Integrated Morphology, Interfacial, and Device Engineering towards High-Performance Perovskite Solar Cells

Po-Wei Liang

A dissertation

submitted in partial fulfillment of the

requirements for the degree of

Doctor of Philosophy

University of Washington

2017

Reading Committee:

Alex K.-Y. Jen, Chair

Fumio S. Ohuchi

Scott T. Dunham

Program Authorized to Offer Degree:

Material Science and Engineering

University of Washington

Abstract

Integrated Morphology, Interfacial, and Device Engineering towards High-Performance Perovskite Solar Cells

Po-Wei Liang

Chair of the Supervisory Committee:
Professor Emeritus Alex K.-Y. Jen
Material Science and Engineering

As a promising renewable energy technology, perovskite solar cells (PVSCs) have made a tremendous progress and received significant attention in recent years, due to the low-cost solution process fabrication, superior charge carrier transporting ability, and decent device performance. In this dissertation, the device performance of PVSCs is enhanced through integrated approaches, such like perovskite thin-film morphology engineering, interface modification of the contact between perovskite and fullerene derivatives layers, and new device architectures. Chapter 1 and 2 briefly overview the current status and the operation mechanism of PVSCs. Chapter 3 demonstrates the importance of the perovskite morphology to the PVSCs performance and the approach of fabricating homogeneous perovskite film. By incorporating Cl^- anions, the

morphology for both pure I and mixed I-Br perovskite become continuous, resulting in an improved device performance. In chapter 4, another methodology to manipulate the perovskite morphology and crystallinity is proposed. An additive, DIO (1, 8-Diiodooctane), was carefully chosen to manipulate the perovskite morphology due to its capability to chelate Pb^{2+} cations. As a result, the increase of precursor solubility and the change of the perovskite crystal growth path generate high-quality perovskite film and decent device performance. Chapter 5 presents an interface charge redistribution between the perovskite active layer and fullerene derivatives, like C_{60}, PCBM, and ICBA. This interesting finding gives us a deeper understating when we try to choose a suitable charge transporting material for high-performance PVSCs. In chapter 6, a device fabrication process is employed to enhance the charge collection efficiency for fullerene layer and passivate the defect states at low bandgap perovskite surface and boundary.

TABLE OF CONTENTS

LIST OF FIGURES

LIST OF TABLES

ACKNOWLEDGEMENTS

I would like to express my sincere gratitude to my Ph.D. dissertation advisor Dr. Alex K.-Y. Jen. I could not finish the dissertation without his dedication. In the past five years, I learned a lot from Dr. Jen, like the knowledge of organic optoelectronic physics and the attitude toward academic research. In addition, I would like to thank my graduate committee members, Dr. Fumio S. Ohuchi, Dr. Scott T. Dunham, and Dr. Cody W. Schlenker for their insightful and constructive comments on my dissertation.

I owe sincere and earnest thankfulness to the Jen group members, Dr. Hin-Lap Yip, Dr. Kevin O'Malley, Dr. Jinyu Zou, Dr. Kung-Shih Chen, Dr. Nam Chul Cho, Dr. Nathan Cernetic, Dr. Chu-Chen Chueh, Dr. Chang-Zhi Li, Dr. Hong Ma, Dr. Jingdong Luo, Dr. Sei-Hum Jang, Dr. Zongling Zhu, Dr. Zhogan Li, Dr. Nara Cho, Dr. Jong Hyun Kim, Dr. Fan Zuo, Dr. Jeremy, Dr. Yunxiang Xu, Dr. Xuikai Xin, Dr. Zhibin Yang, Dr. Lijian Zuo, Dr. Sae Byeol Jo, Dr. Xiaobao Xu, Spencer Williams, Ting Zhao, Adharsh Rajagopal, Dion Hubble, Francis (Ray) Lin, Ian Murphy, Jiaxu Qin, Christine Chang. I would like to thank them for their numerous discussions and great support.

Many thanks to the first generation perovskite team members: Dr. Hin-Lap Yip, Dr. Chu-Chen Chueh, Dr. Fan Zuo, Dr. Xuikai Xin, Chien-Yi(Claire) Liao, Spencer Williams. Thank you all from deep in my heart. It’s been a privilege working with you to build the first perovskite solar cells in our lab.

I would also like to express my gratitude to my previous supervisor Dr. Tzung-Fang Guo. Without his training and help, I would never have a chance to achieve my dream.

Last, I would like to give my deepest appreciation to my beloved parents, sister, wife, and daughter. Special thanks go to my wife Yu-Ju Su who has always been there with me during the Ph.D. study.

Chapter 1. INTRODUCTION

1.1 SOLAR CELLS

Global climate change and the scarcity of the fossil fuel resource mean that the renewable alternatives are urgently needed. Among the clean low-carbon fuel sources, solar power has received tremendous attention because of its unlimited supply and universal availability. The amount of power that sunlight striking earth's surface in just one hour delivers enough energy to power world economy for an entire year.[1] Hence, there is a significant increase in research efforts in finding, developing, and processing new approaches for the efficient conversion of solar energy.

Several Technologies, such as solar thermal, solar fuels, solar cells, etc, are developed to utilize the solar power. The technology of solar cells gained prominence with multiple advantages. First, the operation generates low environmental impacts, like noise, pollution, or radioactive wastes. Second, little maintenance requirement during the operation period. This could effectively reduce the cost of electricity generation. Third, the solar cell modules give the possibility of delivering different size electricity production. For instance, the solar panels can not only be installed on the rooftop for individual users but also could be utilized in the megawatt photovoltaic power plants.

1.1.1 *Inorganic Solar Cells vs Organic Solar Cells*

Various kinds of semiconductor materials have been developed for photovoltaic applications. In general, solar cells could be divided into two categories, which are inorganic and organic photovoltaics. One of the most well-known inorganic photovoltaics is the crystalline silicon (c-Si) solar cells, which dominated over 85% photovoltaic market and generated over tens of TW electrical power. However, the production rate of the solar grade silicon is relatively low, leading

to the power generation cost from solar energy still higher than the traditional power plants. Another famous inorganic photovoltaic is cadmium telluride (CdTe), which is the second largest share in the PV market. CdTe solar cells have the lowest production costs among all the thin-film photovoltaics, which is compatible with Si-based photovoltaics. Besides the cost advantage, the small carbon footprint, low water use and short energy payback time make it attractive compared to the other solar technologies. However, the toxicity of Cadmium and the rarity of Telluride has seriously limited the industrial scalability of CdTe technology.

Another class of material is the organic semiconductors. Organic semiconductors are usually conjugate molecules, which are composed of a series of single and double carbon-carbon bonds. Each carbon on the chain has three covalent bonding and one electron in pz orbital, forming π bonds when these pz orbitals overlap. Hence, the electrons could delocalize along the conjugated backbone, allowing the organic molecules to have high intra-molecule electric conductivity. However, since the weak inter-molecular interaction between two adjacent molecules and lack of long-range order structure, the inter-molecular transporting is much slower and thus limited its mobility. As a result, the free charge carrier mobility in organic semiconductors ($\sim 10^{-3}$ $cm^2V^{-1}s^{-1}$) is several orders lower than inorganic semiconductors ($\sim 10^{3}$ $cm^2V^{-1}s^{-1}$). Nevertheless, the high absorption coefficient properties of organic materials allow the organic photovoltaic could fully utilize the photon in a relatively thin active layer thickness. Therefore, organic semiconductors are usually utilized in the flexible and light-weight electronics, rather than high-speed applications.

Besides the difference in mobility, organic semiconductors usually have relatively lower dielectric constants (around 3-4) than the inorganic semiconductors. As a result, the tightly bonded photo-excited electron-hole pairs, namely Frenkel excitons, inside organic semiconductors have large binding energy (hundreds of meV) compared to the loosely bonded exciton, namely Wannier

exciton (~10 meV), inside inorganic active layers. Thus, these fundamental differences between inorganic and organic semiconductor materials influence the design rules for the inorganic and organic photovoltaics.

1.1.2 *Organic-Inorganic Hybrid Perovskite Solar Cells*

Recently, a new class of solar cell based on mix organic-inorganic halide perovskite have emerged vigorously. Though the first efficient solid-state perovskite solar cells (PVSCs) were represented in mid-2012, the energy conversion efficiencies of PVSCs reached 16.2% at the end of 2013.[2] To date, the confirmed record high efficiency of PVSCs have achieved 22.1%, which is comparable with other conventional thin-film photovoltaics like CIGS and CdTe.[3]

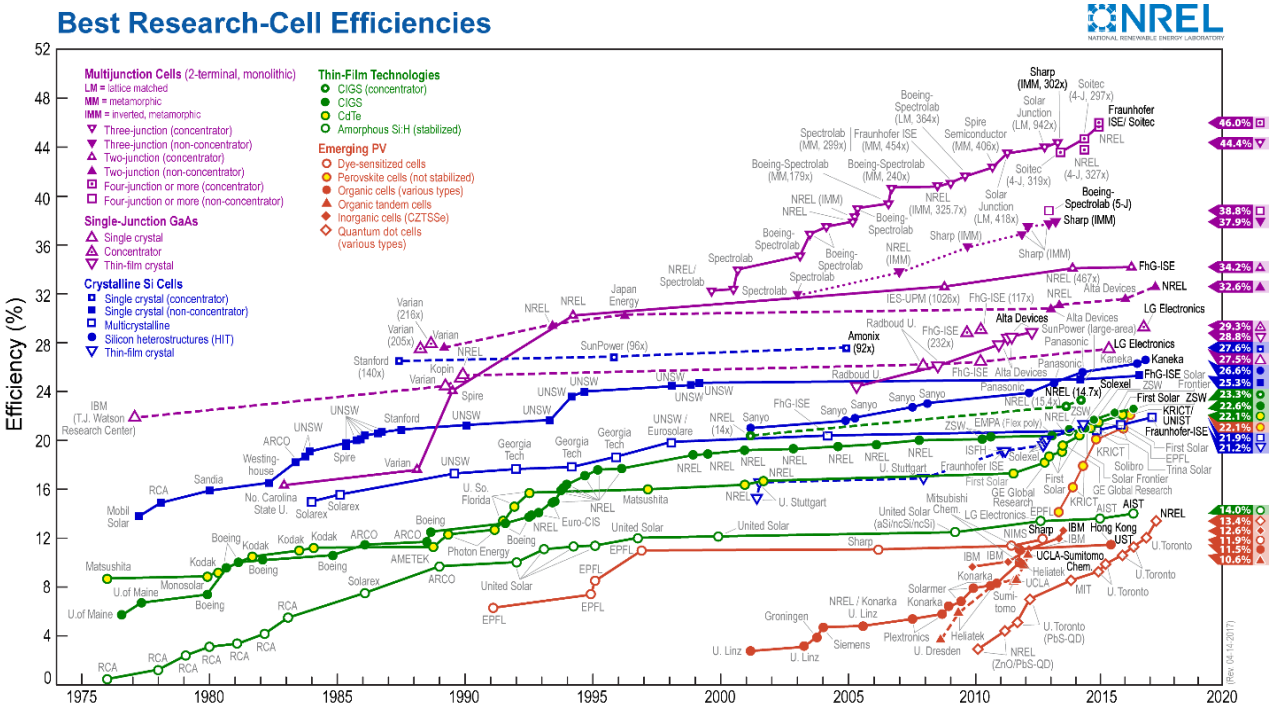

Figure 1.1. Solar cells efficiency table for different kind of materials. The figure was updated at 7/28/2017.[3]

In **Figure 1.1,** the record efficiency of different kinds of photovoltaics is clearly represented in the schematic. It's obvious to see the trend of PVSCs efficiency increased dramatically in recent years. In addition, a wide range of different fabrication methods and device concepts is represented among the highest performance PVSCs, which implies that PVSCs have huge potential to surpass the current state.

Miyasaka et. al. first reported photovoltaic results for perovskite. Through utilization of the nonporous TiO_2 layer in dye-sensitized solar cells (DSSCs) structure, they reported $MAPbBr_3$ PVSCs with an efficiency of 2.2% and $MAPbI_3$ PVSCs with an efficiency of 3.8% in 2009.[4] However, the liquid electrolyte utilized in the photovoltaics would cause the perovskite absorbers degradation and, hence, limit the device lifetime. To enhance the stability of the PVSCs, they replaced the liquid ionic electrolyte with an organic electrolyte containing lithium halide and the corresponding halogen as a hole transporting material (HTM), but this attempt was not particularly successful at that time. Two years later, Park et. al. improved the efficiency to 6.5% based on similar device architectures by applying TiO_2 surface treatment and optimizing perovskite processing.[5]

To enhance the PVSCs device stability, researchers started to find the replacement for the problematic liquid electrolyte. Park et. al. and Gratzel et. al. introduced a spiro-OMeTAD (2,2',7,7'-tetrakis(N,N-di-p-methoxyphenylamine)-9,9'-spirobifluorene) as an effective solid-state HTM for PVSCs. The HTM could transport hole carriers in solid-state and be processed by organic solvents, which has limited effects on perovskite absorbers. This innovation not only improved the stability but also boosted the PVSCs efficiency to 9.7%.[6,7]

Later, several important discoveries were reported along with PVSCs. First, Snaith et al. formed a continuous thin perovskite layer, instead of nanoparticles, on top of the mesoporous TiO_2

scaffold, resulting in a better absorption.[7] Second, a PVSCs with an efficiency of 10.9% was represented even when they employed an insulator Al_2O_3 as an electron transporting material (ETM).[7] This result demonstrated that perovskites have capacity more just than sensitizers, as it could transport both hole and electron as well. Third, scientists discovered that the diffusion lengths of mix-halide perovskites, $MAPbI_xCl_{3-x}$, are over 1 um, which is better than charge carrier transport properties of pure iodide perovskite materials. Since then, the PVSCs filed was split wide open and became prosperous.[8,9]

1.2 Basic Properties of Perovskite Materials

1.2.1 *Crystal Structure*

The term perovskite refers to the crystal structure of calcium titanate ($CaTiO_3$), which was discovered by the German mineralogist Gustav Rose in 1839 and named after the Russian mineralogist Lev Perovski.[10] Generally, the perovskite crystal could be described in a chemical formula ABX_3, where A and B are cations; X is anions. In the field of perovskite photovoltaics, the A sites are organic cations, such as $CH_3NH_3^+$ (MA) or $NH_2CH_3NH_2^+$ (FA); B sites are divalent metal cations, such as Pb^{2+} or Sn^{2+}; and X sites are monovalent halide anions, like I^-, Br^-, or Cl^-. **Figure 1.2a** shows the crystal structure of a perovskite $MAPbI_3$ unit cell, where eight MA^+ located at the vertices of a cubic cage; Pb^{2+} located at the center of the cube; and I^- located at the face center of the cubic cage.

To estimate the crystallographic stability and probable structure, tolerance factor *t* and octahedral factor μ were introduced.[10] The definition of *t* can be expressed as:

$$t = \left(\frac{R_A + R_X}{\sqrt{2}\ (R_B + R_X)}\right) \quad (1.1)$$

where R_A, R_B, and R_X are the ionic radii of the corresponding ions. For the μ, the equation can be written as:

$$\mu = \frac{R_B}{R_X} \tag{1.2}$$

If *t* locates in the range 0.89-1.0, a more symmetric cubic structure would be formed. Tetragonal or orthorhombic structures are preferred if a lower t value derived. The calculated *t* and μ of the halide perovskites with different ammoniums cations, like MA and formamidinium (FA; $HC(NH_2)_2^+$), and metal cations, like Pb, are listed in the **Figure 1.2b**.

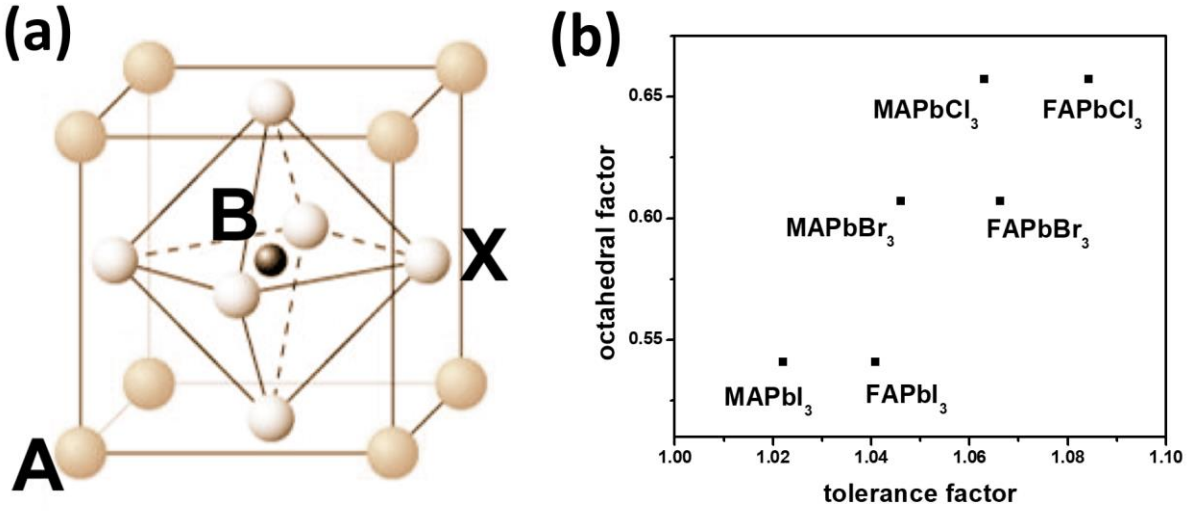

Figure 1.2. Organic-inorganic hybrid halide perovskite (a) crystal structure. The estimated (b) tolerance/octahedral factor for several common perovskite materials.

1.2.2 *Electronic Structure*

The first studies of the electronic band structure of organometal 2D or 3D perovskites have been reported by Papavassiliou team.[11] For $MAPbI_3$ perovskite, Chang et al. showed the valence band (VB) maximum comprise the Pb 6p-I5p σ antibonding orbital, while the conduction band (CB) minima consists of Pb 6p–I 5s σ antibonding and Pb 6p–I 5p π antibonding based on first principle

density functional theory (DFT) calculation, as shown in **Figure 1.3**.[12,13] Then, Mosconi et al. represented the band structure for $MAPbI_3$ (cubic phase) and the mixed halide $MAPbI_2X$ (tetragonal phase) (X = Cl, Br and I) by considering its surrounding MA cations, which was ignored in the early studies.[14] However, the band energies are still mainly determined by the $[PbI_4]^{6-}$, instead of the organic counterions. Another factor like spin-orbital coupling (SOC) effect has also been investigated. Even et al. found that the SOC effect could seriously reduce the CB of the perovskites.[14]

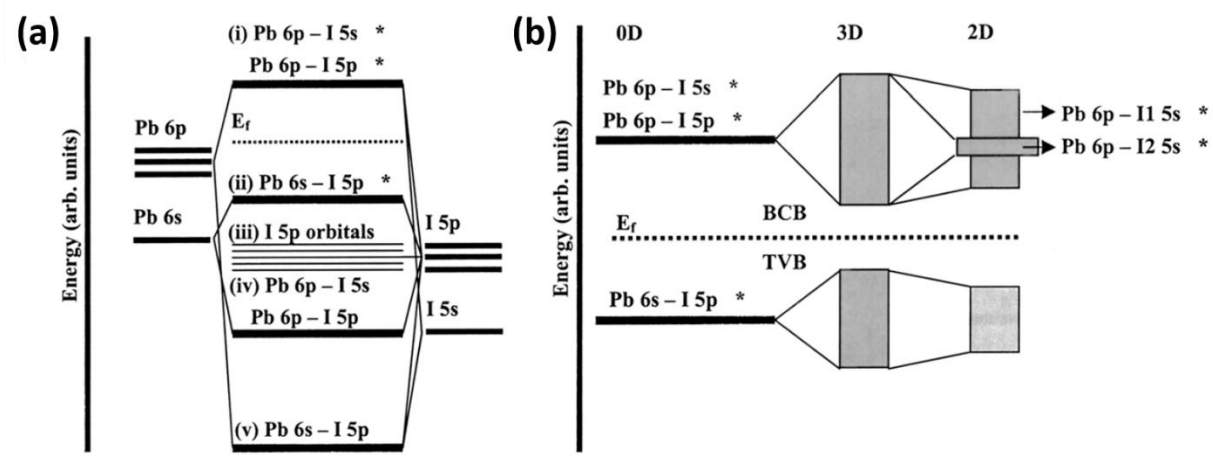

Figure 1.3. Bonding diagram of (a) $[PbI_6]^{4-}$ cluster (0-D), (b) $MAPbI_3$ (3D) and $(C_4H_9NH_3)_2PbI_4$ (2-D) at the valence band maximum and at the conduction band minimum.[15]

Recently, there are some arguments about the nature of the perovskite bandgap. Traditionally, $MAPbI_3$ perovskite has been recognized as a direct bandgap semiconductor according to both theoretical calculations and experimental data.[6,15] However, the superior long charge carrier lifetime of perovskite is more similar to the characteristics of indirect bandgap semiconductors.[16] Many explanations have been proposed, including long-lived trapping of charge, large polarons, and triplet exciton formation.[17–19] Lately, Brivio et al. theoretically predicted that a slightly indirect bandgap formed in the perovskite by using quasiparticle self-consistent GW theory.[20,21]

Ehrler et al. showed that $MAPbI_3$ perovskite has a weakly indirect bandgap, arising from the distortion of the lead iodide framework, 60 meV below the direct bandgap transition.[22] The nature of the bandgap become more direct when slowly increasing the hydrostatic pressure from ambient to 325 MPa. A similar concept of an indirect-direct characteristic of $MAPbI_3$ perovskite was also proposed by Savenije's group.[22]

1.2.3 *Absorption and Bandgap Tuning*

The absorption coefficient of $MAPbI_3$ is around 1.5×10^4 cm^{-1} at 550 nm, which is comparable to the other conventional photovoltaics materials like GaAs, CdTe, and CIGS.[5] The absorption coefficient values for each type of solar cells materials are shown in **Figure 1.4**. This value indicates that the penetration depth for the light with 550 nm wavelength is only 660 nm and, hence, perovskite materials are perfect for thin-film photovoltaic applications.

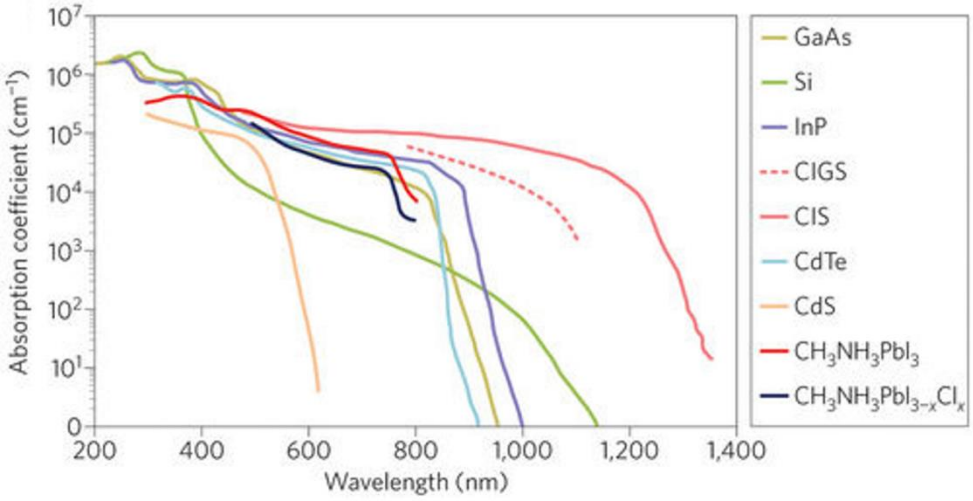

Figure 1.4. The absorption coefficient of $MAPbI_3$ and $MAPbI_{3-x}Cl_x$ compared to other types solar cell materials. [23]

Perovskite materials possess flexible bandgaps that can continuously be tuned within the range of 0.9-1.6 eV via the element-mixing strategy. For the most well-known perovskite $MAPbI_3$, the bandgap was evaluated to be 1.49-1.55 eV from the onset of UV-vis absorption spectrums.[6] Though replacing MA with other organic cations, like FA, the bandgap could be reduced by about 0.07 eV since the M-X-M bond length and the angle was modified.[22] This replacement could extend the absorption wavelength by about 40 nm. Another approach is through the modification of M-X bond. By partially replace Pb^{2+} with Sn^{2+} in perovskite composition, the bandgap could be tuned in a range of 1.55-1.17 eV.[22] However, since the band edges are related to the B-site metal orbitals, the VB maximum and the CB minimum position would be affected. In addition to cation replacement in the perovskite lattice, halide substitution (X= I, Br, or Cl) is another effective way to tune E_g.[14,24–29] Several recent studies have shown that perovskite solar cells with wide bandgap can be achieved by manipulating the ratio of iodide (I^-) and bromide (Br^-).[26–30] The bandgap of lead halide perovskites can be enlarged from 1.6 eV to 2.3 eV, enabling the narrowed absorption region required for employment in tandem architectures with the state-of-the-art inorganic solar cells for higher device efficiencies. **Figure 1.5** shows the electronic band structure for the perovskite with different compositions ABX_3 (A = MA or FA, B = Pb, Sn, or Pb_xSn_{1-x}, and X= Cl, Br, I, or I_xBr_{1-x}).[12]

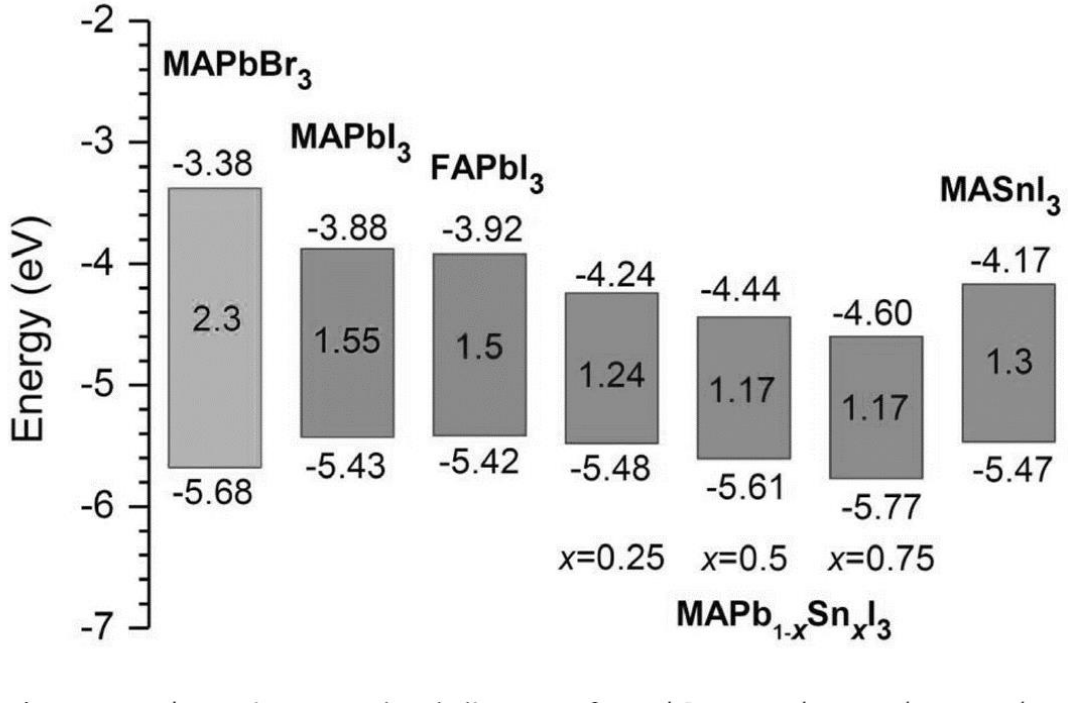

Figure 1.5. The energy level diagram of perovskite with different compositions.

1.2.4 *Dielectric Constant and Exciton Binding Energy*

The relationship of the real part of dielectric permittivity (dielectric constant) ε′ of the organometal halide perovskites and phase (temperature) was investigated. The perovskites tetragonal phase (180K < T < 300K) have higher ε′ than the orthorhombic phase (T <180K).[31–33] Besides the temperature, ε′ is also related to the halide anions in perovskite compositions. At room temperature, ε′ is around 40, 50, and 60 for $MAPbCl_3$, $MAPbBr_3$, and $MAPbI_3$ at 100 kHz, respectively. At the lower temperature where the perovskite crystal become orthorhombic phase, ε′ is around 17, 26, and 36 for $MAPbCl_3$, $MAPbBr_3$, and $MAPbI_3$, respectively. Since the value of ε′ at this state is independent of temperature, it implies that the ε′ stems from the electronic or ionic polarization. Worth to note, a giant ε′ of 10^7 were observed from perovskite upon illumination. A strong ε′ incensement at low-frequency spectrum, as shown in **Figure 1.6**.[33] This phenomenon might have attributed to the MA cations molecular orientation.

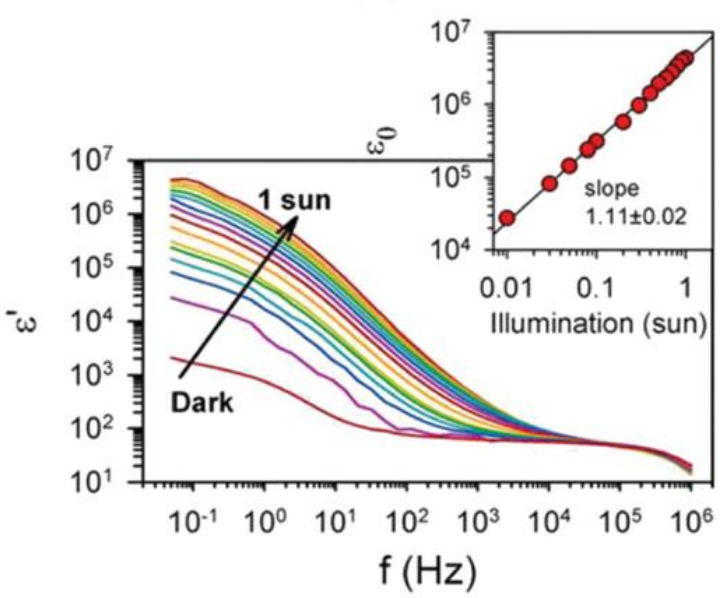

Figure 1.6. The dielectric constant as a function of frequency for different incident light intensities from dark to 1 sun (100 mW/cm^2) for $MAPbI_xCl_{3-x}$. Inset: the relationship of dielectric constant and illumination intensity at f= 50mHz.[33]

In respect to the binding energy of perovskites, different values have been determined experimentally for tetragonal $MAPbI_3$ at room temperature. Collavini et al. reported that the uncertainty in binding energy measurement in perovskite materials mainly stem from the dielectric constant, which is used to derive binding energy. Even though the optical dielectric response is well established, the low-frequency response related to electronic and ionic polarization is not fully understood yet.[35-38] Thus, it's challenging to determine the screening of the exciton. Recently, the binding energy has been determined directly from the high-field magneto-absorption measurement. A binding energy of 12 meV was reported in the tetragonal phase under a high magnetic field, and a binding energy of <5 meV was estimated at zero magnetic fields at room temperature.[34,35] With such low binding energy value, the main electron carriers in $MAPbI_3$ PVSCs were expected as free charges.

1.2.5 *Charge Transport Properties*

The organometal perovskite charge transport properties are summarized in **Table 1.1**. From the table, it's clear to see the measured mobilities in perovskite materials are modest compared with other high-quality semiconductors, like GaAs or Si. The polycrystalline perovskite films have mobilities of 1-30 $cm^2V^{-1}s^{-1}$, while perovskite single crystals have mobility exceeding 100 $cm^2V^{-1}s^{-1}$.[8,36–40] Generally speaking, most high-performance PVSCs are made of polycrystalline perovskite thin film, leading to the question why PVSCs have such efficient charge collection while it has modest mobilities. It seems to stem from long carrier lifetimes (0.01-1 μs, under 1 sun condition) for a direct-bandgap semiconductor.[8,37,38,41–43] The number is compatible with those of low-doped, surface-passive GaAs. Hence, despite the modest mobilities, the long carrier lifetimes of perovskite still generate long diffusion length around 1μm in the polycrystalline film, which is several times longer than the absorption depth. As a result, the photoexcited charge carriers can be collected efficiently and the high conversion efficiency can be achieved.

Table 1.1. Summary of transport characteristics of organometal perovskite materials and other comparison semiconductors.

	Diffusion length *(μm)*	**Carrier lifetime *(μs)***	**Mobility ($cm^2V^{-1}s^{-1}$)**	**Trap density (cm^{-3})**	**Refs**
$MAPbI_3$ polycrystalline film	0.1-1	0.01-1	1-10	10^{15}-10^{16}	[8,9,39,44–46]
$MAPbI_3$ single crystal	2-8	0.5-1	24-105	$(1\text{-}3)\times10^{10}$	[36,37,43]
$MAPbBr_3$ polycrystalline film	0.3-1	0.05-0.16	30	---	[38,42,43,47,48]
$MAPbBr_3$ single crystal	3-17	0.3-1	24-115	$(0.6\text{-}3)\times10^{10}$	[36,43]
Si	e^- 1,000 h^+ 600	~1,000	1,450 500	10^8-10^{15}	[49]
GaAs	e^- 7 h^+ 1.6	~0.01-1	8,000 400		[49,50]

1.3 FUNDAMENTALS OF PEROVSKITES PHOTOVOLTAICS

1.3.1 *Basic Working Principle*

Light absorption, charge separation, charge transport, and charge collection are general solar cell working mechanism. However, there are two distinctive features for the PVSCs. First, organometal halide perovskite materials have a very low binding energy, allowing the photo generated electron-hole pairs can be dissociated spontaneously in a picoseconds time scale without a heterojunction junction structures.[35,48,51–54] Second, organometal halide perovskites show ambipolar charge transporting properties.[55] This unique property allows organometal perovskites act as not only light harvesters but also electron/hole charge transporters. Hence, perovskite active-layers have huge flexibility to apply in either a p-i-n junction or a p-n junction solar cell. People have estimated the perovskite charge carriers transporting properties through different techniques, like X-ray diffraction patterns and electron beam-induced current (EBIC) image.[8,56] In the former method, electron and hole diffusion lengths were ~130 nm and ~100 nm respectively for $MAPbI_3$ samples prepared by $MAI+PbI_2$ mixture, while longer diffusion lengths of ~1069 nm and ~1212 nm respectively for $MAPbI_3$ samples prepared by $3MAI+PbCl_2$ mixture. The difference in diffusion length of the perovskites with different preparation methods may due to the quality of perovskite layer, like crystallinity or grain size. From the EBIC method, the charge diffusion lengths were about 1 μm for the samples prepared by both precursors, but the hole diffusion length was longer than the value of electron in the case of $MAPBI_3$ without chloride elements. Both these techniques show that the organometal halide perovskites possess decent charge transporting properties and, hence, act as superior materials for photovoltaics applications.

The following schematic, as shown in **Figure 1.7**, depicts the loss mechanisms for perovskite active layers.[57] The efficient pathways and suppressed pathways for power loss in perovskites are

shown in the black and gray line, respectively. For the excitons, the loss mechanism is mainly Geminate recombination, which is not an efficient pathway in the PVSCs. For the free charge carriers, trap-assisted recombination and non-Geminate recombination are extremely low. With a strong intensity light, the dominant recombination mechanism in $MAPbI_3$ is Auger recombination, which the released energy from the recombination of electrons and holes would be absorbed by another charge carriers. Interestingly, at higher intensity photo illumination, amplified spontaneous emission (ASE) would compete for the Auger process in perovskite.[58] As a result, Auger recombination and ASE would be strongly suppressed when PVSCs operated under sunlight condition. This figure well explains why organometal halide perovskites become excellent photovoltaic materials.

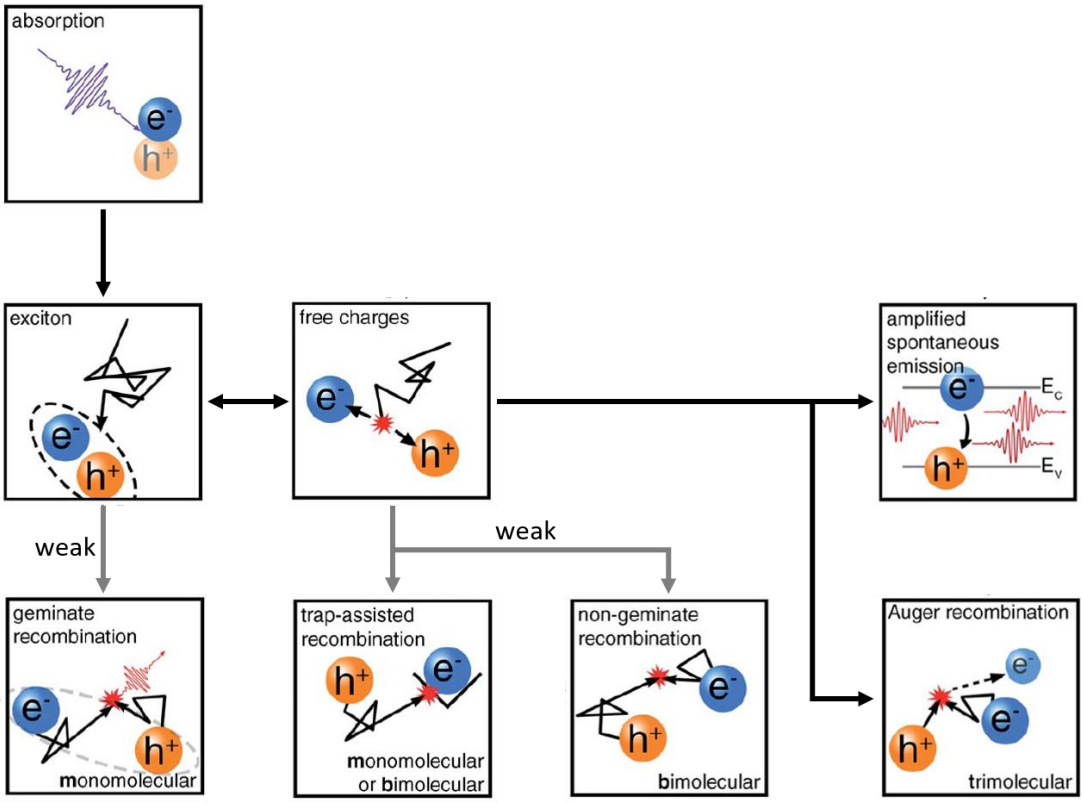

Figure 1.7. A schematic of photovoltaics process and loss mechanism in perovskite solar cells (PVSCs).[57]

1.3.2 *Device Architectures*

Two typical architectures, a mesoporous and planar device structures, are often utilized to fabricate perovskite photovoltaics. These device structures are shown in **Figure 1.8**. For the PVSCs with mesoporous structures, the experimental results showed the transporting rate is similar to those of planar devices, but the recombination rate of mesoporous devices is higher.[59] This result indicates the dominant charge transport pathway is the though the perovskite materials, even in the PVSCs with the mesoporous TiO_2 scaffold. However, the mesoporous TiO_2 still plays an important role since a different performance was observed from the comparison between rutile and anatase mesoporous TiO_2 scaffolds.[58] In addition, different TiO_2 mesoporous nanostructures, like 3D-TiO_2 nanoparticles/ITO nanowire composites and TiO_2 nanoparticle/graphene composites, were used to improve the PVSCs performance.[60–62] Surface engineering techniques, like ultra-thin MgO nanolayer or fullerene self-assembling monolayer (SAM), are also identified as an efficient strategy to control the charge transport and recombination at the TiO_2/Perovskite interface.[60,63]

Planar PVSCs were proposed because scientists tried to get rid of the high temperature (over 400°C) mesoporous TiO_2 scaffold fabrication process. The low-temperature process allows the devices to have more flexibility. For instance, ITO coated poly(ethylene terephthalate) (PET) substrates, the most common substrates for flexible photovoltaics, can only sustain till 250°C. The first planar PVSCs were demonstrated with the inverted structure (p-i-n) of PEDOT:PSS/perovskite/PCBM.[64] The processes of these materials are under 150°C, which is suitable for the flexible PVSCs fabrication. There is another planar device structure associated with different type of stacking order, which is n-i-p structure. This structure also named conventional structure, meaning electron transport materials (ETM)/perovskite/hole transporting

materials (HTM). By utilizing the low-temperature process ZnO nanoparticle, Kelly et al. reported a flexible PVSCs with an efficiency of 10.2% based on conventional structure.[64]

Besides the two typical perovskite device structures depicted in **Figure 1.8**, an HTM free structure is also possible since perovskite possesses decent hole transporting properties. The first HTM-free PVSCs were constructed with FTO/2D sheet TiO_2/$MAPbI_3$/Au configuration and showed an efficiency of 5.5%.[65] Through modulation of the depletion layer at the junction of TiO_2 and perovskite, the performance could be further improved to 10.85%.[66] An inverted HTM-free device structure of ITO/Perovskite/PCBM/Ag with 10% conversion efficiency was also demonstrated.[30]

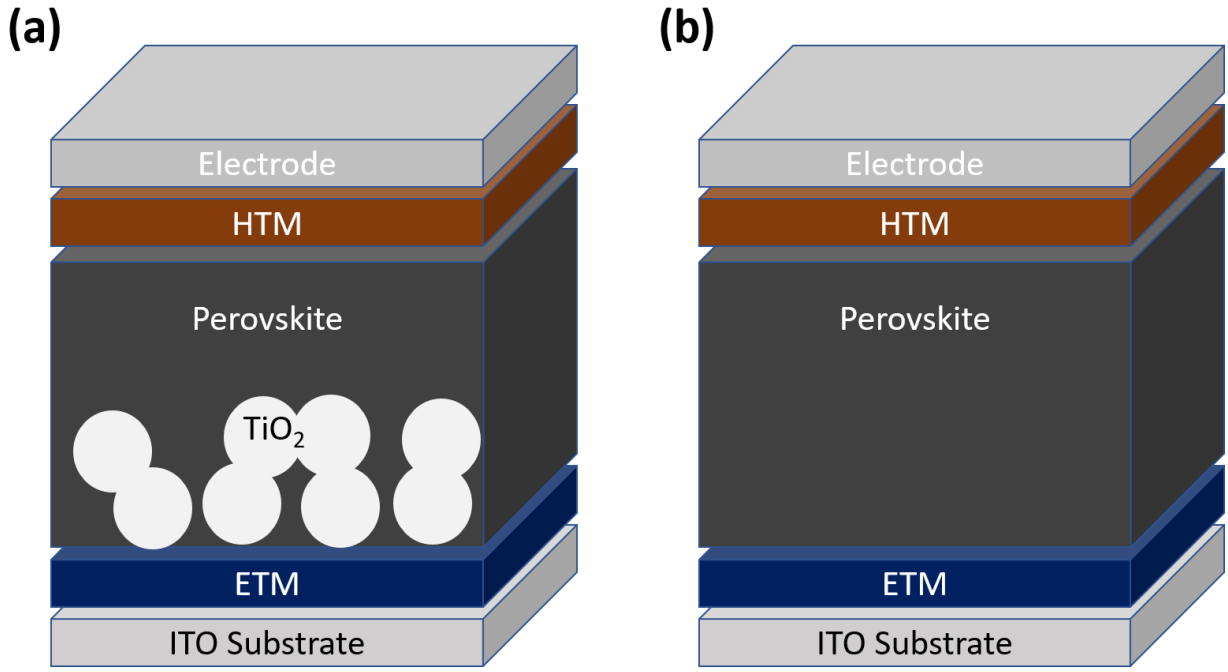

Figure 1.8. Perovskite solar cells (PVSCs) with (a) mesoporous TiO_2 layer and (b) planar structure.

1.3.3 *Commercialization Challenges*

Despite organometal halide perovskites have series of superior characteristics to become great photovoltaic active materials, there are many non-trivial challenges for commercialization. A

critical requirement for commercialization is an extraordinary advantage over the existing technologies. For PVSCs, the advantages might be high conversion efficiency, low fabrication cost, or unique properties such as flexible and semi-transparent devices. However, the presence of Pb in the perovskite components and lack of robustness may create extra barriers to utilizing the materials in consumer products.

Fabrication and Module Cost

The lowest fabrication cost of thin-film photovoltaics is CdTe. Only couple of hours is needed from a glass substrate to a CdTe photovoltaic modules. At 2013, the power per watt of US$ 0.54 W^{-1} and the average module conversion efficiency of 13.4% was reported by considering the fabrication and materials cost, including the FTO-coated glass sheets, junction boxes, tabbing, encapsulation, sealants, and tempered glass back-sheets.[65] It is expected to achieve the operation cost to US$ 0.38 – 0.41 W^{-1} and the average module conversion efficiency of 17.2% by the end of 2017.[65] However, this is still slightly higher than the operation cost of mainstream Si-based photovoltaic modules.

On the other hand, PVSCs have a low production cost due to the facile solution fabrication process and abundant materials supply, but this is unlikely to greatly lower the cost per unit area because of the fragile environmentally stability of PVSCs. Since perovskite materials are not robust enough to against the moisture environment, they require better quality encapsulations. In other words, it's an expensive solution to overcome this issue. Although the PVSCs might use the tandem structure to boost its efficiency to lower down the operation cost in order to compete with CdTe modules, there are still many challenges and issues need to be solved to realize a highly efficient tandem PVSCs.

Hazardous metal

One of the indispensable elements in high-performance perovskite materials is lead (Pb), which is a hazardous heavy metal to the environment. To become a consumer product, this technology should meet the requirement of government regulation. According to the European Restriction on Hazardous Substances (RoHS), the content of Pb should be less than 1000 ppm. For the PVSCs with planar structures, the Pb contents certainly are much higher than the standard.[65] Even if we apply it to the mesoporous TiO_2 structure to dilute Pb content, there is still around 4000-5000 ppm in mesoporous PVSCs.[65] The calculation is based on 60% porosity mesoporous TiO_2 scaffold and the pores are filled with spiro-OMeTAD. Besides that, the Pb compounds usually have a relatively good solubility in water, which may create a serious problem if the disposal doesn't be well taken.

Stability

A key challenge for the commercialization is the PVSCs stability. With the tremendous research efforts spent on improving the stability of the device though perovskite composition tuning, new materials development, interface/device architecture engineering, the state of art PVSCs possess over thousands of hours lifetime now. However, it is still far from the lifetime of Si photovoltaics, which is over 20 years. The efficiency degradation of PVSCs might be related to many plausible reasons, such as moisture, oxygen, temperature, UV light, ion migration, and interfacial interaction.[65] Thus, setting a stability standard analysis protocols and knowledge to investigate the degradation of PVSCs become an important issue.

Chapter 2. SAMPLES PREPARATION AND CHARACTERIZATION

2.1 SAMPLES PREPARATION

2.1.1 *Perovskite Precursor*

Methylammonium Iodide (MAI) Synthesis

Methylammonium iodide (MAI) was synthesized by reacting 24 mL of 0.20 mol methylamine (33 wt% in absolute ethanol, Aldrich), 10 mL of 0.04 mol hydroiodic acid (HI) (57 wt% in water with 1.5% hypophosphorous acid, Alfa Aesar), and 100 mL ethanol in a 250 mL round bottom flask under nitrogen at 0 °C for 2 hour with stirring. After the reaction, the white precipitate of MAI was recovered by rotary evaporation at 40 °C and then dissolved in ethanol followed by sedimentation in diethyl ether by stirring the solution for 30 min. This step was repeated three times and the MAI powder was finally collected and dried at 50 °C in a vacuum oven for 24 hours.

Perovskite Precursor Preparation

Since there are many methods to deposit the perovskite thin film, this section only shows the $MAPbI_3$ perovskite precursor for one-step solution deposition method. Please refer to the experimental sections for more information about each project. To prepare the perovskite precursor solution, MAI and PbI_2 powder were mixed in anhydrous dimethylformamide (DMF, Aldrich) with a molar ratio of 1:1. The precursor solution concentration is about 1M. The solutions were stirred overnight at 80 °C and filtered with 0.45 μm PVDF filters before device fabrication.

2.1.2 *Perovskite Thin Film Deposition Methods*

Solution Process: One-Step vs Two-Step Coatings

Two solution deposition methods were developed for perovskites, which are the one-step and two-step coating methods. One-step method, as shown in **Figure 2.1a,** means that spin-coating a

perovskite precursor, which is made by mixing MAX and PbX_2 (X is halides) at a certain ratio in polar aprotic solvents, such as N, N-dimethylformamide (DMF), gamma-butyrolactone (GBL), or dimethyl sulfoxide (DMSO), etc. Though this method is facile and simple, it's challenging to form a continuous pinhole-free perovskite thin film. Since perovskite morphology is a critical factor for device performance, scientists have developed several methods to improve the process. One of the methods is mixing the precursor with additives, such as MACl, 1, 8-diiodooctane (DIO), NH_4Cl, HI, I_2, H_2O/HBr, phosphonic acid ammonium etc, to manipulate the perovskite crystallization.[67–71] Besides, solvent engineering has been intensely studied. An MAI-PbI_2-DMSO intermediate phase was discovered when perovskite precursor dissolved in a mixed GBL and DMSO at 7:3 volume ratio.[2] After toluene solution wash, the excess DMSO would be removed and the intermediate state will be left. With this method, a certified efficiency of 16.2% was reported. Likewise, a fast perovskite crystallization was reported through utilizing chlorobenzene to quench a spin-coating perovskite precursor.[72] By this method, a device performance of 13.9% was achieved.

Another solution based deposition is two-step sequential deposition method (**Figure 2.1b**) which was developed by Mitzi team. and applied in PVSCs by Burschka team.[73,74] There are two steps for a typical sequential fabrication procedure. The first step is that spin-coating PbI_2 solution under appropriate conditions, including the solution concentration and spin speed. After spinning, a yellowish PbI_2 layer would be formed. The second step is that dipping the substrate into the MAI solution. Usually, the solvent for MAI is isopropanol since it has a low solubility for PbI_2. The cuboid-like crystal structure was observed in the perovskite thin film prepared by a two-step method, whereas needle-like morphology in the perovskite prepared by a one-step method.[73,74] Two-step sequential method offers a unique advantage for PVSCs with the mesoporous TiO_2

scaffold. It can be expected that the mesoporous layer would be better infiltrated through the sequential deposition process since the volume expansion (~75%) occurring during the conversion from PbI_2 to perovskite.[75] Thus, the two-step sequential deposition offers a pathway to high reproducible performance for mesoporous PVSCs.

Vapor Deposition Process

$MAPbI_{3-x}Cl_x$ perovskites formed through dual-source evaporation of $PbCl_2$ and MAI was demonstrated by Snaith's group.[76] **Figure 2.1c** shows that the solid state of $PbCl_2$ and MAI were heated to vapor state and deposited on the compact TiO_2 substrate under a high vacuum. The perovskite thin film formed from vapor deposition shows ultra-homogeneous without any pinhole. The conversion efficiency can reach about 15.4%.[76] However, the high vacuum procedure increases the fabrication cost of mass production. To resolve this problem, Yang et al. developed a method of vapor-assisted solution process (VASP), as shown in **Figure 2.1d**.[75] They formed PbI_2 layers on substrates through spin-coating first, then treated it with MAI vapor. The perovskite film formed from this approach showed excellent coverage and uniform grain size, resulting in a device performance of 12.1%.[75] The advantages of these vapor deposition process are easy to control the perovskite thin film quality and thickness, which could generate reproducible experimental results.

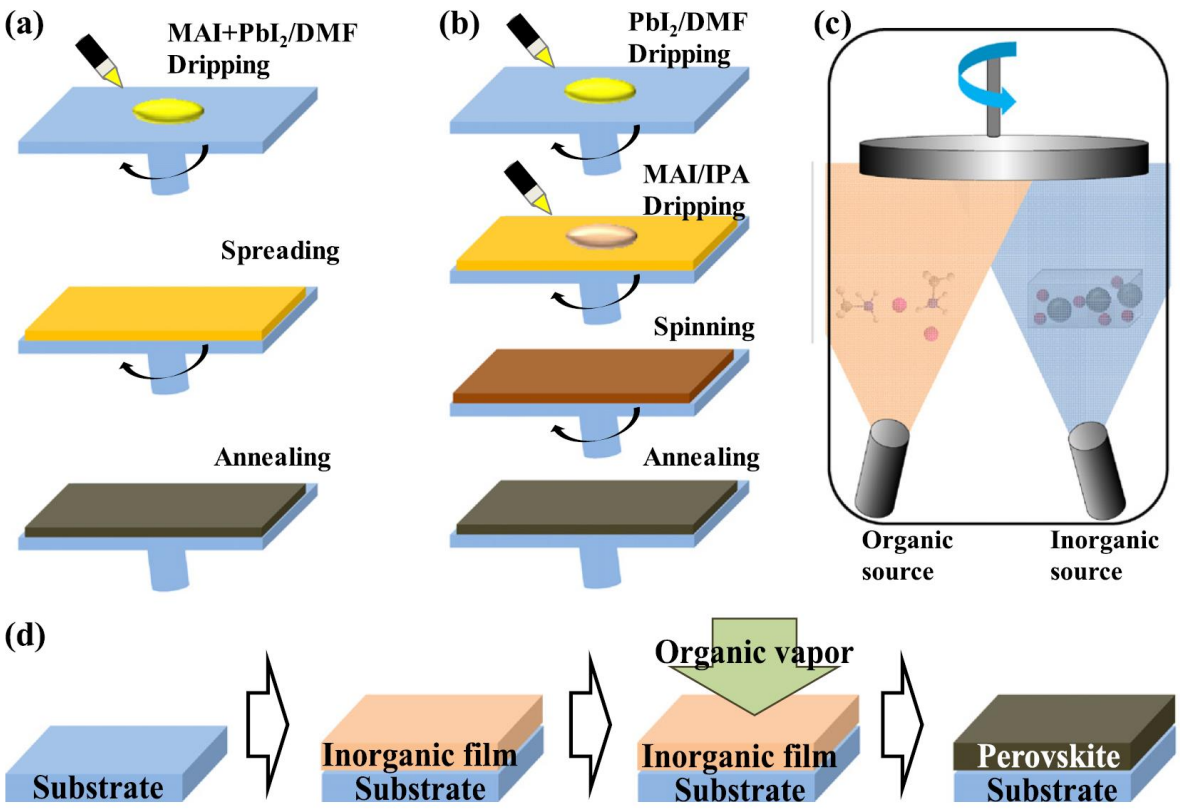

Figure 2.1. Four general methods for depositing perovskite thin film. (a) one-step deposition, (b) two-step sequential deposition, (c) dual-source evaporation deposition, and (d) vapor-assisted solution process.[75]

2.1.3 *Perovskite Solar Cells Fabrication*

Most of the devices present in this dissertation were fabricated in the configuration of indium tin oxide (ITO) or fluorine-doped tin oxide (FTO)/PEDOT:PSS/perovskite/[6,6]-phenyl-C_{61}-butyric acid methyl ester (PCBM)/fullerene surfactant (C_{60}-bis)/Ag. Please see the experimental section in each chapter for more information about each project. ITO (15 ohm/sq) and FTO (8 ohm/sq) glass substrates were cleaned sequentially with detergent and deionized water, acetone, and isopropanol under sonication for 10 min. After drying under N_2 stream, substrates were further cleaned by a plasma treatment for 30 s. PEDOT:PSS (Baytron PVP Al 4083, filtered through a

0.45 μm nylon filter) was first spin-coated onto the substrates at 5k rpm for 30 s and annealed at 150 °C for 10 min in air. To avoid oxygen and moisture, the substrates were transferred into an N_2-filled glovebox, where the thin-film perovskite layers were deposited through solution or vapor deposition approaches which described in the previous section. Afterward, the PCBM (15 mg/mL in chloroform) and C_{60}-bis surfactant (2 mg/mL in isopropyl alcohol) were then sequentially deposited by spin coating at 1k rpm for 60 s and 3k rpm for 60 s, respectively. Silver electrodes with a thickness of 150 nm were finally evaporated under high vacuum ($<2\times10^{-6}$ Torr) through a shadow mask. The device areas are defined as 3.14 mm^2 or 10 mm^2.

2.2 SAMPLES CHARACTERIZATION

2.2.1 *Solar Cells Parameters and Measurement*

To analyzed different type of photovoltaic devices fabricated from different companies and laboratories, a standardized test is needed for a fair comparison. According to the International Electrotechnical Commission (IEC) norm, the standard test conditions are listed as follows: (1) Air mass 1.5 spectrum (AM1.5). (2) Light intensity of 100mW/cm^2 (1kW/m^2 or one-sun illumination). (3) Temperature of 25℃.[75]

Under the standard characterization conditions, the performance of solar cell can be deducted from the current density-voltage (*J-V*) measurement. The fourth quadrant in **Figure 2.2** represents the power generation region since the direction of the current is opposite to the applied voltage bias. The maximum power density (P_{max}) can be calculated from the product of *V* and *J* at the maximum power point (MPP). The short-circuit current density (J_{sc}) means the y-intercepts, where the *J-V* curve crossing the y-axis (*V* = 0 V). On the counterpart, the open-circuit voltage (V_{oc}) is the x-intercepts, where the *J-V* curves meeting the x-axis (*J* = 0 mA/cm^2). In an ideal device, the P_{max} is equivalent to the multiplication of the V_{oc} and the J_{sc}, as shown in the blue rectangle area in

Figure 2.2. In a real device, the P_{max}, as depicted in the green area in **Figure 2.2**, is always lower than the multiplication of the V_{oc} and the J_{sc} because of the various energy losses. To quantify the deviation from the ideality, fill factor (*FF*), the ratio between the green area to the yellow area, is used to describe the discrepancy. The equation could be written as:

$$FF = (V_m \cdot J_m) / (V_{oc} \cdot J_{sc}) \quad (2.1)$$

The value of *FF* could give us a hint how close to its theoretical maximum. For a normal silicon photovoltaic, the average *FF* is around 80%.

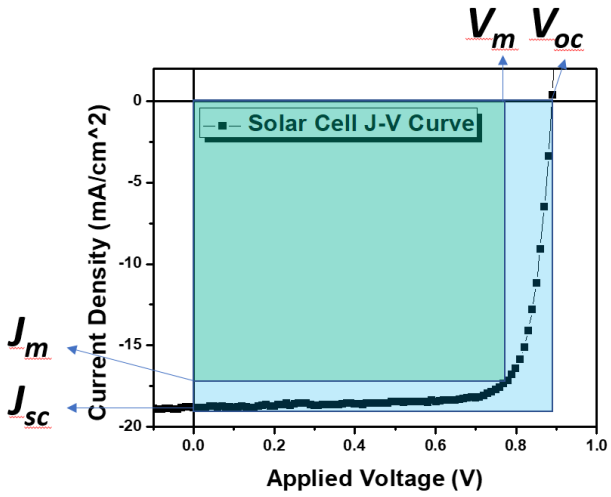

Figure 2.2. Current-voltage (*J*-*V*) curve for a typical solar cell under illumination.

Power conversion efficiency (PCE) is a parameter to evaluating how efficient a solar cell can transfer the incident light power density (P_{in}) to output electrical power (P_{out}). P_{in} represented as the product of the PV device area and the incident light, which is one-sun (100 mW/cm^2) condition. Since the solar cells usually work at the MPP, we could simply take P_{max} as P_{out}. Hence, it can be represented by the equation as:

$$PCE = P_{out}/P_{in} = P_{max}/P_{in} = (V_m \cdot J_m)/P_{in} = (V_{oc} \cdot J_{sc} \cdot FF)/P_{in} \quad (2.2)$$

From the equation, PCE is clearly related to the three parameters V_{oc}, J_{sc}, and *FF*. It indicates that we could improve the device performance through optimized each parameter. For instance, *FF* is greatly affected by the power dissipation across internal resistances. These parasitic resistances can be identified as a parallel shunt resistance (R_{sh}) and series resistance (R_s). For an ideal cell, the R_{sh} is infinite and the current has no route to flow, while the R_s is zero and the voltage has no drop before the load. With the device engineering to maximizing the R_{sh} and minimizing R_s of PV devices, FF and, hence, PCE could be further improved.

Another important parameter of solar cells is quantum efficiency (QE), which is the measure of the electron generated when a cell irradiated by photons at a given wavelength. Through the integration of the cell's QE over the whole solar spectrum, it could evaluate the amount of current produced by an illuminated solar cell. Worth to note, over 100% QE may be possible because of the incident photon energy could be higher than twice the band-gap energy, resulting in two or more excitons creation per incident photon. Two types of QE are often considered for a solar cell. The first one is external quantum efficiency (EQE), which is the ratio of the number of charge carriers collected by the number of photons at a given wavelength from outside of the solar cells. The equation of EQE can be expressed as:

$$EQE(\lambda) = \frac{number\ of\ collected\ electrons/sec}{number\ of\ incident\ photons/sec} \times 100\% = \frac{hc}{q}\frac{J_{sc}(\lambda)}{\lambda \cdot P_{in}(\lambda)} \qquad (2.3)$$

Where λ is the wavelength, *h* is the Planck's constant, *c* is the speed of light, *q* is the elementary charge. Another important QE is the internal quantum efficiency (IQE), which is the ratio of the number of charge carriers collected by a solar cell to the number of photons at a given energy that absorbed by the cell. The equation of IQE could be written as:

$$IQE(\lambda) = \frac{number\ of\ collected\ electrons/sec}{number\ of\ absorbed\ photons/sec} \times 100\% = \frac{EQE(\lambda)}{Abs_{AL}(\lambda)} \qquad (2.4)$$

where $Abs_{AL}(\lambda)$ is the incident photons absorption ratio of the active layers in solar cells. The IQE value is always higher than the EQE since the substrates reflection and absorption. A low IQE indicates that the active layer of the solar cell is poor to transfer the absorbed photons into the electron-hole pairs.

2.2.2 *Field Effect Transistor Measurement*

To investigate the charge transport properties of materials, one of the best approaches is measuring the charge carrier mobility (μ) from field-effect transistors (FET). The basic FET device structure is shown in **Figure 2.3**. It has three terminals, which are the source, drain, and gate electrodes. The device architecture can be simplified into a sandwich structure (metal/insulator/metal), considering source/drain electrodes and semiconductor as one "metal" layer, while the dielectric layer and gate electrodes could be described as the insulator and other metal respectively. This implies the field effect would be generated as long as the dielectric layer is inserted between two "metal" layers.

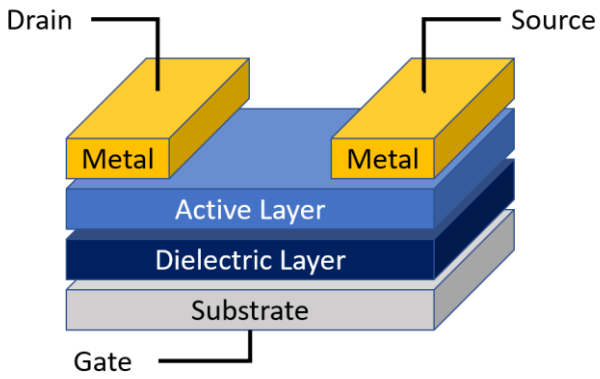

Figure 2.3. Basic field-effect transistor (FET) device architecture.

Mobility means the velocity of a charge carrier (hole or electron) under certain of applied electric field. The unit can be written as $cm^2V^{-1}s^{-1}$. Generally, organic materials have mobility around 10^{-2}-10^{-3} $cm^2V^{-1}s^{-1}$. The threshold voltage (V_{th}) is the gate-source voltage at which charge transport pathway is generated in the device. Many of factors could affect V_{th} value, including

energy level mismatch between electrodes and semiconductors, traps at the surface of the interface of semiconductors, dielectric constant of dielectric layers, etc.[75] The on/off current ratio (I_{on}/I_{off}) is determined by the ratio of the drain-source current at on/off states. The last parameter is the subthreshold swing (SS), which is the exponential behaviors of the drain-source current as a function of gate-source voltage. The unit for SS is $mVdec^{-1}$, describing how quickly the device turns on.

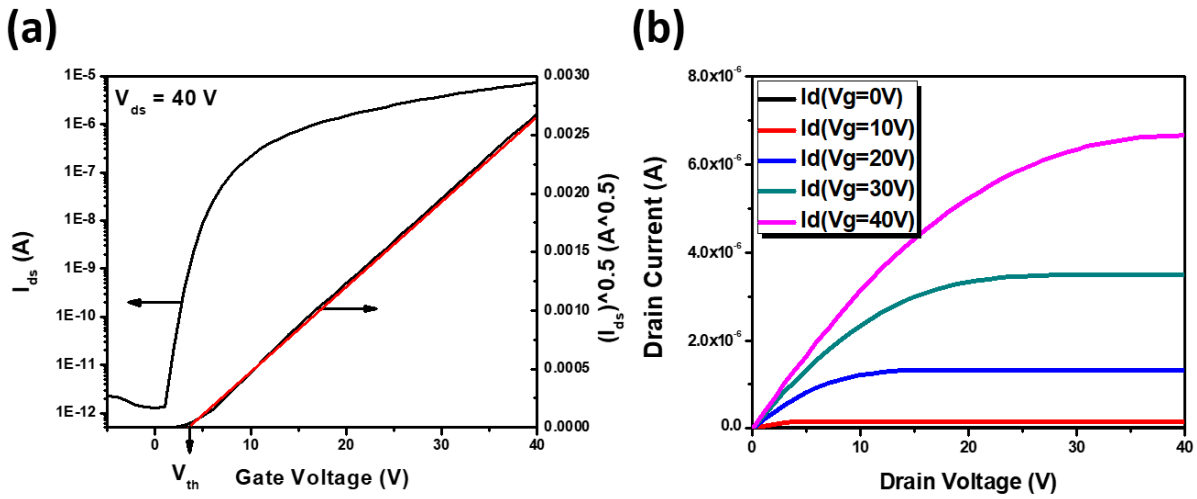

Figure 2.4. Representative (a) transfer and (b) output characteristic electrical curves of a standard PCBM OFET.

To correctly extract the mobility from the materials, there is sequence of electrical measurement steps. The first parameter needs to be determined is the capacitance, which can be derived from the capacitance-voltage (C-V) measurement. A typical device structure for this measurement is a metal-insulator-metal (MIM) architecture. From the C-V characterization, we could derive the material's dielectric constant from the following equation:

$$C_{ox} = \frac{\varepsilon_r \cdot \varepsilon_o}{d} \quad (2.5)$$

Where C_{ox} is the capacitance per unit area (F cm^{-2}), ε_r is the relative dielectric constant (3.9 for SiO_2), ε_o is the permittivity of free space, and d is the thickness of the dielectric layer. From the equation, it's clear to see the relation between C_{ox} versus the relative dielectric constant or the thickness of the dielectric. Since the V_{th} is determined by the value of C_{ox}, the operation voltage of the transistor could be reduced by increasing the materials ε_r or reduce the dielectric thickness.

Once the capacitance is calculated, the output curve would be measured as shown in **Figure 2a**. It measured I_{ds} while holding V_{gs} constant and varying V_{ds}. In the case of **Figure 2a**, V_{ds} is set as 40 V when measuring the relation between I_{ds} and V_{ds}. The mobility can be determined in either the linear or saturation regimes of the output curve measurement. The relationship between I_{ds}, V_{ds}, and V_{gs} can be expressed as follows:

linear regime:

$$I_{ds,lin}(\lambda) \quad = \frac{W}{L} \cdot C_{ox} \cdot \mu_{lin} \cdot [\,(V_{gs} - V_{th})\frac{V_{ds}}{2}] \cdot V_{ds} \tag{2.6}$$

Saturation regime:

$$I_{ds,sat}(\lambda) \quad = \frac{W}{2L} \cdot C_{ox} \cdot \mu_{sat} \cdot (V_{gs} - V_{th})^2 \tag{2.7}$$

Where W is the channel width, L is the channel length, C_{ox} is the capacitance per unit area of the dielectric, um is the charge carrier mobility in the linear regime, μ_{lin} is the charge mobility in the linear regime, and μ_{sat} is the charge mobility in the saturation regime. The charge carrier mobility can thus be determined in the saturation regime from the slope of the $(|I_{ds,sat}|)^{0.5}$ vs V_{gs}. In addition, the V_{th} can be determined as the x-intercept of the linear region in the $(|I_{ds,sat}|)^{0.5}$ vs V_{gs} plot.

Chapter 3. MORPHOLOGY ENGINEERING: TERNARY HALIDE FOR LARGE-BANDGAP PEROVSKITE PHOTOVOLTAICS

3.1 INTRODUCTION

As mentioned in the previous section, PVSCs have superior photovoltaic efficiency, where the record value reaches 22.1%.[77] To further push the PVSCs PCE, constructing a tandem solar cell is an effective approach since it could overcome the Shockley-Queisser limit for single junction cells.[78,79] Since tandem photovoltaics consisted with large- (1.7-1.8 eV) and small- (1.1-1.2 eV) bandgap cells, it critical to realizing an efficient large-bandgap PVSCs to couple with small-bandgap photovoltaics, like Si solar cells.

An effective way to control perovskite bandgap is thought the halide substitution (I, Br, or Cl) in composition. Several studies have demonstrated that a large-bandgap PVSC can be achieved by manipulating the ratio of iodide (I^-) and bromide (Br^-).[25–29] The bandgap of iodide-bromide mixed perovskites is ranged from 1.6 eV to 2.3 eV, enabling the narrowed absorption region required for employment in tandem architectures with the state-of-the-art inorganic solar cells for higher device efficiencies.

Though people could manipulate perovskite bandgap with halides substitution, the key challenge of realizing efficient large-bandgap PVSCs is controlling the perovskite film morphology. It has been proposed that the planar thin-film architecture's low performance may arise from pinholes formation.[80–82] These pinholes, the uncovered area of perovskite film, create device shorting pathways and lost light absorption in the active layer, resulting in low performance in perovskite efficiency. Zhao et al have demonstrated that the MA^+ rich environment could slow down the perovskite formation rate and, hence, the perovskite morphology become more

homogeneous.[83] Besides, the bandgap of the $MAPbI_3$ and $MAPbI_xCl_{3-x}$ are almost identical since the Cl^- anions would be driven out by the release of gaseous MACl during the annealing process. More importantly, Snaith et al. demonstrate that the diffusion length for $MAPbI_3$ perovskite formed by the precursor contained MACl salts is over 1 μm.[8,37] With a long diffusion length, the charge has a better possibility to be collected by metal electrodes. The previous findings imply that large-bandgap $MAPbI_xBr_{3-x}$ perovskites with Cl^- anions incorporation could improve its morphology and diffusion length, which greatly affects the photovoltaic device performance.

In this section, we describe the successful fabrication of highly efficient large-bandgap $MAPb(I_{1-y}Br_y)_xCl_{3-x}$ perovskite PHJ solar cells through a simple and low-temperature solution process. It is important to note that all of our scanning electron microscopy (SEM) EDS and X-ray photoelectron spectroscopy (XPS) analysis has indicated no measurable quantity of Cl^- remains in the material after annealing, but for convenience and clarity we will still refer to it as $MAPb(I_{1-y}Br_y)_xCl_{3-x}$ with the stipulation that if non-zero, $x \leq 0.025$ from the limitations of our equipment.[84] We found out perovskite crystal formation process changes dramatically when incorporating Cl^- into $MAPb(I_{1-y}Br_y)_3$ precursor. As a result, a smoother thin-film with greatly enhanced crystallinity and homogeneity was formed. This result was supported by the evidence in SEM and time-resolved X-ray diffraction (XRD). This improved perovskite thin-film morphology enables an elongated charge carrier lifetime and diffusion length from ~160 nm ($MAPb(I_{1-y}Br_y)_3$) to ~700-800 nm ($MAPb(I_{1-y}Br_y)_xCl_{3-x}$), as is revealed by transient photoluminescence (PL). For the device performance, large-bandgap PHJ PVSCs based on the ternary halide perovskite show much increased PCEs of 7.5-10.0%, outperforming the binary halide devices which exhibit typical PCEs of around 3.6%. Hence, this study becomes an important step stone for the future research of low cost, high efficiency, and solution processed tandem PVSCs.

3.2 EXPERIMENTAL

Fabrication of thin-film PVSCs

The device configuration is ITO/PEDOT:PSS/MAPb($I_{1-y}Br_y$)$_x$$Cl_{3-x}$/PCBM/$C_{60}$-bis/Ag. ITO-coated (15 Ω/sq) glass substrates were cleaned sequentially with a detergent, DI-water, acetone, and isopropanol. After drying by nitrogen blower, the ITO surface was treated with plasma for 30 s. PEDOT:PSS (Baytron 4083) was then spin-coasting on clean ITO substrates (~ 40 nm) and then baked at 150 ^{o}C for 10 min. The perovskite precursor solution was made by mixMAI and $PbCl_2$ powder in anhydrous dimethylformamide (DMF, Aldrich) with a molar ratio of 3:1. The perovskite/1,8-diiodooctane (DIO, Aldrich) solution was prepared via adding 1 wt% of DIO with respect to perovskite weight into the perovskite precursor solution. The solutions (40 wt%) were stirred overnight at 80 °C and filtered with 0.45 μm PVDF filters before device fabrication**.** To avoid moisture, the perovskite thin films were spin-coated 6k rpm for 45 s and then anneal 90°C for 2-3 hr in the N_2-filled glove box. Afterward, the PCBM (15 mg/ml in chloroform) and C_{60}-bis surfactant (2 mg/ml in isopropyl alcohol) were sequentially spin-coated at 1k rpm for 60 sand 3k rpm for 60s, respectively. Finally, silver electrodes with a 150 nm thickness were evaporated under high vacuum (<2× 10^{-6} Torr). For all perovskite devices, the active area was defined as 3.14mm^2. All the *J-V* curves in this study were recorded by using Keithley 2400 source measurement unit. The photocurrent was measured under illumination from a 450 W thermal Oriel solar simulator (AM 1.5G). The illumination intensity of the light source was accurately calibrated employing a standard Si photodiode detector equipped with a KG-5 filter, which can be traced back to the standard cell of National Renewable Energy Laboratory (NREL). The calibration method, based on the IEC-69094-1 spectrum, followed procedures described previously. The EQE spectra performed here are obtained by the IPCE measurement using the combination of a Xenon lamp

(Oriel, 450 W) as the light source, a monochromator, chopper with frequency of 100Hz, a lock-in amplifier (SR830, Stanford Research Corp), and a Si-based diode (J115711-1-Si detector) for calibration. The absorption and transmission spectra were measured using a Perkin-Elmer Lambda-9 UV-visible spectrophotometer. Tapping-mode AFM images were taken on a Veeco multimode AFM with a Nanoscope III controller

PL measurement

Glass substrates were cleaned sequentially in detergent, DI water, acetone, iso-propanol and oxygen plasma. PEDOT:PSS aqueous solution was filtered and spin-coated on glass at 5000 rpm for 40s and then annealed at 150 °C for 10 min. Methylammonium iodide and lead (II) chloride were dissolved under heating in anhydrous DMF at a 3:1 molar ratio of MAI to $PbCl_2$, with final weight percent of 40%. And methylammonium bromide and lead (II) chloride were dissolved under heating in anhydrous DMF at a 3:1 molar ratio of MABr to $PbCl_2$, with final weight percent of 33%. Later they were mixed with a different ratio. The precursors were then filtered and spin-coated on the glass or glass/PEDOT:PSS substrate at 6000rpm inside the glove box. After spin-coating, the $CH_3NH_3Pb(I_yBr_{1-y})_xCl_{3-x}$ films stayed for 30 min before annealed at 90°C for 120 minutes. The capping layers were then deposited via spin-coating chloroform solutions of 10mg/ml poly(methylmethacrylate) (PMMA) or 15mg/ PCBM at 1000rpm.

Time-resolved PL measurements were measured by a time-correlated single photon counting (TCSPC) system (FluoTime 100, PicoQuant GmbH). Samples were photoexcited using a 467 nm laser beam (LDH-P-C-470, PicoQuant GmbH) pulsed at frequencies between 0.25-10MHz, with a pulse duration of 60 ps and fluence of ~10 nJ/cm^2, to avoid nonlinear effects such as exciton-charge annihilation. And the emission light was collected after passing a 665 nm long-pass filter to block reflected excitation laser.

3.3 RESULT AND DISCUSSION

3.3.1 *Morphology Comparison and Crystallization Study*

To investigate the variation of optical properties of the organic-inorganic tri-halide hybrid perovskite, we measure the UV-visible absorption spectra of $MAPb(I_{1-y}Br_y)_3$ and $MAPb(I_{1-y}Br_y)_xCl_{3-x}$ ($0<Y<0.4$), as shown in **Figure 3.1**. Without the incorporation of Cl^- ions, the onset absorption band of perovskite can be tuned from 800 nm wavelength (1.55eV) to 700 nm wavelength (1.77eV) as y increasing from 0 to 0.4. The redshift of the band edge of perovskite agrees well with previously published results. [28,85,86] It's worth noting that the baseline of binary halides perovskite elevated as perovskite contains a higher proportion of I^- anions. The possibly contributed factors of this phenomenon might be the scattering effect caused by the roughness of the surface. On the other hand, by incorporating chloride ions into perovskite, the onset absorption band of $MAPb(I_{1-y}Br_y)_xCl_{3-x}$ can be tuned from a 770 nm wavelength (1.61eV) to 680 nm wavelength (1.82eV) as y increasing from 0 to 0.4, as shown in **Figure 3.1** illustrated the range of bandgap tunability of $MAPb(I_{1-y}Br_y)_xCl_{3-x}$ is similar the $MAPb(I_{1-y}Br_y)_3$. Additionally, the relatively low baseline of UV-vis spectrum of $MAPb(I_{1-y}Br_y)_xCl_{3-x}$ indicated that a better thin film morphology is formed because of the low scattering effect caused by a uniform perovskite thin film morphology formed by Cl^- inclusion.

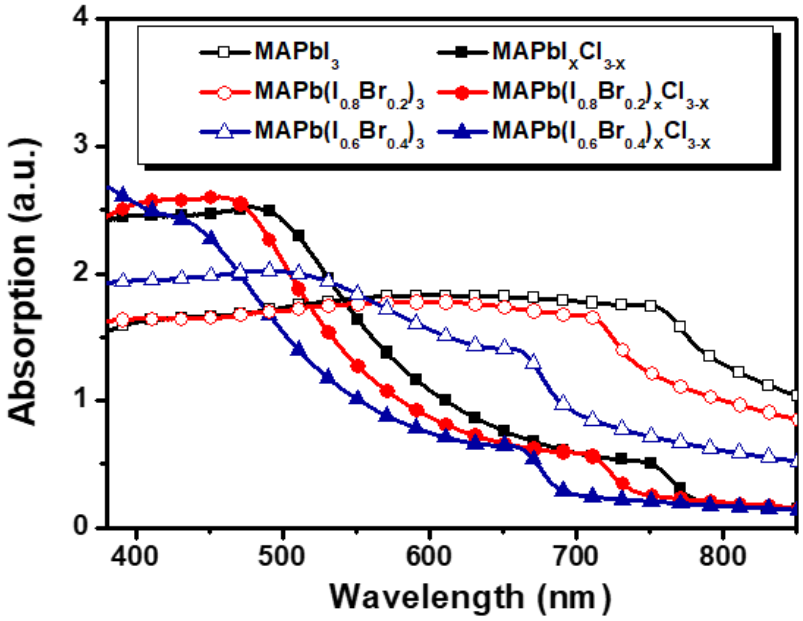

Figure 3.1. UV-vis spectra of $MAPb(I_{1-y}Br_y)_xCl_{3-x}$ (y=0, 0.2, 0.4).

This assumption is confirmed by the top view SEM images, as shown in **Figure 3.2**. The first three figures, **Figure 3.2a-c**, are the morphology of the perovskite $MAPb(I_{1-y}Br_y)_3$ (y=0, 0.2, 0.4) and the following three figures, **Figure 3.2d-f** are the morphology of the perovskite with chloride ions incorporation $MAPb(I_{1-y}Br_y)_xCl_{3-x}$ (y=0, 0.2, 0.4). The thin film morphologies of $MAPb(I_{1-y}Br_y)_xCl_{3-x}$ are uniform and near 100% surface coverage. Fewer pinholes appeared on thin film morphology means that the less possibility of the contact between the PEDOT:PSS and PCBM and hence reduce the recombination sites in the perovskite thin film. Therefore, the V_{oc} and J_{sc} of $MAPb(I_{1-y}Br_y)_3$ based photovoltaics could be further enhanced by incorporated Cl^- into perovskite and result in higher efficiency in the planar solar cells.

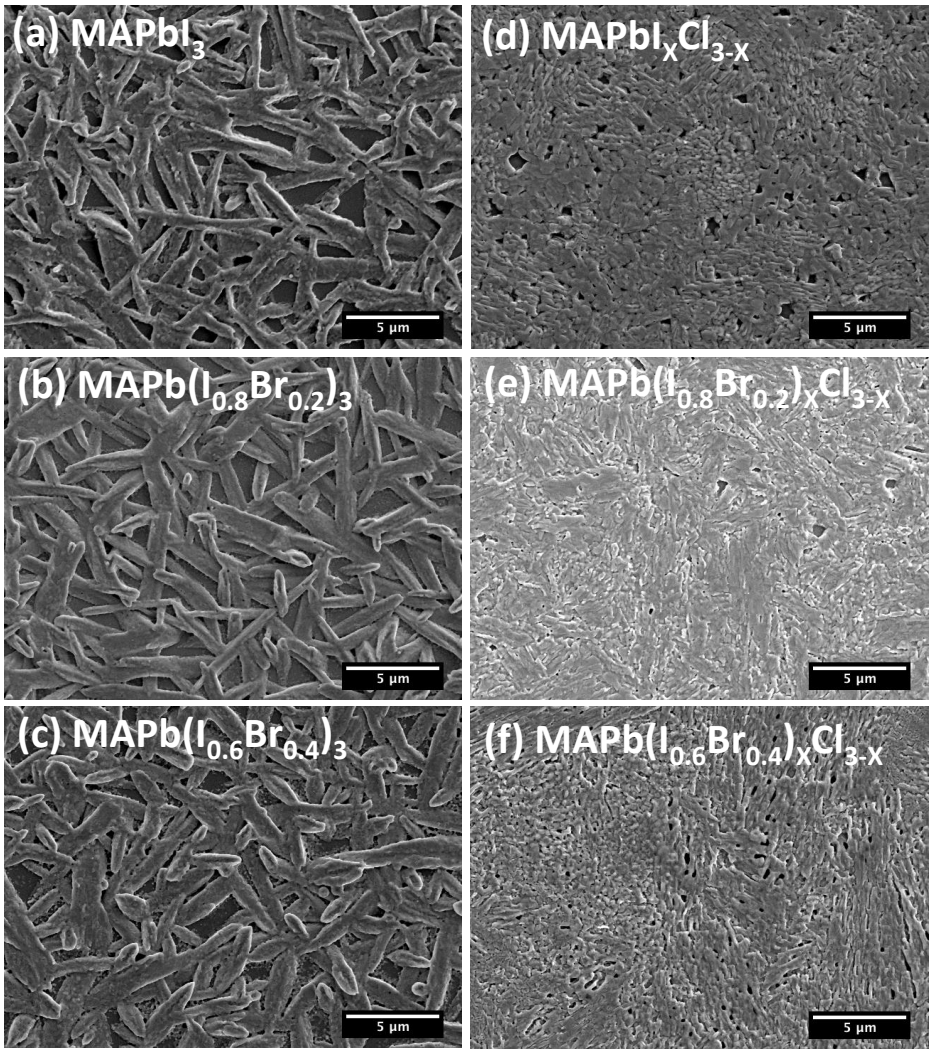

Figure 3.2. SEM images of the surface of (a-c) $MAPb(I_{1-y}Br_y)_3$, where y=0, 0.2, 0.4, and (d-f) $MAPb(I_{1-y}Br_y)_xCl_{3-x}$, where y=0, 0.2, 0.4. All these samples are prepared on ITO/PEDOT:PSS substrates.

XRD has also been carefully studied. $MAPbI_xCl_{3-x}$ can be indexed into tetragonal perovskite structure with I4cm symmetry, while $MAPb(I_{0.8}Br_{0.2})_xCl_{3-x}$ and $MAPb(I_{0.6}Br_{0.4})_XCl_{3-X}$ can be indexed into cubic perovskite phase with Pm-3m symmetry, agreeing well with the structure of pure $MAPbI_3$ and pure $MAPbBr_3$ at room temperature, respectively. **Figure 3.3a** shows an enlarged XRD pattern in the range of 28.0°-29.2°. For $MAPbI_xCl_{3-x}$, there are two peaks at 28.2°

and 28.4°, corresponding to the diffraction of (004) and (220) planes, respectively. After the introduction of 0.2 portions of Br^- to replace I^-, the phase evolved from tetragonal to cubic. The two peaks at 28.2° and 28.4° disappear and a single peak rises up at 28.7° corresponding to the diffraction of (200) plane in the Pm-3m space group. The similar phase transformation after replacement of I^- with Br^- has been reported by Seok's team.[28] When the portion of Br^- increases to 0.4, this peak further moved to $2\theta = 29.0°$. This peak shift toward higher 2θ indicated the shrink of lattice after replacing the larger I anion with smaller Br anion.

To elucidate the role of Cl^- in the crystallization process, we have studied phase compositions at different annealing times with XRD, as demonstrated in **Figure 3.3b**. After spin-coating the $MAPbI_xCl_{3-x}$ precursor solutions onto the substrates, ions in the precursor solutions immediately begin to self-assemble into the $MAPbCl_3$ perovskite structure before annealing as demonstrated by XRD peak at $2\theta = 15.7°$ (**Figure 3.3b**). After annealing for 30 min, the intensity of this peak started to decrease, while a peak corresponding to iodide based organometal perovskites (at $2\theta = 14.2°$) arose. This trend kept consistent as annealing process continued. After 2 h, the peak for $MAPbCl_3$ phase disappeared completely, and the $MAPb(I_{0.8}Br_{0.2})_3$ peak evolved into a strong and sharp peak, indicating high crystalline feature.

This XRD study shows that chloride ions change the transformation pathway during annealing by introducing the competition between chloride based perovskite phase and iodide based perovskite phase. This alteration in growth pathway likely influences overall transformation routes in addition to modulating the resulting morphology as compared to pure lead systems. Although as of now the exact mechanism by which chloride inclusion enhances ultimate material properties is inadequately understood, it is an active research area in the field. As demonstrated by Colella et al., both iodide and chloride based perovskite lattices can co-exist at equilibrium after annealing,

however, if Pb^{2+} is the limiting species, it will preferentially coordinate with iodide in the perovskite lattice.[24] This also explains why there is a little portion of Cl^- in the EDS result (**Table 3.1**), while I^- and Br^- ratio kept the same as in perovskite precursor.

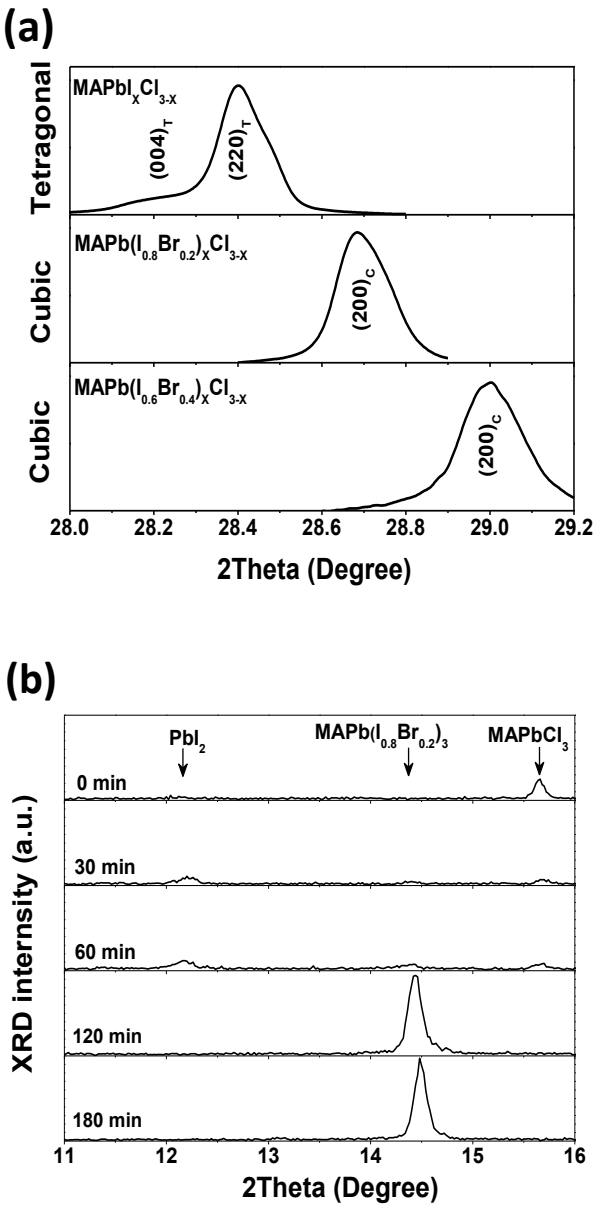

Figure 3.3. (a) Magnified X-ray diffraction (XRD) patterns of $MAPb(I_{1-y}Br_y)_xCl_{3-x}$, where y=0, 0.2, 0.4, in the region of tetragonal $(004)_T$ and $(220)_T$ and cubic $(200)_C$ peaks (2θ = 28-29.2°). (b)Time resolved XRD analysis of $MAPb(I_{0.8}Br_{0.2})_xCl_{3-x}$.

Table 3.1. The summary of electronic data systems (EDS) of $MAPb(I_{1-y}Br_y)_3$ and $MAPb(I_{1-y}Br_y)_xCl_{3-x}$.

	Pb	**I**	**Br**	**Cl**		**Pb**	**I**	**Br**	**Cl**
	1.5	4.1	0	0		1.1	3	0	*
$MAPbI_3$	1.4	4.1	0	0	**$MAPbI_xCl_{3-x}$**	1	2.8	0	*
	1.4	3.9	0	0		1.1	3	0	*
Average	1.4	4			**Average**	3.2	8.8		
Ratio		100%			**Ratio**		100%		
	1.5	3.3	0.8	0		1.2	2.7	0.7	*
$MAPb(I_{0.8}Br_{0.2})_3$	1.5	3.4	0.8	0	**$MAPb(I_{0.8}Br_{0.2})_xCl_{3-x}$**	1	2.4	0.7	*
	1.4	2.9	0.7	0		1.1	2.4	0.5	*
Average	1.5	3.2	0.8		**Average**	1.1	2.5	0.6	
Ratio		81%	19%		**Ratio**		80%	20%	
	1.5	2.5	1.5	0		1	1.7	1.2	*****
$MAPb(I_{0.6}Br_{0.4})_3$	1.4	2.5	1.5	0	**$MAPb(I_{0.6}Br_{0.4})_xCl_{3-x}$**	1.1	1.7	1.2	*****
	1.3	2.4	1.5	0		1	1.6	1.2	*****
Average	1.4	2.5	1.5		**Average**	1	1.7	1.2	
Ratio		62%	38%		**Ratio**		58%	42%	

***** The content is too low to be detected.

3.3.2 *Diffusion Length Estimation*

Figure 3.4a-b shows the time-resolved PL for $MAPb(I_{1-y}Br_y)_xCl_{3-x}$ when y = 0.2 and y = 0.4. The intensity of the excitation laser was kept small at approximately 10 nJ cm^{-2}/pulse to reduce the chance of nonlinear effects, such as auger recombination or exciton-charge annihilation. The thickness of the $MAPb(I_{1-y}Br_y)_xCl_{3-x}$ films was measured with a profilometer, which is approximately 250 ± 50 nm, which is equal to the thickness of the perovskite layer in our solar cell devices. The PL decay of $MAPb(I_{1-y}Br_y)_xCl_{3-x}$ without quencher showed time-constant of 130 ± 3 ns when y = 0.2 and 74 ± 13 ns when y = 0.4, by fitting a single exponential decay equation. The decay time-constant is significantly decreased if electron quencher (PCBM) and hole quencher (PEDOT:PSS) were added. In the case y = 0.2, the decay time-constant were 9.3 ± 1.0 ns and 7.1 ± 0.2 ns, with PEDOT:PSS and PCBM layer, respectively. And in the case y = 0.4, the decay time-constant were 3.8 ± 0.1 ns and 4.4 ± 0.1 ns, with PEDOT:PSS and PCBM layer, respectively.

The time-resolved PL decay measurements were modeled with 1-D diffusion equation. The spatial and temporal distribution of electrons and holes in the film n(x, t) is given by

$$\frac{\partial n(x,t)}{\partial t} = D\frac{\partial^2 n(x,t)}{\partial x^2} - k(x,t)n(x,t) \tag{3.1}$$

where D is the diffusion coefficient for electrons or holes, and k(x,t) is the recombination rate of the carriers. The electron and hole concentration were assumed to be equal since we assumed the perovskite is an intrinsic semiconductor. The initial distribution of excitons was assumed to be:

$$n(x,\ 0) = \mathrm{n_o}e^{Ax} \tag{3.2}$$

where A is the absorbance of the perovskite layer at 467 nm and the incident light beam is perpendicular to the device substrate. The effect of the quenching layer (PCBM or PEDOT:PSS) was included by assuming that all carriers which reach the interface are 100% quenched. Hence,

the boundary condition is n(L, t) = 0, where L is the interface of perovskite and quencher. The average diffusion length, where τ_{rec} is the recombination lifetime without quencher. Since the binding energy of perovskite is small (20~50 meV), we assume that free carriers are generated inside perovskite films upon photoexcitation. Therefore, the diffusion coefficients for holes and electrons can be estimated by the time-resolved PL decay with hole or electron quenchers. Fitted curves from the diffusion model are shown in **Figure 3.4a-b**, and the parameters are summarized in **Table 3.2**. The diffusion length for both electrons and holes are larger than 800 nm, which is very close to previous reported value of 1 μm by Snaith et al for $MAPbI_xCl_{3-x}$.[8] This indicates that the addition of Br^- in this mixed halide system does not significantly shorten the diffusion length. Because the electron and hole diffusion length are longer than the film thickness (250 nm), most of the excited charges can reach the quenching layer before recombination. Therefore, the charge collection is efficient in $MAPb(I_{1-y}Br_y)_xCl_{3-x}$ system. As a result, the EQE of $MAPb(I_{0.8}Br_{0.2})_xCl_{3-x}$ still remain as high as $MAPbI_xCl_{3-x}$ (**Figure 3.5b**). When the Br ratio increased to 40%, the decay time-constant decreased, probably due to more defects or potential interface between I-riched and Br-riched phase. The electron and hole diffusion length is smaller when y = 0.4 comparing to y = 0.2, which indicates a larger chance of recombination of excited carriers, thus a smaller EQE. However, the EQE of perovskite with y = 0.4 is much smaller than y = 0.2. Therefore the difference of the diffusion coefficient may not be the only reason for the small EQE. Other potential mechanisms need to be further investigated.

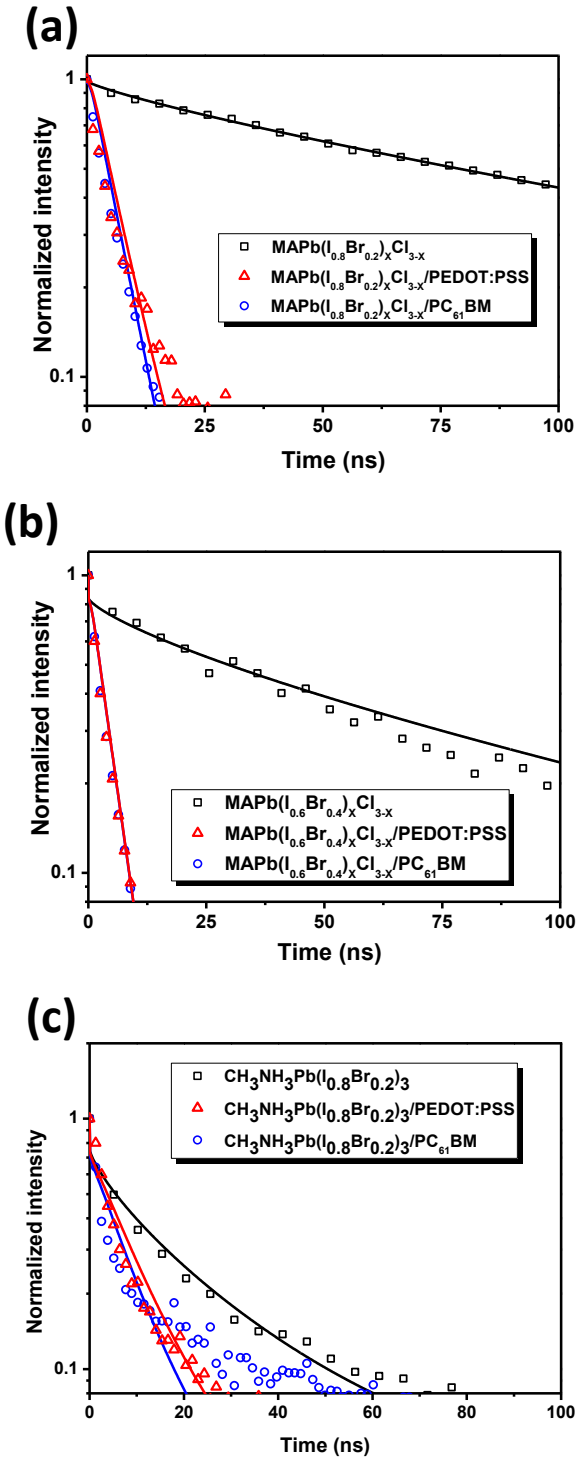

Figure 3.4. Time-resolved PL measurements and fitted curves to the diffusion model for the (a) $MAPb(I_{0.8}Br_{0.2})_xCl_{3-x}$, (b) $MAPb(I_{0.6}Br_{0.4})_xCl_{3-x}$, and (c) $MAPb(I_{0.8}Br_{0.2})_3$, without quencher (black squares) or with the presence of hole quencher (PEDTO:PSS, red triangle) or electron quencher (PCBM, blue circle).

Table 3.2. Diffusion constants (D) and lengths (L_D) from the fitted PL decays via the diffusion model described in SI. The errors can be ascribed predominantly from perovskite film thickness variations of ±50 nm.

Perovskite	Y	Hole Diffusion Coefficient (cm^2s^{-1})	Electron Diffusion Coefficient (cm^2s^{-1})	Hole Diffusion Length (nm)	Electron Diffusion Length (nm)
$MAPb(I_{1-y}Br_y)_3$	0.2	$1.5 \pm 0.7 \times 10^{-2}$	$1.7 \pm 0.7 \times 10^{-2}$	159 ± 32	166 ± 34
$MAPb(I_{1-y}Br_y)_xCl_{3-x}$	0.2	$4.7 \pm 2.1 \times 10^{-2}$	$5.1 \pm 2.3 \times 10^{-2}$	770 ± 154	804 ± 161
	0.4	$7.2 \pm 3.1 \times 10^{-2}$	$7.2 \pm 3.2 \times 10^{-2}$	721 ± 143	722 ± 144

In the papers reported by Snaith et al., the electron and hole diffusion length of tri-iodide perovskite $MAPbI_3$ is about 100 nm, which is one magnitude smaller than mixed halide perovskite.[8] In our perovskites, we observed similar trends. The hole diffusion length of $MA(I_{1-y}Br_y)_3$ is 102 nm and 147 nm, for Y = 0.2 and Y = 0.4, respectively. The diffusion length is smaller than the film thickness, thus the charge collection efficiency is lower, which is reflected by the low short-circuit current of the $MAPb(I_{1-y}Br_y)_3$ devices.

3.3.3 *Device Performance*

Given the improved properties of ternary halide perovskites, a conventional PHJ configuration of ITO/PEDOT:PSS (35-40 nm)/perovskite (~250 nm)/PCBM (~55 nm)/Bis-C_{60} (10 nm)/Ag (150 nm) is employed to realize the photovoltaic performance. The prominent advantages of this architecture lie in the efficient electron/hole extraction and complete low-temperature solution processability.[70,87–92] Note that the employment of Bis-C_{60}, an efficient electron-selective interfacial layer, enables the energy alignment between PCBM and the cathode, allowing the usage of stable Ag as the top electrode.[93,94] **Figure 3.5a** presents the current *J-V* curves of the studied devices under 1 sun AM 1.5 simulated solar irradiation, and the relevant photovoltaic parameters

are summarized in **Table 3.3**. Encouragingly, all the ternary halide perovskite devices show significantly enhanced photovoltaic performance and better reproducibility compared to their pristine binary counterparts with regard to the smooth thin-film with nearly 100% surface coverage. The MAPb($I_{0.8}Br_{0.2}$)$_x$$Cl_{3-x}$ device with an bandgap of 1.7 eV exhibits a promising PCE_{max} of 10.0% with a V_{oc} of 0.99 V, a J_{sc} of 14.9 mA/cm^2, and a FF of 0.68 while the MAPb($I_{0.8}Br_{0.2}$)$_3$ device shows a poor PCE_{max} of 3.6% with a V_{OC} of 0.88 V, a J_{SC} of 10.9 mA/cm^2, and a FF of 0.38. As the substituting Br portion increases to Y = 0.4, the ternary halide device still possesses a decent PCE_{max} of 7.6% (V_{oc}: 1.06 V; J_{sc}: 11.5 mA/cm^2; FF: 0.62), outperforming the pristine binary halide counterpart with a PCE_{max} of 3.7% (V_{oc}: 0.92 V; J_{sc}: 10.5 mA/cm^2; FF: 0.38). It is interesting to point out that no severe hysteresis is observed for the studied devices. This result suggests this kind of p-i-n PHJ architecture has limited charge traps across each interlayer.[88,89] Besides, the EQE curves shown in **Figure 3.5b** affirm the enlarged bandgap of the studied perovskites. The shifted trend of the absorption edge in EQE coincides with that observed in the UV-vis spectra (**Figure 3.1b**).

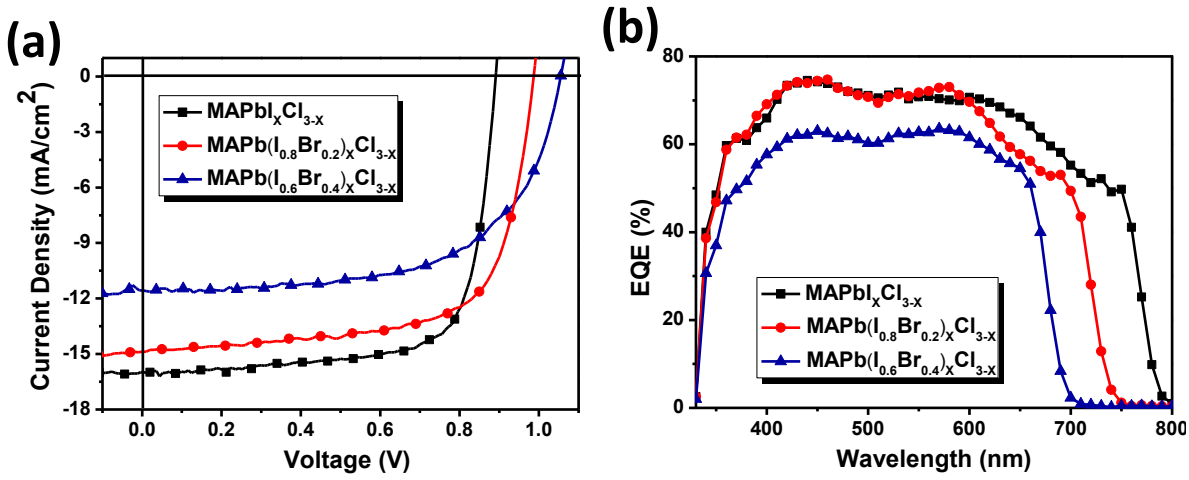

Figure 3.5. (a) The *J-V* curves, (b) EQE spectra of the studied PHJ MAPb($I_{1-y}Br_y$)xCl_{3-x} solar cells, where y=0, 0.2, 0.4 under 100 mW cm^{-2} AM1.5 illumination.

Table 3.3. The summarized best photovoltaic performance of the studied perovskite solar cells.

	V_{oc} (V)	J_{sc} (mA/cm^2)	FF	PCE (%)	E_g
$MAPbI_3$	0.85	10.6	0.38	3.4	1.55
$MAPbI_{0.8}Br_{0.2}$	0.88	10.9	0.38	3.6	1.65
$MAPbI_{0.6}Br_{0.4}$	0.92	10.5	0.38	3.7	1.74
$MAPbI_xCl_{3-x}$	0.89	16.0	0.74	10.5	1.61
$MAPb(I_{0.8}Br_{0.2})_xCl_{3-x}$	0.99	14.9	0.68	10.0	1.70
$MAPb(I_{0.6}Br_{0.4})_xCl_{3-x}$	1.06	11.5	0.62	7.6	1.83

Noticeably, the slightly lower performance of $MAPb(I_{0.6}Br_{0.4})_xCl_{3-x}$ than $MAPb(I_{0.8}Br_{0.2})_xCl_{3-x}$ might arise from the narrower light-harvesting region and mismatched energy levels with adjacent p/n heterojunctions, while the charge carrier diffusion length of both perovskites is comparable. As reported in the literatures,[14,28,95,96] the increased bandgap of $MAPbBr_3$ (2.3 eV) originates from a simultaneous upshift of conduction band (from -3.93 eV to -3.38 eV) and downshift of valence band (from -5.46 eV to -5.68 eV) relative to the pristine $MAPbI_3$ (1.5 eV). Note that the inclusion of Cl^- has been demonstrated to have a subtle influence on the optoelectronic properties of the resultant perovskite due to the preferential occupancy at the apical position of Pb.[14] In our studied PHJ configuration, the energy levels of $MAPbI_3$ and $MAPbI_xCl_{3-x}$ (HOMO: -5.46 eV and LUMO: -3.93 eV) align well with the employed PEDOT:PSS (work function (WF): ~-5.2 eV) and $PC_{61}BM$ (WF: -4.2 eV), enabling the efficient charge dissociation and extraction. Nevertheless, the energy levels of $MAPb(I_{1-y}Br_y)_xCl_{3-x}$ will gradually drift from those of the adjacent hetero-junctions as the Br^- fraction increases, due to the shift induced by the increase of bandgap. This inevitably results in an interfacial potential barrier and restrains the resulting V_{oc} despite the increase of bandgap.[95] On the other hand, the relatively narrow light-harvesting region of $MAPb(I_{0.6}Br_{0.4})_xCl_{3-x}$ leads to the low J_{sc} compared to $MAPb(I_{0.8}Br_{0.2})_xCl_{3-x}$.

As a result, the performance drops from 10% to ~8% as the substituting Br portion increases from 20% to 40%.

The enhancement in performance from binary halide to ternary halide perovskites is attributed to the increased charge carrier diffusion length as a result of improved thin-film morphology. Considering its influence in relation to charge dissociation, the relationship of V_{oc}/ E_g ratio and FF between binary and ternary halide perovskite is summarized in **Figure 3.6**.[26,27] It clearly reveals that the binary system suffers great potential loss (ratio below 0.54; $E_g - qV_{oc}$ = 0.77-0.82 eV), as reflected in the small increase of V_{oc} (from 0.85 V to 0.92 V while the bandgap of perovskite increases from 1.55 eV to 1.74 eV), as well as poor FF. However, the potential loss is effectively reduced for the ternary system (ratio above 0.58; $E_g - qV_{oc}$ = 0.71-0.79 eV). As a result, the resultant V_{oc} and FF are significantly improved, enabling the high performance achieved in the PHJ devices.

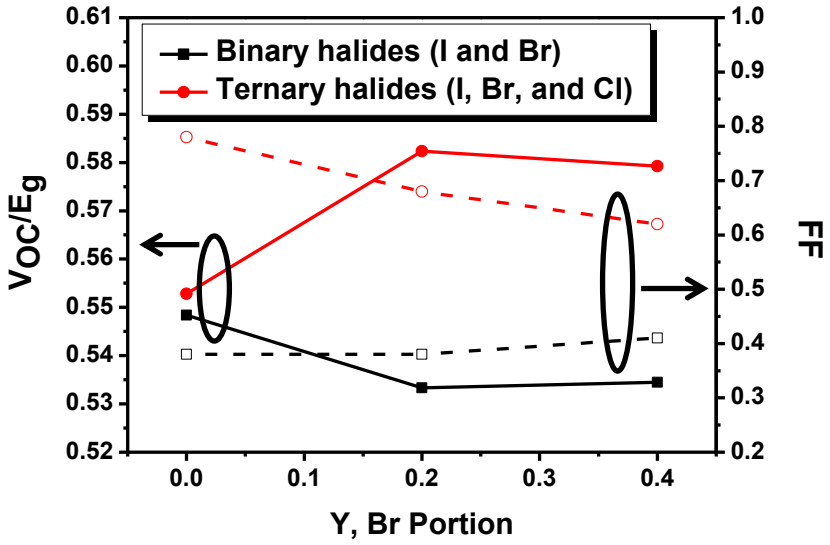

Figure 3.6. Variation of V_{oc}/E_g and FF of the studied PHJ MAPb($I_{1-y}Br_y$)xCl_{3-x} solar cells, where y=0, 0.2, 0.4 under 100 mW cm^{-2} AM1.5 illumination.

3.4 SUMMARY

In summary, we have demonstrated a high efficient large bandgap (1.7eV) perovskite solar cell based on planar hetero-junction structure through ternary halides (I/Br/Cl) perovskite composition. Cl anions play an important role to control the morphology and charge carrier lifetime of $MAPb(I_{1-y}Br_y)_xCl_{3-x}$ thin film formation with little affection on the final perovskite composition. As a result, the large bandgap PVSCs performance was greatly improved. The ternary halide perovskite discussed in this paper offer a stable and simple platform for the development of future perovskite technology, like perovskite tandem solar cell.

Chapter 4. MORPHOLOGY ENGINEERING: ADDITIVE ENHANCED CRYSTALLIZATION FOR EFFICIENT PEROVSKITE PHOTOVOLTAICS

4.1 INTRODUCTION

At the early stage of the organometal PVSCs research, a key issue needs to be overcome is the perovskite thin film quality. Homogeneity of the perovskite thin film have been considered as an important factor to evaluate quality since it regarding to the charge recombination rate and photon absorption, which is determine the device performance.[64,87,97,98] The perovskite thin film morphology can be affected by many factors, including the substrate surface energy, solution concentration, precursor composition, solvent choice, and deposition temperature.[64,87,97,98] For example, we demonstrated that the morphology of $MAPbI_3$ and $MAPbI_xBr_{3-x}$ could be modified by introducing Cl^- anion into perovskite precursor.[99] A continuous perovskite thin films were generated and leading to the improved device performance.

Encouraged by the previous result, we attempted to develop a novel approach to further enhance the perovskite thin film morphology of solution processed perovskite. Though rationally adding a small amount of additive, the perovskite crystallization path can be effectively manipulated, and so do the morphology. A temporary chelation of Pb^{2+} by the bidentate halogenated additives during crystal growth is evidenced by the improved solubility of $PbCl_2$ in the presence of 1,8-diiodooctane (DIO). The chelation encourages homogeneous nucleation and likely modifies interfacial energy favorably, ultimately altering the crystal growth path. As a result, the morphology of the perovskite thin films processed from the DIO contained precursor shows a much smoother and more continuous surface than that obtained from the pristine solution, as is

illustrated in **Figure 4.1**. The homogeneity formed under the influence of this halogenated additive lead to very promising PCEs close to 12% in planar-heterojunction perovskite solar cells.

4.2 EXPERIMENTAL

Planar Heterojunction PVSCs Fabrication Method

The devices were fabricated in the configuration of ITO or FTO/PEDOT:PSS/$MAPbI_{3-x}Cl_x$/PCBM/$C_{60\text{-bis}}$/Ag. ITO and FTO glass substrates were cleaned sequentially with detergent and deionized water, acetone, and isopropanol under sonication for 10 minutes. After drying under an N_2 stream, substrates were further cleaned by a plasma treatment for 30 s. PEDOT:PSS (Baytron P VP Al 4083, filtered through a 0.45 μm nylon filter) was first spin-coated onto the substrates at 5k rpm for 30 s and annealed at 150°C for 10 min in air. To avoid oxygen and moisture, the substrates were transferred into an N_2-filled glovebox, where the thin-film perovskite layers were spin-coated from a homogeneous 40 wt% $MAPbI_{3-x}Cl_x$ and $MAPbI_{3-x}Cl_x$ with 1wt% DIO precursor solution at 6k rpm for 45 s (300-500 nm thickness) and then annealed at 90℃ for 2~3 hours. Afterward, the PCBM (15 mg/mL in chloroform) and C_{60}-bis surfactant (2 mg/mL in isopropyl alcohol) were then sequentially deposited by spin coating at 1k rpm for 60 s and 3k rpm for 60 s, respectively. Silver electrodes with a thickness of 150 nm were finally evaporated under high vacuum (<2 x 10^{-6} Torr) through a shadow mask. The device area is defined as 3.14 mm^2. All the *J-V* curves in this study were recorded using a Keithley 2400 source meter unit. The device photocurrent was measured under AM1.5 illumination condition at an intensity of 100 mW cm^{-2}. The illumination intensity of the light source was accurately calibrated with a standard Si photodiode detector equipped with a KG-5 filter, which can be traced back to the standard cell of the National Renewable Energy Laboratory (NREL). The EQE spectra performed here were obtained from an IPCE setup consisting of a Xenon lamp (Oriel, 450 W) as the light source, a

monochromator, a chopper with a frequency of 100Hz, a lock-in amplifier (SR830, Stanford Research Corp), and a Si-based diode (J115711-1-Si detector) for calibration.

Time-Resolved PL Measurements

Time-resolved PL measurements were measured by a time-correlated single photon counting (TCSPC) system (FluoTime 100, PicoQuant GmbH). Samples were photoexcited using a 467 nm laser beam (LDH-P-C-470, PicoQuant GmbH) pulsed at frequencies between 0.5-10MHz, with a pulse duration of 60 ps and fluence of ~10 nJ/cm^2, to avoid nonlinear effects such as exciton charge annihilation. The lifetime was obtained by fitting the PL measured from perovskite films with a bi-exponential decay function of the form:

$$\mathrm{l}(t) = A_1 e^{-t/\tau_1} + A_2 e^{-t/\tau_2}$$

4.3 Result and Discussion

4.3.1 *Morphology Effects*

An inverted p-i-n heterojunction architecture of ITO or FTO/PEDOT:PSS (35~40 nm)/$CH_3NH_3PbI_{3-x}Cl_x$ (~400 nm)/PCBM (~55 nm)/Bis-C_{60} (10nm)/Ag (150 nm) was adopted to study the influence of perovskite thin-film morphology on device performance. The PEDOT:PSS and PCBM interlayers guaranteeing sufficient charge dissociation and extraction for the photoexcited charge carriers generated in perovskite active layer. Notably, the Bis-C_{60} surfactant is employed as an efficient electron-selective interfacial layer that aligns the energy levels at the organic/cathode interface and enables the utilization of stable metals such as Ag as the top electrodes, providing respectable environmental stability.[93,94] The mixed halide $CH_3NH_3PbI_{3-x}Cl_x$ perovskite was chosen for study by virtue of the fore mentioned merits demonstrated in the previous chapter.[99] The detailed information regarding the preparation of the perovskite precursor

solution, deposition of the perovskite thin-film, and the fabrication of devices is described in the experimental section.

The approach of solvent additives has already been demonstrated in modulating the morphology of bulk heterojunction (BHJ) OPVs. Bazan *et al* first reported that the morphology of BHJ layers could be effectively optimized by simply incorporating additives like alkane dithiols or 1,8-di(R)octanes into the processing solution.[100,101] The reasons why these processing additives can effectively change the BHJ morphology are because of the selective solubility of fullerenes and the increased boiling point with respect to the host solvent. Inspired by this achievement, we are interested in exploring the additive's influence on both the crystallization of perovskite thin films and device performance. The additive studied here is DIO as it bears iodine in common with $CH_3NH_3PbI_{3-x}Cl_x$ and as a soft Lewis base may interact with Pb^{2+}, a soft Lewis acid. We hypothesize that this additive can temporarily coordinate Pb^{2+} during crystal growth and modulate crystallization path as the transient capture of additive in the growing crystal lattice will increase both the internal energy and entropy of the crystals.[9,24,75]

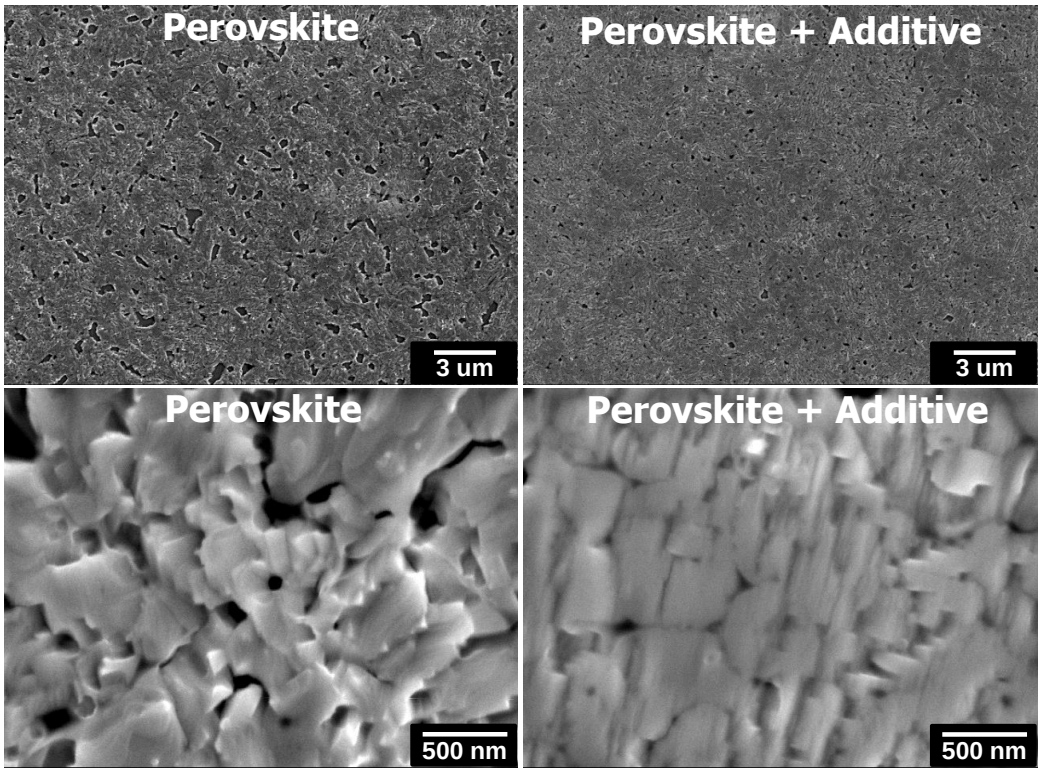

Figure 4.1. SEM images of the $CH_3NH_3PbI_{3-x}Cl_x$ layer with and without additive.

The DIO additive was mixed into the precursor solution prior to spin-coating deposition and the optimized blending ratio was found to be around 1 wt % with respect to the weight of perovskite. The performance of the device made with the new approach showed about 30% improvement compared to the control device. **Table 4.1** is a summary of device parameters, including V_{oc}, J_{sc}, FF, and PCE. The control device fabricated from the pristine composite solution showed a PCE of 7.8% with a V_{oc} of 0.90 V, a J_{sc} of 15.0 mA/cm^2, and a FF of 58.1% while that derived from the solution containing 1% DIO exhibited a significantly enhanced PCE of 10.3% with a V_{oc} of 0.92 V, a J_{sc} of 15.6 mA/cm^2, and an FF of 71.3%. This encouraging result highlights the DIO additive positive effects on PVSCs. In addition, the extended annealing time for the perovskite precursor contained DIO implies the perovskite crystallinity has been changed. It is well known that the crystallinity of perovskite absorber domains determines ultimate performance

of the fabricated devices since defects in the crystals will create severe shorting and trapping sites for charge recombination. Crystallinity will also greatly affect the efficiency of charge dissociation, transport, and diffusion length.[9,90] As evidenced in **Figure 4.1**, the film prepared from the 1% DIO solution showed higher coverage, less surface roughness, and more regular crystallites with more ordered growth directions than the pristine thin film. It is worthwhile to point out that the high V_{oc} over 0.90 V for both devices implies the small potential loss for exciton dissociation (band-gap of $CH_3NH_3PbI_{3-x}Cl_x$ is ~1.5 eV, estimated from **Figure 4.3a**). This highlight prominent benefits of perovskites: small exciton binding energy (< 20 meV) and respectable ambipolar charge conduction.[8,9,37,75,90,91,102,103] The high FF of over 70% further demonstrates the efficient charge transfer and extraction of such a planar p-i-n heterojunction.[90,91]

The dependence of the perovskite performance on the substrate surface roughness has been revealed by Snaith's group.[87] The perovskite layer showed more homogeneous and continuous on FTO/PEDOT:PSS substrates compared to the morphology of ITO/PEDOT:PSS, benefitting from the rough surface of FTO (100 nm) relative to ITO (~5 nm). This resulted in the superior performance of the device constructed on FTO which motivated us to explore our additive's influence in this favored system. Very impressively, an increased PCE with similar enhancement factor (~31%) to that of the ITO case was achieved on FTO, suggesting that DIO's beneficial influence on crystal growth is not limited by the interfacial structure. The device derived from the 1% DIO solution on FTO possessed a promising PCE of 11.8% with a V_{oc} of 0.92 V, a J_{sc} of 17.5 mA/cm^2, and a FF of 73.2%, enhanced from the 9.0% PCE of the control device with a V_{oc} of 0.90 V, a J_{sc} of 16.0 mA/cm^2, and a FF of 62.3%. Similar to the case of ITO substrates, the improved quality and surface coverage of the crystalline perovskite thin films caused by the presence of DIO significantly contributes to the enhancement of J_{sc} (16.0 to 17.5 mA/cm^2) and FF (62.3% to

73.2%). The results of our top-performing devices are among the best reported for state-of-the-art low-temperature solution processed photovoltaics at that time. The EQE plotted in **Figure 4.2b** confirms the increased J_{sc} of these devices. As can be seen, the maximum EQE peaks of the top-performing devices can reach over 70 % (ITO-substrate) and 80 % (FTO-substrate) EQE. This high photon-to-electron conversion highlights the perovskite extremely low exciton binding energy and superior charge transporting properties.

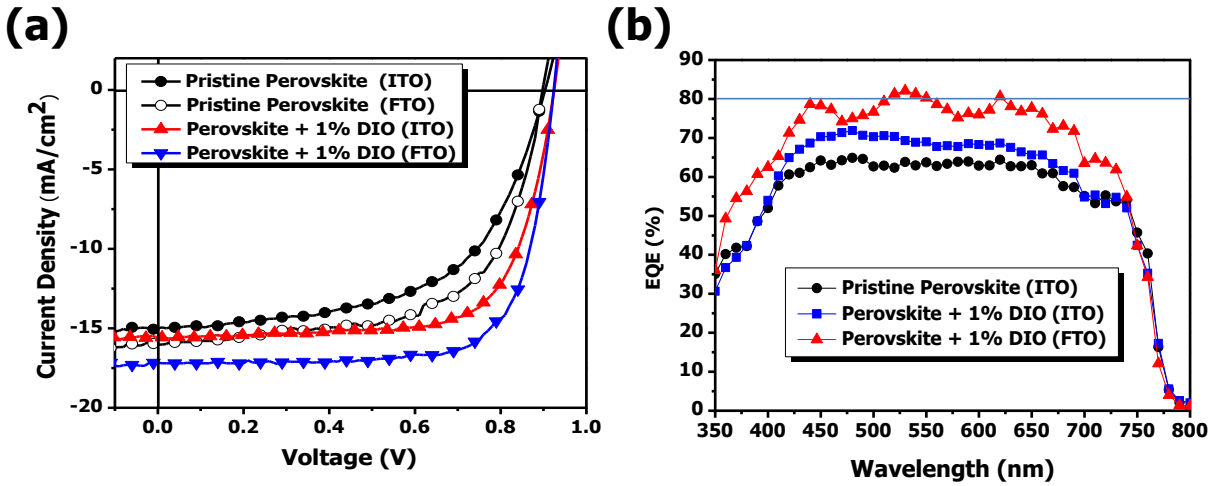

Figure 4.2. Influence of additives on device performance of the solution processed perovskite: (a) Current−voltage characteristics and (b) external quantum efficiency (EQE) spectra of the studied solar cells.

Table 4.1. Performance of the studied solar cells under AM 1.5G Illumination (100 mW cm^{-2}).

	V_{oc} (V)	FF (%)	J_{sc} (mA/cm^2)	PCE (%)
	On ITO Substrate (Roughness: ~5 nm; 15 ohm/sq)			
Pristine Perovskite	0.90	58.1	15.0	7.9
Perovskite-1% DIO	0.92	71.3	15.6	10.3
	On FTO Substrate (Roughness: ~100 nm; 8 ohm/sq)			
Pristine Perovskite	0.90	62.3	16.0	9.0
Perovskite-1% DIO	0.92	73.2	17.5	11.8

4.3.2 *Crystallinity Effects*

The relationship between the perovskite crystallinity and additive remain unclear. Although from the **Figure 4.3b**, the X-ray diffraction (XRD) spectra, the peak intensity of perovskite with additive shows almost two times than the peak intensity of perovskite without additive, we cannot identify the high intensity value is contributed from the high perovskite crystallinity or the volume of the perovskite material. Even the perovskite active layer thickness is the same, the amount of the perovskite with additive could be still more than the volume of the perovskite without additive since it has a better coverage, which might be the reason to increase the UV-absorption as demonstrated in **Figure 4.3a**. Utilization of the advanced analyze techniques, like Transmission electron microscopy (TEM), might help to see the effect of the additive on the perovskite crystal orientation.

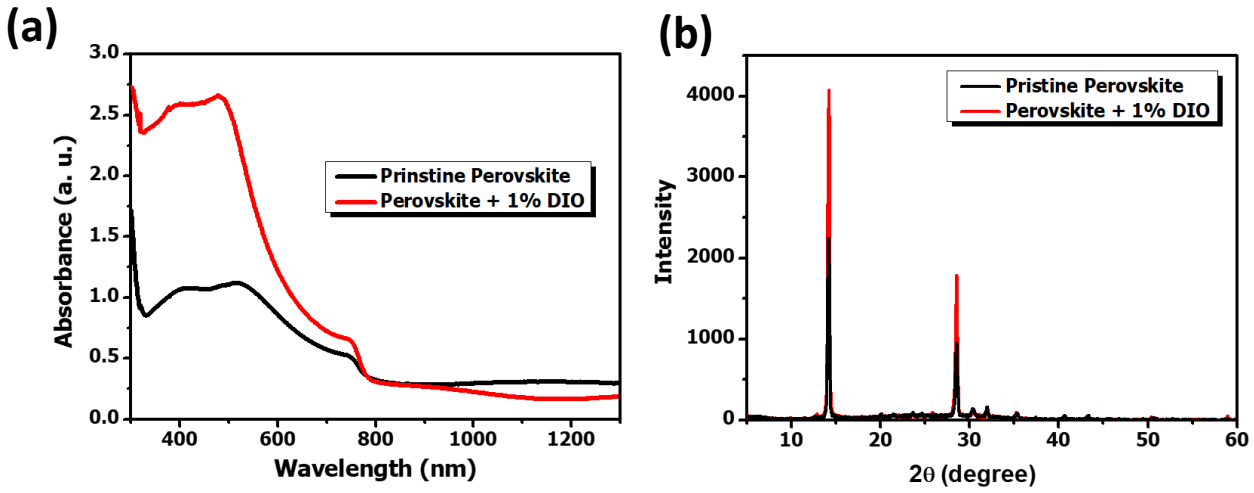

Figure 4.3. Influence of additives on light harvesting, and crystallization of the solution processed perovskite: (a) UV-vis absorption spectra and (b) XRD spectra of the solution processed perovskite with and without additive.

4.3.3 *Perovskite Formation Pathways*

To get more in-depth understanding of the function of DIO during perovskite crystallization, time resolved morphological characterization was made and recorded with scanning electron microscopy (SEM), as presented in **Figure 4.4**. The preparation of these perovskite thin films was identical to the conditions used for the device fabrication. As-cast, both films contain many pinholes and voids, but the additive assisted film already demonstrates markedly improved surface coverage. Additionally, the unique contrast features in the SEM image of the as cast DIO film along with its dense XRD pattern suggest a generation of order before annealing that is unique to the DIO sample. The presence of DIO may also modify this interfacial energy, making it more favorable for the crystal to grow in contact with the surface.

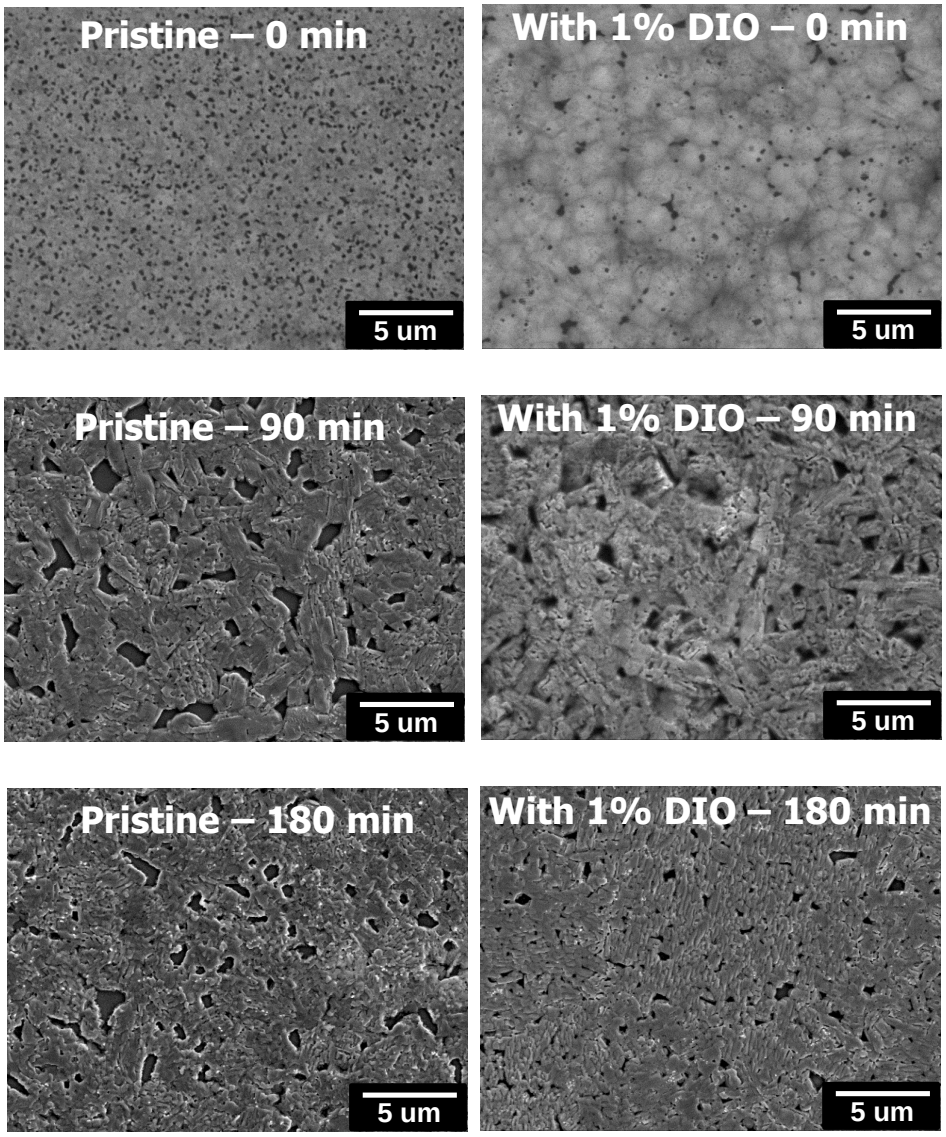

Figure 4.4. Time resolved morphology and crystallization of the solution processed perovskite: Time resolved SEM images of the surface of the evolving $CH_3NH_3PbI_{3-x}Cl_x$ films. The scale bars are all 5μm.

These improvements may also be attributed to the increased solubility of $PbCl_2$ in the mixed solvent DMF/DIO, as shown in **Figure 4.5**. We speculate that this improvement results from the temporary coplanar chelation of Pb^{2+} with DIO as Cl^- ligands reside in axial octahedral positions on Pb^{2+}.[24,76] Iodocarbons, soft Lewis bases, can coordinate with soft metal ions based on the hard-

soft acid-base principle.[105] Thus it can be envisioned that the transient metal-solvent coordination can improve the solubility of $PbCl_2$, as proposed in **Figure 4.6**.[105,106]

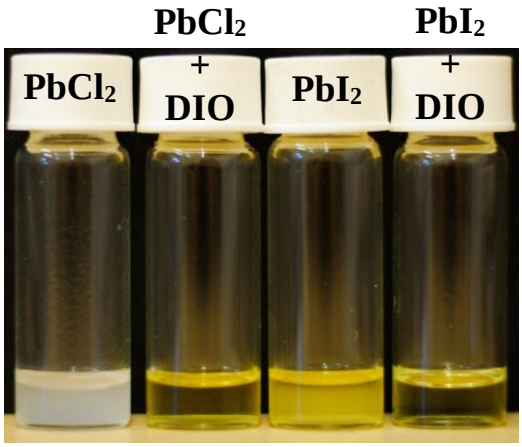

Figure 4.5. Solubility of the $PbCl_2$ and PbI_2 in DMF with or without additives. From left to right, $PbCl_2$ in DMF, $PbCl_2$ in DMF/DIO, PbI_2 in DMF, and PbI_2 in DMF/DIO.

On the other hand, bidentate chelation is also more favorable than monodentate chelation from a thermodynamic perspective as observed in some metal complex systems.[105,106] The formation of the chelate ring structures of the former allows less configurational entropy loss during coordination, resulting in a much smaller Gibbs free energy. Therefore, the temporary chelation of Pb^{2+} with DIO will participate in the evolving dynamic equilibrium of the drying and annealing film, co-existing with the coordination of Pb^{2+} with MAI during crystal growth until DIO fully evaporates. As a result, perovskite transformation path is altered, leading to a homogeneous perovskite thin film. Moreover, it can be seen in the micrographs that the crystallites of the additive-assisted film display more regular faceting and improved interconnectivity during crystal growth, which can also be attributed to the prolonged growth pathway caused by temporary chelation of Pb^{2+} by DIO. The distorted crystal lattice induced by captured DIO will increase the internal energy and configurational entropy of growing crystals thus modulating their growth rate

and shape. The impact of these modifications on growth path is clearly apparent in the device data discussed above, correlating well with the increase of all relevant parameters.

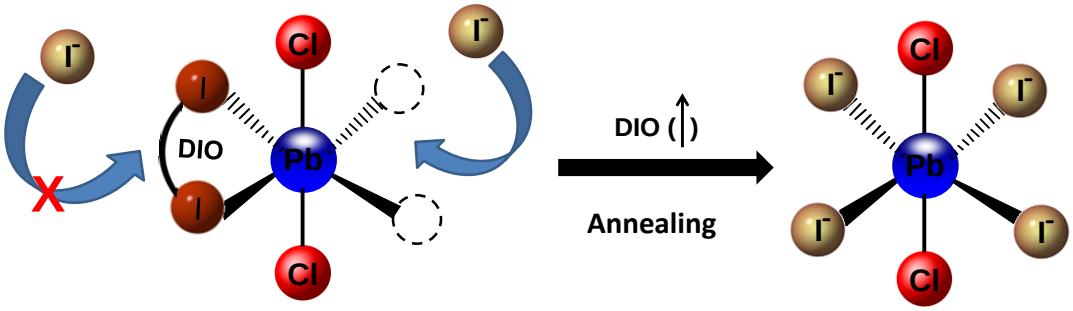

Figure 4.6. Proposed schematic diagram for the transient chelation of Pb^{2+} with DIO.

4.3.4 *Charge Transfer Efficiency*

Time resolved photoluminescence (PL) behavior was characterized to probe the influence of the enhanced crystallization of perovskite thin films on charge transfer efficiency. The detailed information regarding the preparation, measurement, and fitting methodology can be found in the experimental section. The PL lifetime of the samples was fitted with a bi-exponential decay function containing a fast decay and a slow decay process. We consider the fast decay process to be the result of the quenching of free carriers in the perovskite domain through transport to PEDOT:PSS or PCBM, and the slow decay process to be the result of radiative decay. **Figure 4.7** displays the PL decay and the related parameters are summarized in **Table 4.2**. For the pristine thin-film perovskite, the fast decay lifetime is 12.9 ± 0.8 ns and the slow decay lifetime is 104 ± 3 ns while their weight fractions are 81% and 19% respectively, indicating that charge transfer is the dominating decay mechanism. To mimic the real charge behavior in our p-i-n planar heterojunction device, the bilayer $MAPbI_{3-x}Cl_x$/PCBM systems were examined. The existence of the electron quenching PCBM layer atop the perovskite significantly decreases the fast decay

lifetime from 12.9 ± 0.8 ns to 3.4 ± 0.4 ns and increases the weight fraction of fast decay from 81% to 94%. This suggests that most of the free carriers generated by illumination are efficiently transferred to PEDOT:PSS and PCBM, which confirms the potential of the conventional p-i-n heterojunction.

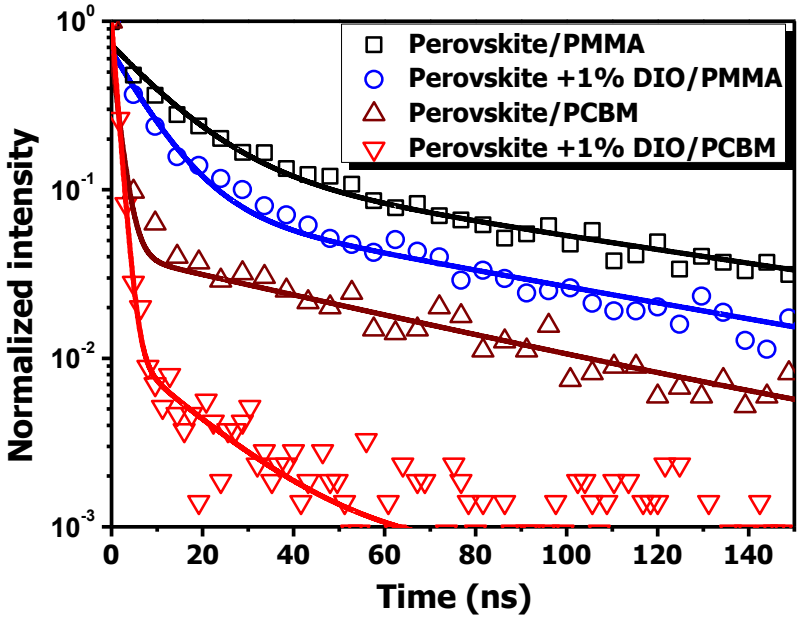

Figure 4.7. Advantages of the additive on the charge dissociation: Time resolved photoluminescence characterization of the solution processed perovskite with and without the additive.

Table 4.2. Time resolved photoluminescence characterization of the solution processed perovskite.

Subs.	ETM	Additive	τ_1 (ns)	Fraction 1	τ_2 (ns)	Fraction 2	Average (ns)
ITO/ PEDOT :PSS	-	-	12.9 ± 0.8	81%	104 ± 3	19%	30
		DIO	8.5 ± 0.5	88%	88 ± 3	12%	18
	PCBM	-	3.4 ± 0.4	94%	139 ± 10	6%	12

	DIO	1.2 ± 0.1	99%	18 ± 2	1%	1.4

As for the additive assisted perovskite thin film, the fast decay lifetime decreased from 12.9 ± 0.8 ns to 8.5 ± 0.5 ns and the weight fraction increased from 81% to 88%. The same trend was observed in the bilayer $MAI_{3-x}Cl_x$/PCBM film with lifetime decreasing from 3.4 ± 0.4 ns to 1.2 ± 0.1 ns and weight fraction increasing from 94% to 99%. As evidenced in **Figure 4.4**, the addition of DIO improved the coverage and crystallinity of the perovskite thin films on ITO/PEDOT:PSS, thus facilitating the diffusion of free carriers and increasing the efficiency of charge transfer. Consequently, the weight fraction of fast decay, which relates to the charge transfer process increased and the lifetime of fast decay decreased. For perovskite processed from the 1% DIO precursor with PCBM, the weight fraction related to quenching was almost 100%, which indicated a very efficient charge dissociation in the perovskite domain with PEDOT:PSS and PCBM. The observed high J_{sc} (15.6 ~ 17.5 mA/cm^2) and FF (71.3 ~ 73.2 %) of the devices derived from the 1% DIO solution can also be attributed to this enhanced charge separation and collection.

4.4 SUMMARY

In summary, a significant improvement of the planar-heterojunction PVSCs from 9.0% up to 11.8% PCE by incorporating DIO additives into the perovskite precursor solutions, resulting in raising the perovskite film quality. From the SEM and XRD characterizations, the additives facilitate perovskite homogeneous nucleation and modulate the growth path during crystallization, resulting in efficient charge transfer between the charge transporting interlayers and the perovskite absorber. As a result, a promising low-temperate solution process method to fabricate efficient planar-heterojunction PVSCs was demonstrated. This additive assisted crystallization study

highlights a new potential way allowing scientists to manipulate the perovskite crystal and morphology, which is critical to realize highly efficient PVSCs.

Chapter 5. INTERFACIAL ENGINEERING: ROLE OF FULLERENE DERIVATIVES IN PEROVSKITE PHOTOVOLTAICS

5.1 INTRODUCTION

PHJ PVSCs have been intensely studied recently since it has potential to apply in the flexible photovoltaics. Generally, it consisted with HTMs and ETMs, while perovskite active materials are sandwiched between them. Many HTMs materials, such as PEDOT:PSS, NiOx, CuSCN, etc, have been developed to employ in PHJ PVSCs. For PHJ PVSCs ETMs, however, the most common materials are fullerene derivatives due to its decent electron mobility, appropriate energy level, solution processability at a relatively low-temperature. Guo *et al.* first demonstrated the feasibility of such an inverted PHJ configuration, realizing a PCE of 3.9% by employing a PCBM ETM.[64] Since then, fullerene based materials have been widely employed in different kinds of PHJ PVSCs as ETMs.

In addition to PCBM, other fullerene derivatives, such as C_{60}, ICBA, $PC_{71}BM$, etc, have also been utilized as efficient ETMs in PVSCs. A PHJ PVSC with a high FF over 0.80 was reported by utilizing unique fullerene bilayers consisting of PCBM/C_{60} or ICBA/C_{60}. Besides, a PCE of 16.3% PHJ PVSC with $PC_{71}BM$ as ETMs were demonstrated by Wu's group.[107] All these results highlight the importance of fullerene-based ETMs in enhancing device performance. However, large discrepancies documented in the literature for each system suggest that a systematic study to investigate the influence of the fullerene physical properties on device performance is warranted. In addition, the interaction between perovskite and fullerene remains unclear at present.[89] For this reason, it is important to understand the roles of these fullerene-based ETMs in PVSCs, especially in terms of their intrinsic properties and interaction at the perovskite/fullerene interface.

In this chapter, we demonstrate a clear correlation between the charge extraction properties of fullerene-based ETMs and photovoltaic performance by systematically studying three fullerenes, ICBA, PCBM, and C_{60} (**Figure 5.1**). The conversion efficiency of fullerene-derived PVSCs (8.06% for ICBA, 13.37% for PCBM, and 15.44% for C_{60}) improves with increasing electron extraction rate of the fullerene layer, which is derived from steady-state PL measurement. This result might stem from the better energy alignment between the perovskite (CB: -3.9 eV) and fullerene derivatives ($LUMO_{ICBA}$: -3.6 eV, $LUMO_{PCBM}$: -3.6 eV, and $LUMO_{C60}$: -3.6 eV). In addition to elucidating the impacts of fullerene derivative's energy level matching, we have also examined the electrical characteristics of bilayer perovskite/fullerene FETs. Surprisingly, a metallic behavior was observed in the bilayer perovskite/fullerene film. This finding implies that a strong charge redistribution occurs at the interface of perovskite and fullerene derivatives. As a result, the recombination dynamic and the band structure at the perovskite interface might be changed when fullerene derivatives are applied as ETMs for PVSCs.

5.2 EXPERIMENTAL

Fabrication of perovskite thin-film solar cells

ITO-coated glass substrates were cleaned with a detergent, DI-water, acetone, and isopropanol sequentially. After drying, the ITO substrate was treated with air plasma for 20 s. PEDOT:PSS (Baytron 4083) was then spin-cast onto clean ITO substrates, followed by annealing at 150 °C for 10 min in air. To prepare the perovskite precursor solution (concentration is about 1M), PbI_2 and MAI were dissolved in a mixture of r-butyrolactone and DMSO (7:3 v/v) with a molar ratio of 1:1 and stirred at 80 °C for 12 h. To avoid moisture, the perovskite thin films were prepared in an N_2-filled glovebox *via* a consecutive three-step spin-coating process at 0.5k, 1k, and 5k rpm for 5, 45, and 45 s, respectively. During the spin-coating, the substrate was treated with toluene at 20 s after

the start of 5k rpm. Then, the devices were annealed at 100 °C for 15 min in the glovebox. Afterward, the ICBA/PCBM/C_{60} solution (15 mg/ml in dichlorobenzene) and Bis-C_{60} surfactant (2 mg/ml in isopropyl alcohol) were sequentially spin-cast at 1000 rpm for 60 s and 3000 rpm for 30 s, respectively. Finally, a 150 nm thick top Ag electrode was evaporated under high vacuum (< 2×10^{-6} Torr). For all devices, the active area was defined as 3.14 mm^2 by shadow mask. All the *J-V* curves in this study were recorded by using Keithley 2400 source measurement unit and the scan rate was kept at 0.1-1.0 V/s, except for the hysteresis test 0.01V/s. The photocurrent was measured under illumination from a 450 W thermal Oriel solar simulator (AM 1.5G). The illumination intensity of the light source was accurately calibrated employing a standard Si photodiode detector equipped with a KG-5 filter, which can be traced back to the standard cell of National Renewable Energy Laboratory (NREL). The EQE spectra performed here are obtained by the IPCE measurement using the combination of a Xenon lamp (Oriel, 450 W) as the light source, a monochromator, chopper with frequency of 100 Hz, a lock-in amplifier (SR830, Stanford Research Corp), and a Si-based diode (J115711-1-Si detector) for calibration.

Fabrication and Characterization of FETs

Fullerene-based FETs were fabricated with the top-contact and bottom-gate geometry. Heavily doped p-type silicon <100> substrates with a 300 nm thermal oxide layer were purchased from the Montco Silicon Technologies INC. Substrates were cleaned by sequential ultrasonication in acetone and isopropyl alcohol for 15 min each, then treated with UV-ozone for 5 min. For fullerenes-based FET devices, a thin divinyltetramethyldisiloxanebis(benzocyclobutene) (BCB) buffer layer was primarily spin-cast at 4000 rpm on silicon dioxide, followed by annealed at 250 °C overnight. The total capacitance density measured from parallel-plate capacitors was 10.6 nF/cm^2. For bilayer FET devices, the perovskite layer and fullerene layer were sequentially spin-

cast on silicon dioxide by the same procedure used in solar cell fabrication. The thickness of the fullerene layers is around 60 nm estimated from SEM measurement. Inter-digitated source and drain electrodes (W=1000 μm, L= 50 μm) were defined by thermal evaporated Ag (100 nm) through a shadow mask under high vacuum (< 2×10^{-6} Torr). OFET characterization was carried out in an N_2–filled glovebox using an Agilent 4155B semiconductor parameter S6 analyzer. The field-effect mobility was calculated from the linear fit of $(I_{ds})^{1/2}$ vs V_{gs} in the saturation regime. The threshold voltage (V_{th}) was estimated as the x intercept of the linear section of the plot of $(I_{ds})^{1/2}$ vs V_{gs}. Conductivity was derived from gated two terminal measurements at zero gate voltage with the equation of $\sigma = (L/A)(I_{ds}/V_{ds})$, where L (cm) and A($cm^2$) are the channel length and cross-sectional area of the devices, respectively.

5.3 Result and Discussion

5.3.1 *Fullerene Derivatives Selections*

Three fullerene derivatives (ICBA, PCBM, and C_{60}) were chosen to systematically understand the role of fullerene-based ETMs in PVSCs. The structures of the fullerene derivatives were shown in **Figure 5.1**. Generally, fullerenes are served as electron extraction layers, which help the free electron generated in a perovskite absorber collected by the cathodes. In the other word, a good electron extraction rate of the fullerene layer could influence the device performance dramatically. Considering the electron extraction rate is closely correlated with the energy level of both the perovskite and fullerene derivatives, we carefully chose three fullerene derivatives (ICBA, PCBM, and C_{60}) with different LUMO level. Besides, since fullerene composition is the only dynamic variable in our system, the differences in charge extraction rate between devices should be directly correlated with the fullerene interlayer's electrical characteristics of the perovskite/fullerene

interface.

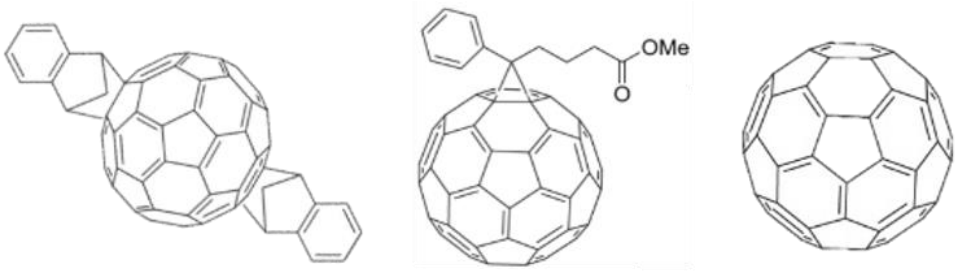

ICBA **PCBM** **C_{60}**

Figure 5.1. The chemical structures of the n-type fullerene derivatives, ICBA, PCBM, and C_{60}.

5.3.2 *The Relation of Fullerene Intrinsic Properties and PVSCs*

The energy levels of the fullerenes in this study were determined by cyclic voltammetry (CV). The detail energy level of each fullerene derivatives was shown in **Table 5.1**. LUMO level ($LUMO_{ICBA}$: -3.6 eV; $LUMO_{PCBM}$:-3.8 eV; $LUMO_{C60}$:-3.9 eV) gradually decreases from ICBA to C_{60} due to increased conjugated atoms in the fullerene cage. The UV-vis absorption spectra of all fullerenes show weak absorption beyond 400 nm, which prevents parasitic absorption loss. The electron mobility of these fullerenes was characterized with bottom-gate/top-contact configuration FET devices.[89] Curves shown in **Figure 5.2a-b** are the transfer and output curves of the fullerene films, all of which clearly manifest their n-type semiconducting properties. Estimated electron mobilities are summarized in **Table 5.1** along with the associated energy levels. Due to increased conjugation, electron mobility gradually increases from ICBA (6.9×10^{-3} cm^2/Vs), to PCBM (6.1×10^{-2} cm^2/Vs), to C_{60} (1.6 cm^2/Vs). C_{60} mobility is highest among the three may due to the lack of bulky side-chains, which allows it to be packed more densely and thus enhances electron mobility. Worth to notice, the exact value for the C_{60} mobility might not as same as what we showed on **Table 5.1** since the C_{60} curve is not a simple FET transfer characteristic, which caused the error when we do the mobility estimation.

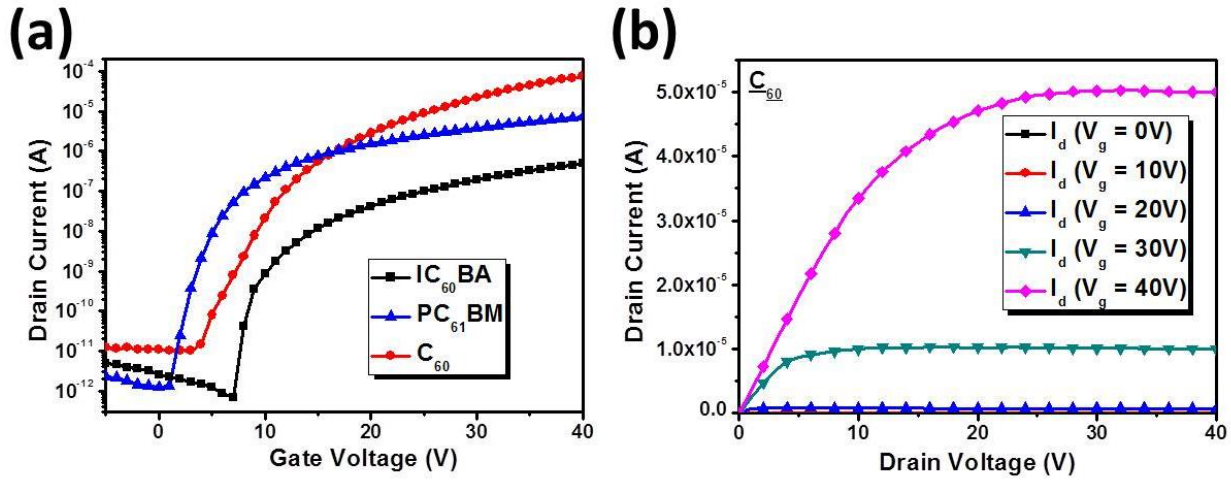

Figure 5.2. The FET (a) transfer characteristics of studied fullerenes and (b) output characteristics of C_{60}.

Table 5.1. The energy levels and FET electron mobilities of the studied.

	LUMO (eV)	HOMO (eV)	E_g (eV)	Mobility (cm^2/Vs)	On/Off Ratio
ICBA	-3.6	-5.6	2.0	6.9×10^{-3}	7.0×10^5
PCBM	-3.8	-5.9	2.1	6.1×10^{-2}	5.7×10^6
C_{60}	-3.9	-5.6	1.7	1.6	7.4×10^6

To illustrate the effects of electron extraction capability of fullerene-based ETMs on the photovoltaic performance of PVSCs, an inverted device configuration of ITO/PEDOT:PSS (35-40 nm)/$MAPbI_3$ (300 nm)/fullerenes (~60 nm)/Bis-C_{60} (10 nm)/Ag (150 nm) was fabricated.[70,99,108,109] All the fullerene ETMs are spin-cast for a fair comparison. The deposition of the $MAPbI_3$ thin film followed the solvent-washing method reported by Seok *et al.*, which provides a smooth perovskite thin film with good surface coverage on PEDOT:PSS.[2] The detailed information regarding perovskite deposition and device fabrication is described in the experimental section.

The *J-V* curves of the studied devices under 1 sun AM 1.5 simulated solar irradiation are

shown in **Figure 5.3a** and the relevant photovoltaic parameters including V_{oc}, J_{sc}, FF, and PCE are summarized in **Table 5.2**. Impressively, the C_{60}-based device afforded the highest PCE of 15.44% with a V_{oc} of 0.92 V, a J_{sc} of 21.07 mA/cm^2, and an FF of 0.80. The PCBM- and ICBA-based devices showed PCEs of 13.37% (V_{oc}: 0.89 V, J_{sc}: 18.85 mA/cm^2, and *FF*: 0.80) and 8.06% (V_{oc}: 0.95 V, J_{sc}: 11.27 mA/cm^2, and *FF*: 0.75), respectively.

Compared to the ICBA-derived device, the PCBM- and C_{60}-based devices exhibited much higher J_{sc} and FF. The high J_{sc}s of both devices can be verified by their EQE curves shown in **Figure 5.3b**, in which the error between the integrated J_{sc}s and the measured values are both within 5%. The insert in **Figure 5.3b** is the UV-vis absorption of $MAPbI_3$, $MAPbI_3$/PCBM, and $MAPbI_3/C_{60}$. As can be seen, the perovskite absorber is responsible for most of the light harvesting while light absorption from the fullerene is negligible. High panchromatic photon responses over the visible range were observed in the EQE curves, consistent with the broad absorption of perovskite.

Anomalous hysteresis has recently been raised as an important issue for PVSCs.[110] As such, a hysteresis test of the studied devices was performed. All the devices presented very minor hysteresis at a low scan rate of 0.01 V/s, suggesting limited charge traps at the perovskite interfaces (PEDOT:PSS/$MAPbI_3$ and $MAPbI_3$/fullerene). These results are consistent with the general observation of reduced hysteresis in inverted fullerene-based PHJ PVSCs as compared to inverted TiO_2-based PHJ PVSCs.[88,89]

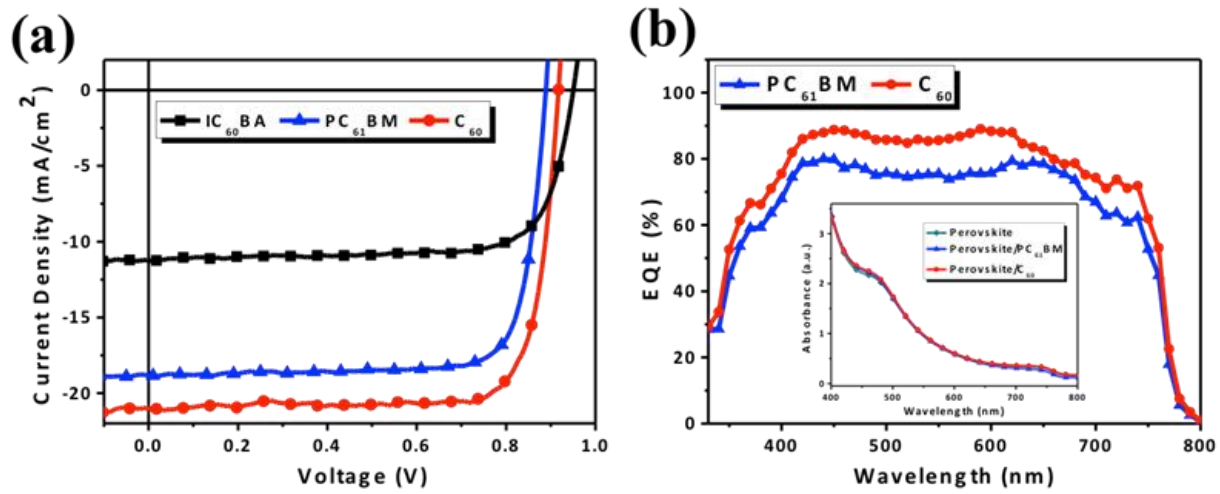

Figure 5.3. (a) *J-V* characteristics and (b) external quantum efficiency (EQE) spectra of the studied PVSCs using different fullerene-based ETMs.

Table 5.2. Photovoltaic performance of the studied PVSCs using different fullerene-based ETMs.

Employed Fullerene	V_{OC} (V)	J_{SC} (mA/cm^2)	FF	PCE (%)	R_s (Ω cm^2)	R_{sh} (kΩ cm^2)
ICBA	0.95	11.27	0.75	8.06	5.10	0.71
PCBM	0.89	18.85	0.80	13.37	2.60	3.14
C_{60}	0.92	21.07	0.80	15.44	2.26	8.72

The improved J_{sc} and FF of PCBM- and C_{60}-based PVSCs can be interpreted as a consequence of improved charge dissociation/transport at the perovskite/fullerene interface arising from these fullerenes' decent electron extraction capability. The assumption is supported by the steady-state PL spectra, as shown in **Figure 5.4**. Quenching efficiency of perovskite luminescence follows the trend C_{60} > PCBM >> ICBA. The improved quenching provided by C_{60} and PCBM result in much reduced series resistance (R_s) and increased shunt resistance (R_{sh}) of derived PVSCs, leading to better performance as compared to the ICBA-based device. More importantly, it shows that C_{60} is an even better ETM than the typically used PCBM for high-performance inverted PVSCs. C_{60} is also more cost-effective than PCBM. Given its comparable room-temperature solution

processability, it is economically superior as well.

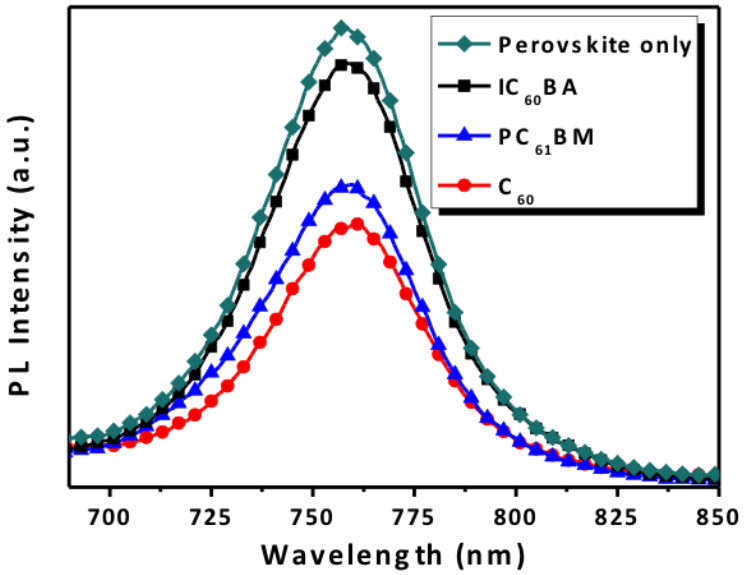

Figure 5.4. Steady-state PL spectra of perovskite in the presence of the studied fullerene quenchers.

5.3.3 *Interfacial Interaction between Fullerene and Perovskite*

Complicated surface states stemmed from unsaturated Pb^{2+} and I^- ions at the surface or boundary are identified in perovskite active layer. These under-coordinated ions can act as electronic trap states and obstruct charge transfer across perovskite interfaces.[111,112] Passivation of the perovskite surface with either a Lewis base or acid has been demonstrated to effectively reduce non-radiative recombination, thereby leading to enhanced photoluminescence lifetimes by nearly an order of magnitude. Similar perovskite passivation was also observed at the perovskite/fullerene heterojunction, in which fullerene was found to passivate the perovskite surface to result in a much diminished trap density of states (*t*DOS).[89] These results highlight the complexity of perovskite interfaces.

Motivated by this perspective, we attempt to probe the electrical characteristics of the

perovskite/fullerene interface. Similar to the perovskite/fullerene heterojunction used in the PVSCs in the study, bilayer perovskite/fullerene FETs were fabricated in which $MAPbI_3$ and fullerenes were sequentially deposited on silicon oxide substrates. Surprisingly, all bilayer perovskite/fullerene devices exhibit metallic behavior, as depicted in **Figure 5.5a**. The linear output characteristics shown in **Figure 5.5b-d** further affirm the metallic-like conduction of the bilayer perovskite/fullerene film, which is strikingly different from the pristine n-type semiconducting properties observed in the fullerene-based FETs as discussed earlier.

Taking C_{60} for example, the perovskite/C_{60} FET shows a six order higher current than the pristine C_{60} FET at $V_G = 0$ V (**Figure 5.2a** & **5.5a)** while the ICBA- and PCBM-based devices also exhibit similar phenomena but with lower degrees of enhancement. The estimated intrinsic conductivities (at $V_G = 0$ V) for the bilayer $MAPbI_3$/fullerene devices are 2.4×10^{-3} S/cm (for $MAPbI_3/C_{60}$), 3.2×10^{-4} S/cm ($MAPbI_3$/PCBM), and 6.5×10^{-5} S/cm ($MAPbI_3$/ICBA), respectively. These results suggest that charge transfer occurs spontaneously between perovskite and fullerenes.

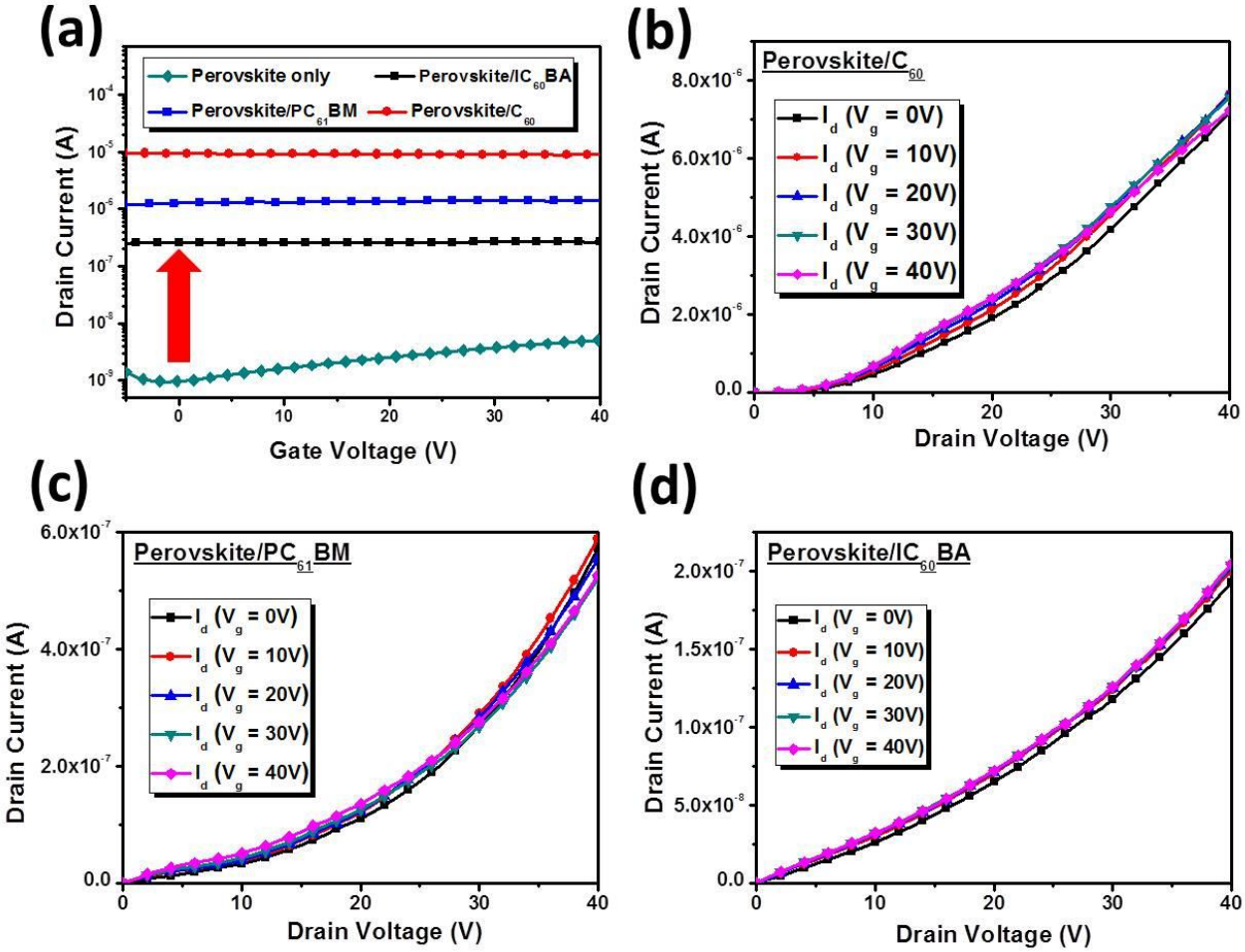

Figure 5.5. The FET (a) transfer characteristics of bilayer perovskite/fullerenes devices and the output characteristics of (b) perovskite/C_{60}, (c) perovskite/PCBM, and (d) perovskite/ICBA FET devices.

Table 5.3. The electrical characteristics of the bilayer perovskite/fullerene FET devices.

	Conductivity (S/cm)
$MAPbI_3$/ICBA	6.5×10^{-5}
$MAPbI_3$/PCBM	3.2×10^{-4}
$MAPbI_3/C_{60}$	2.4×10^{-3}

At the device level, this change in charge distribution may have multiple consequences. First, defect trap states at the perovskite interface can be passivated. As a result, perovskite

photoluminescence lifetime would increase due to diminished non-radiative recombination, as has been demonstrated by Snaith *et al*.[111,112] both in the case of electron-rich and electron-deficient molecular passivation. Unfortunately, this effect is difficult to analyze in our system since the fullerenes are excellent quenchers. However, the recent finding reported by Huang *et al.* echoes this hypothesis to a certain extent as they find that fullerene-based ETMs (PCBM, C_{60}, or PCBM/C_{60}) do passivate the trap density of states at the perovskite surface.[89,113] Second, charge redistribution can increase the carrier concentration in the fullerene layer, which effectively becomes n-doped by the electrons transferred from the perovskite. Upon doping, the Fermi level of the fullerene film would up-shift to conducting states, thereby reducing contact resistance, enhancing charge extraction, and increasing built-in potential across the device. Both these phenomena occurring at the perovskite/fullerene interface can effectively reduce the interfacial energy barrier for charge extraction, and thus they are believed to be the dominant factors leading to the very minor hysteresis and high performance of fullerene-based PVSCs.[70,89,92]

To more thoroughly understand interaction at the perovskite/fullerene interface, bilayer samples analogous to those fabricated for FET measurement containing a C_{60} top layer of variable thickness were prepared for characterization with X-ray photoelectron spectroscopy (XPS). While XPS is an excellent technique for characterizing interfacial phenomena, its surface sensitivity (3 to 5 nm) requires a sample that contains an incredibly thin and uniform top layer to facilitate effective measurement of the interface itself. We approached the challenge by carefully spin-casting dilute solutions of C_{60} with gradually decreasing concentrations. Individual elements in the resulting systems (I, Pb, N, and C) were investigated, and the XPS spectra are shown in **Figure 5.6**, in which all the peaks of each element are normalized and shifted according to C signal.

The gradually changing intensity ratio between signals from 1s carbon core levels

corresponding to C-C (285.4 eV) and C-N (286.6 eV) bonding shown in **Figure 5.6d** demonstrates that although we do not see much change in the binding energy Pb and I, the C_{60} films employed may indeed vary through the thickness range necessary to begin to see the interface itself. With this in mind, the lack of change in Pb and I signal suggests that a specific chemical interaction is not necessary to facilitate charge redistribution across the perovskite/fullerene interface. This is to say that charge redistribution at the perovskite/C_{60} interface might result from the effective coupling between the CB of perovskite and the LUMO level of C_{60} rather than an oxidation or reduction of species at the interface. Although previous work indicates that charge transfer from an iodide moiety to the conjugated π-network of the fullerene cage is possible,[114,115] at this stage we are not prepared to point to the precise chemical and electronic interactions facilitating charge redistribution. That said, this analysis serves as a basis for a more comprehensive study of the issue in the future.

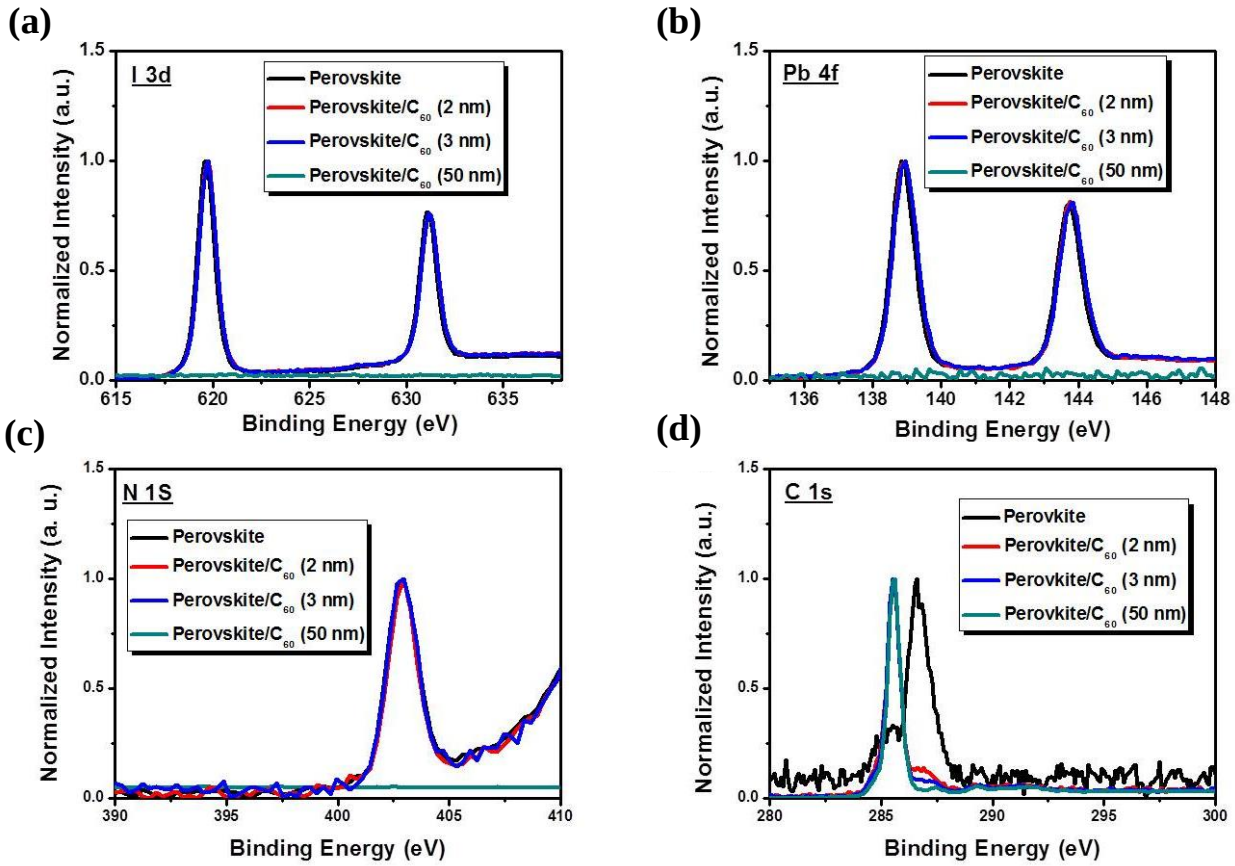

Figure 5.6. Thickness dependence of XPS spectra of (a) I 3d, (b) Pb 4f, (c) N 1s and (d) C 1s at perovskite/C_{60} interface.

5.4 SUMMARY

In this chapter, an important correlation between charge extraction capability of fullerene-based ETMs and resulting device performance in inverted PHJ PVSCs have demonstrated by systematically studying three fullerenes, ICBA, PCBM, and C_{60}. The PCEs of the fullerene-derived PVSCs (8.06% for ICBA, 13.37% for PCBM, and 15.44% for C_{60}) clearly follow the trend of PL quenching in the fullerene layer, which illustrates that fullerenes with high electron extraction capability can effectively promote PVSC performance. Besides elucidating the role of fullerene electron extraction capability, we have also unveiled the metallic-like conduction of bilayer perovskite/fullerene systems by FET measurements signifying that spontaneous charge

redistribution occurs across the perovskite/fullerene interface. These combined phenomena lead to the finding that C_{60} is an even better ETM than the typically used PCBM for high-performance inverted PVSCs. As a whole, this study also more comprehensively elucidated the complex roles of fullerenes in enhancing the performance of PVSCs, which ultimately pointed at the perovskite/fullerene interface as a system warranting further study.

Chapter 6. DEVICE ENGINEERING: GRADED FULLERENE HETEROJUNCTION IN LOW BANDGAP SN-BASED PEROVSKITE PHOTOVOLTAICS

6.1 INTRODUCTION

To ensure PVSCs become a more environmentally friendly technology, it is urged to develop metal alternatives to replace Pb, which is one critical element in perovskite composition. Scientists have been explored many metal alternatives to resolve this issue. Among all the candidates, Tin (Sn) is one of the most feasible metal since it has similar outer shell electronic configuration, coordination geometry and ionic radius as Pb ions.[116,117] However, Sn based PVSCs suffer from low device performance and stability due to oxidative susceptibility of Sn^{2+}.[108,118,119] The oxidation of Sn^{2+} to Sn^{4+} significantly deteriorates the semiconductor nature of perovskites and adversely affects the photovoltaic device operation. Recently, some additives, like SnF_2 and antioxidants, has been introduced to alleviate the impact of Sn oxidation and improve the processability of Sn-based perovskites.[120,121] Through optimization of additive composition and processing conditions, Yan's group have reported a certified PCE of 17.01% based on $(FASnI_3)_{0.6}(MAPbI_3)_{0.4}$ perovskite composition.[122]

To further improve the optoelectronic quality of this class of perovskites, it is important to reduce the density of trap states (tDOS), which adversely impacts the charge collection efficiency and device performance. Trap states usually stem from the facile point defect formation in the crystal and uncoordinated bonding at the surface.[123] Additionally, for Sn-based perovskites, Sn cation vacancies (V_{Sn}) are identified as a factor that could deteriorate perovskite semiconductor properties.[117,124] Recent studies on perovskite and fullerene interaction provide some insights for potentially overcoming these issues. First, the tDOS at the perovskite thin film could be passivated

by applying fullerene derivatives, like C_{60} or PCBM.[113,125] As a result, the PVSCs electronic properties were effectively enhanced and the hysteresis effects were significantly suppressed.[125] Second, the fullerene derivatives could be applied as an efficient ETM for PVSCs since it has decent charge transport properties and lower the resistance at perovskite/ETM interface.[126] These important insights could be translated to the development of efficient low-E_g binary Pb-Sn PVSCs.

The fluoroalkyl-substituted fullerene, DF-C_{60}, has been developed by Jen et. al. to passivate defects at perovskite grain boundary and also increase the hydrophobicity of perovskite surface.[127] It has been demonstrated as an efficient ETM to enhance the PVSCs device performance. Worth to notice, a graded fullerene distribution in perovskite thin-film surface during fullerene/perovskite heterojunction formation because of the low surface energy of fluoroalkyl function group. Similar graded fullerene distribution structure was also reported by other groups recently, and have been demonstrated as an effective method to enhance the charge extraction efficiency.[128] These results highlight the efficacy of forming graded heterojunction using fullerene derivatives to passivate the tDOS and improve device performance.

In this section, we incorporated fluoroalkyl-substituted fullerene, DF-C_{60}, into the Pb-Sn mixed perovskite to lower the tDOS of thin films and enhance the electron collection efficiency, leading to better device performances. To understand the effects of DF-C_{60} on Sn based perovskite, Urbach energies were carefully extracted from the EQE measurement. Also, capacitance-voltage profiling and impedance spectroscopy were conducted to investigate the origin of defects passivation. For a fair comparison, the composition of Pb-Sn mixed perovskites in this paper are fixed $MAPb_{0.5}Sn_{0.5}I_3$ since it has relatively small bandgap around 1.22 eV. Worth to notice, the fluorene function groups on the fullerene could prevent the moisture penetration and, hence, protect the perovskite materials in high moisture conditions.

6.2 EXPERIMENTAL

Solar cell fabrication and characterization

ITO glass substrates were cleaned via ultra-sonication in the sequential detergent, DI water, acetone, and isopropanol for 10 min immersion, respectively. After drying under an N_2 stream, substrates were further cleaned by UV-ozone treatment for 10 min. PEDOT:PSS (Baytron P VP Al 4083, filtered through a 0.45 μm nylon filter) was first spin-coated onto the substrates at 5k rpm for 30 s and annealed at 150°C for 10 min in air. To prepare the perovskite precursor solution, MAI, PbI_2, SnI_2 and SnF_2 (molar ratio of 1:1.2:1:0.2) were dissolved in γ-butyrolactone and DMSO with a volume ratio of 7:3 and with a total concentration of 1 M. For the perovskite thin films with PHJ structures, the perovskite precursor were spin-coated onto PEDOT:PSS at 5000 rpm for 30 s. After spin 10s, anti-solvent toluene was in-situ dripped on the substrate to quench perovskite crystal growth. For the perovskite thin films with BHJ structures, the DF-C_{60} solution was added into the perovskite precursor solution prior spin-coating as the previous report.[127] Same spin-coating conditions as PHJ devices fabrication were utilized to formed Sn-based perovskite thin films. For the perovskite thin films with GHJ structures, same perovskite precursor used in PHJ devices was applied on top of PEDOT:PSS and spin coating at 5000 rpm for 30 s. After 10 s, toluene contained 6mg/ml DF-C_{60} was dripped to formed the GHJ structure. After spin-coating, the films were annealed at 100 °C for 10 min. The PCBM ETM (15 mg/mL in chlorobenzene) was spin-coated onto the perovskite film at 1500 rpm for 60 s and bis-C60 interlayer (2 mg/mL in isopropyl alcohol) was spin-coated at 3000 rpm for 30 s. For the electrodes, silver was evaporated under high vacuum ($<2\times10^{-6}$ Torr) for 150 nm thickness. The device area was defined by the mask as 1.022 cm^2.

XRD measurement was conducted by X-ray diffractometer (Bruker D8 Discover). The perovskite morphology and structure were observed by FEI Sirion XL30. The device performance in this paper was measured by Keithley 2400 source measurement unit. The photocurrent was measured under illumination from a 450 W thermal Oriel solar simulator (AM 1.5G). The illumination intensity of the light source was accurately calibrated employing a standard Si photodiode detector equipped with a KG-5 filter, which can be traced back to the standard cell of National Renewable Energy Laboratory (NREL). The EQE spectra were measured by combining a monochromated 450 W xenon lamp (Oriel) with a source meter (Keithley 2400) and calculated using a calibrated Si photodiode (OSI-Optoelectronics). The steady-state photoluminescence spectra were measured by Horiba Fluorolog FL-3 with an excitation wavelength of 550 nm. EIS spectra were measured at an applied bias and a frequency ranging between 1 Hz and 1 MHz with AC amplitude of 10 mA. The Z-View Analyst software was used to model the Nyquist plots obtained from the impedance measurements.

6.3 Result and Discussion

6.3.1 *Two methods to realized GHJ* Structure

In order to have a comparative control, we optimized the additive formulation for $MAPb_{0.5}Sn_{0.5}I_3$ based devices. We utilized tin fluoride (SnF_2) additives to suppress the oxidation of Sn^{2+} and reduce the hole density in the resulting Sn-based perovskite films. In the meantime, we also added the same mole ratio of excess lead iodide (PbI_2) additives to avoid the bandgap change. From the UV-vis absorption, the bandgap of the perovskite thin film with different additive ratio remains around 1.22 eV. Besides, several studies have demonstrated that slightly excess PbI_2 results in beneficial defect passivation and improve the perovskite film quality.[129–131] This is reflected in the device performance. With increased amount of additive ratio, the device performance increases

correspondingly. The optimized condition is found to be Pb/Sn perovskite with 10% molar ratio additives. The corresponding device has a V_{oc} of 0.69V, J_{sc} of 24.23 mA/cm^2, *FF* of 0.68 and PCE of 11.39%. This optimized perovskite condition was used as a control device in this paper.

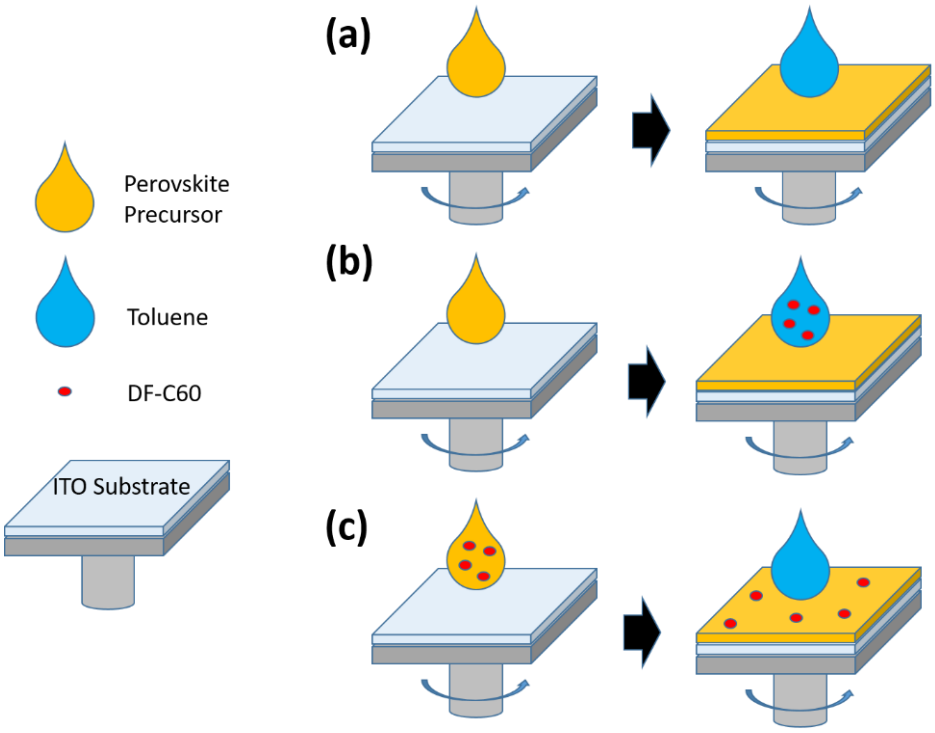

Figure 6.1. The fabrication processes and SEM images of the perovskite thin films with (a) PHJ, (b) GHJ and (c) BHJ structures.

To explore and better understand incorporation of DF-C_{60}, two methods were investigated to fabricate fullerene/perovskite heterojunction devices. First, we mixed DF-C_{60} solution with $MAPb_{0.5}Sn_{0.5}I_3$ precursor before the toluene washing treatment, as described in the **Figure 6.1c**. Several groups have reported similar techniques.[127,132–134] From our previous work, the DF-C_{60} and $MAPbI_3$ mixture slightly increases the perovskite grain size.[127] Moreover, the DF-C_{60} would be distributed at the surface region of $MAPbI_3$ thin film due to the low surface energy of fluorene function groups. This unique distribution enhanced the device performance and suppressed the hysteresis in devices. From the SEM images showed in **Figure 6.2a** and **c**, the morphology of the

$MAPb_{0.5}Sn_{0.5}I_3$ with and without DF-C_{60} is similar. However, from the device point of view, the performance decreased dramatically when using fullerene perovskite mixture. This result might arise from the difference of crystallization kinetic between $MAPbI_3$ and $MAPb_{0.5}Sn_{0.5}I_3$ perovskite. It well documented that the transformation time from Sn-based perovskite precursor to perovskite film is much rapid than the time of pure Pb perovskite. This constraint DF-C_{60} movability, implying limited time moving toward the surface or grain boundary. Therefore, DF-C_{60} would be trapped inside the perovskite grains during the perovskite crystallization and form bulk heterojunction (BHJ) structure. Compared to the planar heterojunction (PHJ) structure, the trapped DF-C_{60} inside perovskite grains acts as a recombination site instead of passivation site. Moreover, the uncontrollable distribution of fullerenes close to HTM side would hinder the hole collection efficiency, leading to poor device performances.

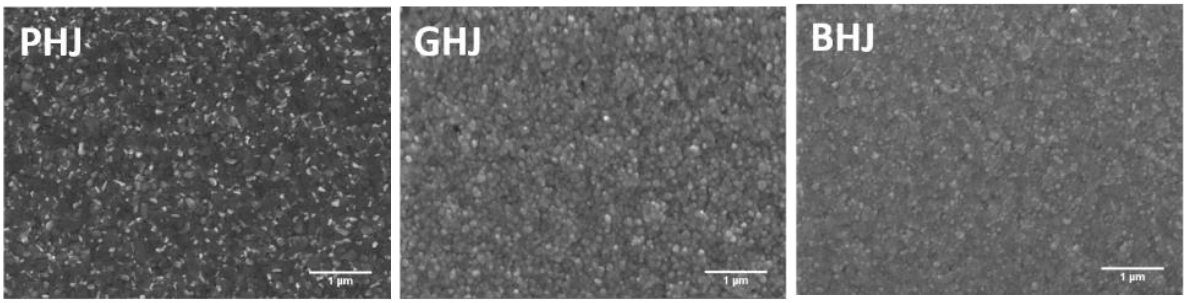

Figure 6.2. SEM images of (a) PHJ, (b) GHJ and (c) BHJ mixed Pb-Sn perovskite thin film morphology.

An alternative second method is the perovskite precursor treated with toluene solvent containing DF-C_{60} during the spin-coating, as shown in the **Figure 6.1b**. This fabrication process would result in a unique fullerene-perovskite graded heterojunction (GHJ) structure, which is reported by Han's group.[128] To be clarified, we use the term GHJ to describe the perovskite fabrication method instead of the real fullerene distribution inside the perovskite materials. The real distribution of DF-C_{60} required more analysis to confirmed. The SEM image of GHJ

perovskite thin film (**Figure 6.2**) showed that the overall grain sizes and thin film morphology is similar to the $MAPb_{0.5}Sn_{0.5}I_3$ pristine perovskite. Interestingly, the GHJ device performance is higher than the standard device, as depicted in **Figure 6.3a**. The average PCE of PVSCs improve from 11.02 ± 0.45% to 12.88 ± 0.42% by utilizing the new process. The best device performance showed PCE of 13.46% with an V_{oc} of 0.73 V, a J_{sc} of 26.33 mA/cm^2 and an FF of 0.70 when measured under forwarding voltage scan. Small hysteresis has been observed by J-V measurement with various scan rate. **Figure 6.3b** shows the corresponding EQE spectrum for the GHJ PVSCs. The integrated photocurrent densities are 26.17 mA/cm^2, in good agreement with the J_{sc} derived from the *J-V* measurement. Considering the unchanged light absorption of the PHJ and GHJ thin films, the enhancement of the photocurrent is related to an improved charge collection or reduced recombination/transport losses.

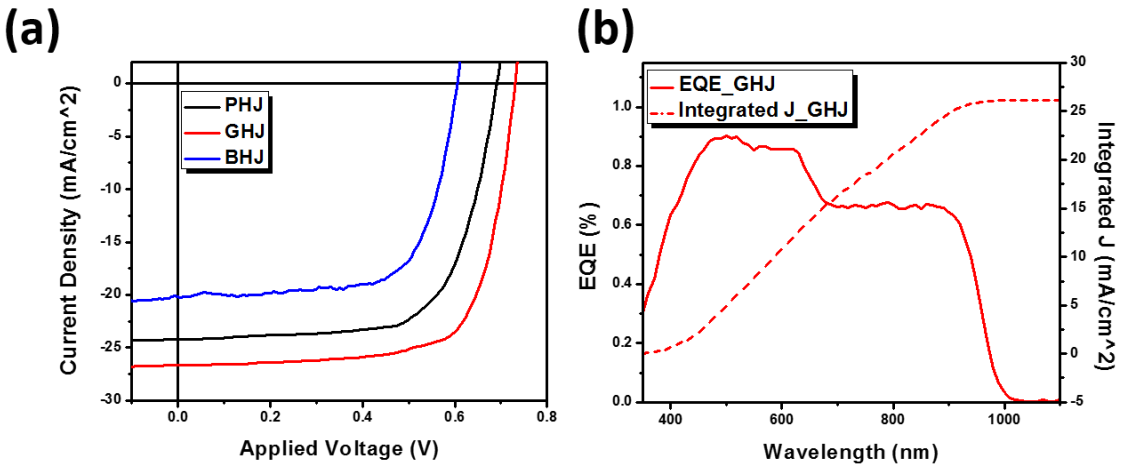

Figure 6.3. (a) the *J-V* curve of the perovskite photovoltaics with PHJ, GHJ and BHJ device configurations. (b) the EQE and accumulation current density of GHJ perovskite solar cells.

Table 6.1. Performance of the studied solar cells under AM 1.5G Illumination (100 mW cm^{-2}).

	V_{oc} (V)	J_{sc} (mA/cm^2)	*FF*	PCE (%)
PHJ	0.68±0.01 (0.69)	23.57±0.78 (24.23)	0.69±0.02 (0.68)	11.02±0.45 (11.39)
GHJ	0.72±0.02 (0.73)	25.73±1.30 (26.33)	0.69±0.01 (0.70)	12.88±0.42 (13.46)
BHJ	0.57±0.03 (0.60)	19.26±2.21 (20.20)	0.66±0.02 (0.69)	7.37±1.08 (8.43)

6.3.2 *The origin of V_{oc} Improvement*

Moreover, the V_{oc} also increased from 0.68 V in PHJ PV to 0.72 V in GHJ PV. To identify the origin of V_{oc} improvement, we used the EQE and UV-vis absorption to understand the defect states change near the band-edge of perovskite films with different device structures.[122,135–137] The band-edge slope of GHJ perovskite thin film is larger than the slope of PHJ perovskite thin-film, which indicates that a lower density of trap states occurred when the GHJ configuration was formed. Urbach energy (E_u), which is the energetic disorder at the band edge, can be derived from the equation $\eta(h\nu) = \eta_0 e^{\wedge}((h\nu - E_0)/E_{\text{Urbach}})$, where $\eta(h\nu)$ is the EQE and E_{Urbach} is the Urbach energy. From **Figure 5.3a**, the control 50% Sn ratio perovskite sample showed the Urbach energy around 21.7 meV. On the other hand, the 50% Sn ratio perovskite with graded structure showed the Urbach energy around 19.2 meV. Considering the average V_{oc} improves from 0.68 V to 0.72 V, which increases nearly 40 meV, the 2.5 meV change in the Urbach energy seems not the dominant contributor to the V_{oc} improvement. This result implies the recombination mechanism change in GHJ PVSCs may be the origin of the V_{oc} improvement.

To further elucidate the improvement of charge recombination process in Pb/Sn-binary perovskites with different structures, light-intensity-dependent PV characterization measurement were conducted. **Figure 5.3b** and d shows the light-intensity-dependent V_{oc} and J_{sc}, respectively. The V_{oc} is related to the splitting of the quasi-Fermi levels of electrons and holes with the quasi-Fermi level positions set by the free-carrier concentration, which is determined by the balance between the photogeneration and recombination rates.[138] A trap-free relationship should have a slope of $\delta V_{oc} = kT/q\ln(I)$, where q is the elementary charge, k is the Boltzmann constant, and T is the temperature.[139,140] For bimolecular recombination, the ideality factor n close to unity. On the other hand, if trap-assisted Shockley-Read-Hall (SRH) recombination dominated, the ideality factor n approached 2. In the case of PHJ, the ideality n~ 1.84 at low incident light intensities (< 10 mW/cm^2) implied SRH type recombination in this region. However, at the higher irradiance regime from 10 to 100 mW/cm^2, which is AM1.5, the ideality n~1.28 showed more bimolecular type of carrier recombination as demonstrated in the previously reported papers.[141,142] In the case of the GHJ devices, the ideality n~ 1.05 among the whole light intensity spectrum from 2 to 100 mW/cm^2. This not only implied that the bimolecular recombination dominated inside the GHJ devices, but also indicates that the tDOSs in the GHJ perovskite thin films are far lesser than the thin films of PHJ devices considering the unaffected charge recombination mechanism even at the low incident light intensity region. Furthermore, the J_{sc} at the different light intensities are shown in **Figure 6.3c**, which demonstrate the power law dependence, J_{sc} & I. The GHJ PVSCs demonstrated a slope of 0.92 compared to a slope of 0.85 for PHJ PVSCs, indicating the reduced extent of non-radiative trap assisted recombination with GHJ.[143] These results suggested that the incorporated DF-C_{60} passivates the defect state in perovskite thin-film and effectively enhances the charge collection efficiency at perovskite/ETM interface.

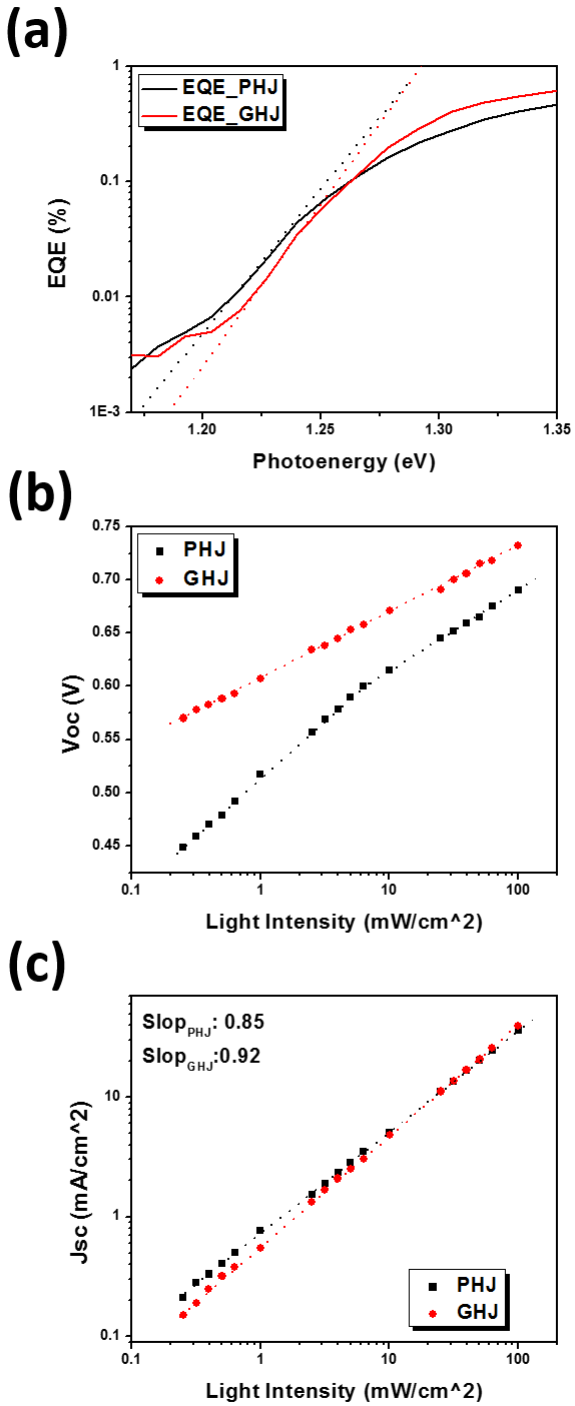

Figure 6.4. (a) EQE spectra of the PVSCs with the PHJ and GHJ device structure. The corresponding Urbach energy is estimated by fitting the EQE slope at the low energy region. Light dependent (b) open-circuit voltage and (c) short-circuit current density.

Electrochemical impedance spectroscopy (EIS) has been widely used to measure the charge transport dynamics in solar cells, such as chemical capacitance, recombination lifetime, and transport properties.[59,144] To unravel the charge dynamics in GHJ PVSCs, we measure the EIS for the device on both PHJ and GHJ PVSCs. As mentioned above, the unique GHJ fabrication process allows the fullerenes locate at the surface region of perovskite thin-film, which could possibly lower the tDOS of Sn-based perovskite.[127,128] The Nyquist plots of the PHJ and GHJ devices at different applied voltage are shown in **Figure 6.5a** and **b**. The frequency used for all EIS measurements is ranged from 1 Hz to 1 MHz. All devices were applied with a bias ranging from 0V to 0.7 V. To understand the recombination process, we fitted the data to the commonly used equivalent circuit model, where R_{surf}-C_{surf} represented the model of surface recombination, R_{bulk}-C_{bulk} represented the model for the bulk recombination, and R_{series}, $R_{internal}$ and C_{geo} represent the series resistance, internal resistance, and geometric capacitance, respectively.[113] The recombination process in devices was examined by its surface charge recombination resistance (R_{surf}) and the bulk charge recombination resistance (R_{bulk}).[113,145–148] We observed that the R_{surf} of GHJ PVSCs are almost one order higher than the values of PHJ PVSCs. These results further confirm that the unique device structure allows the fullerene derivative could efficiently passivate the defects state near perovskite surface.

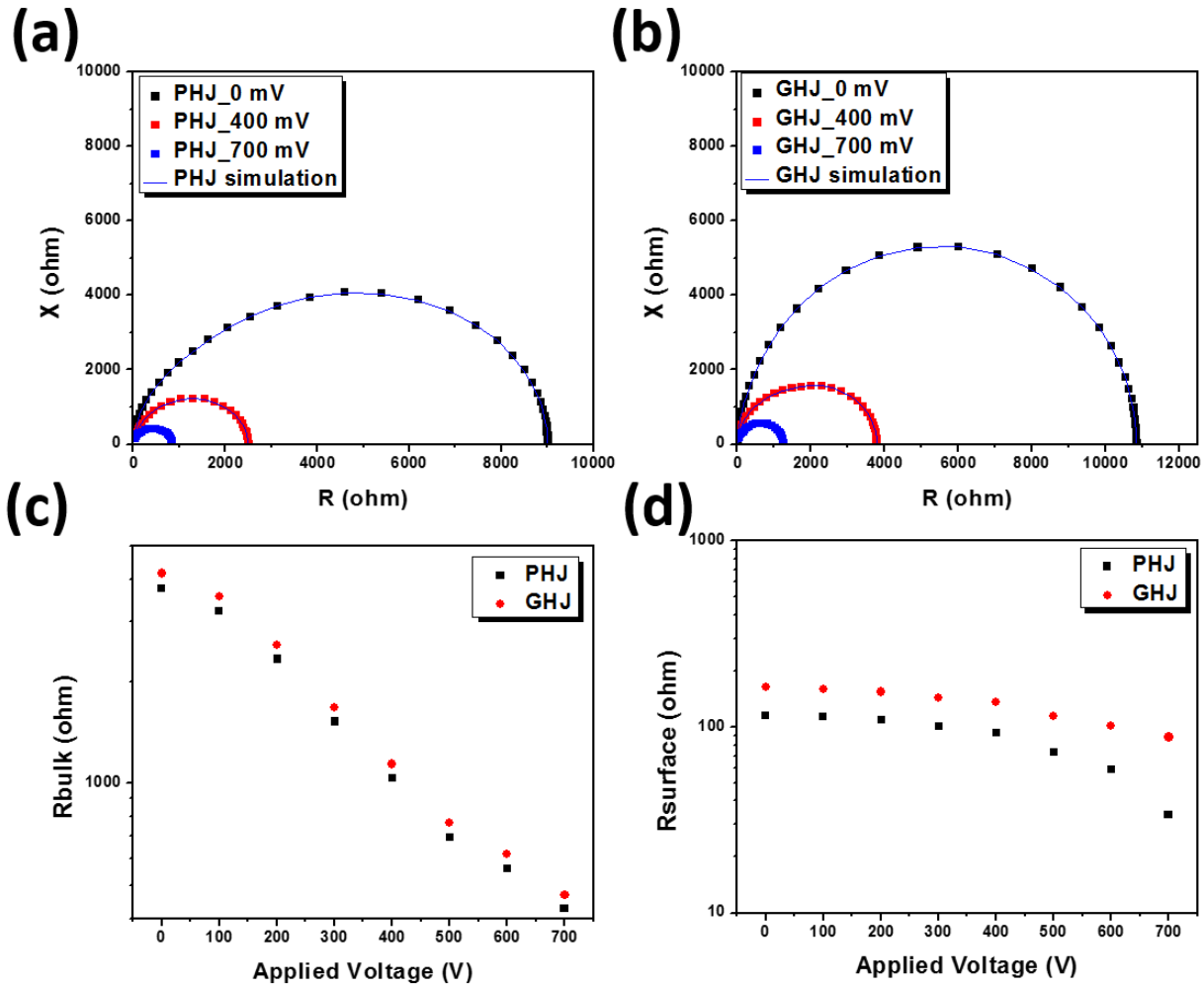

Figure 6.5. The impedance spectroscopy of the PVSCs with (a) PHJ and (b) GHJ device structures. The extracted (c) R_{buk} and (d) $R_{surface}$ value at different applied bias.

Owing to the hydrophobic nature of DF-C_{60}, the GHJ device is expected to have improved ambient stability than the PHJ PVSCs. As shown in **Figure 6.6**, the contact angle for the perovskite thin film with PHJ and GHJ structure is 52.5° and 122.5°. This discrepancy revealed that the attached perfuoroalkyl group effectively decreases the surface energy of perovskite thin film and enhanced its hydrophobicity. Besides, the preferential gradient distribution of DF-C_{60} nearby the surface of the thin film can help prevent the permeation of oxygen and moisture into the Sn-based perovskite thin film and, therefore, slow down the perovskite deterioration.

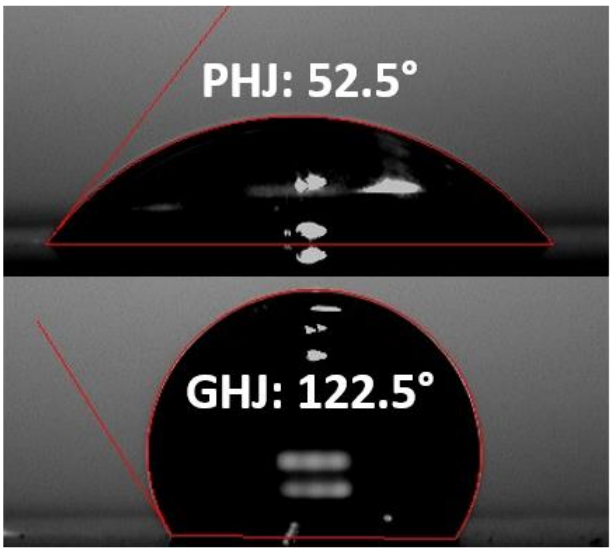

Figure 6.6. The contact angle measurement for both conditions.

Hence, we monitored the change of XRD, **Figure 6.7a** and **b**, for both PHJ and GHJ Sn-based perovskite thin film under ambient environment. Compared to the perovskite with PHJ structure, GHJ Sn-based perovskite thin films demonstrated a relatively stable XRD peak intensity. This indicated the unique GHJ fabrication process could slow the perovskite crystal decomposition. However, the Sn-based GHJ perovskite thin film drop continuously with time. This phenomenon was also found out in the PVSCs performance stability test. After devices stored in ambient with a relative humidity of 60 ± 5% for two weeks, both PHJ and GHJ PVSCs PCE drop over 50% than its original values. These results implied that a thin DF-C_{60} layer might slow down the moisture penetration, but cannot efficiently decelerate oxygen invasion, which is one of the most sensitive elements for Sn-based perovskite. In other words, in addition to moisture issue, solving the oxygen penetration problem is also important to build a stable Sn-based PVSCs. Further study to lower the moisture and oxygen permeation is critical to enhancing the stability of Sn-based PVSCs.

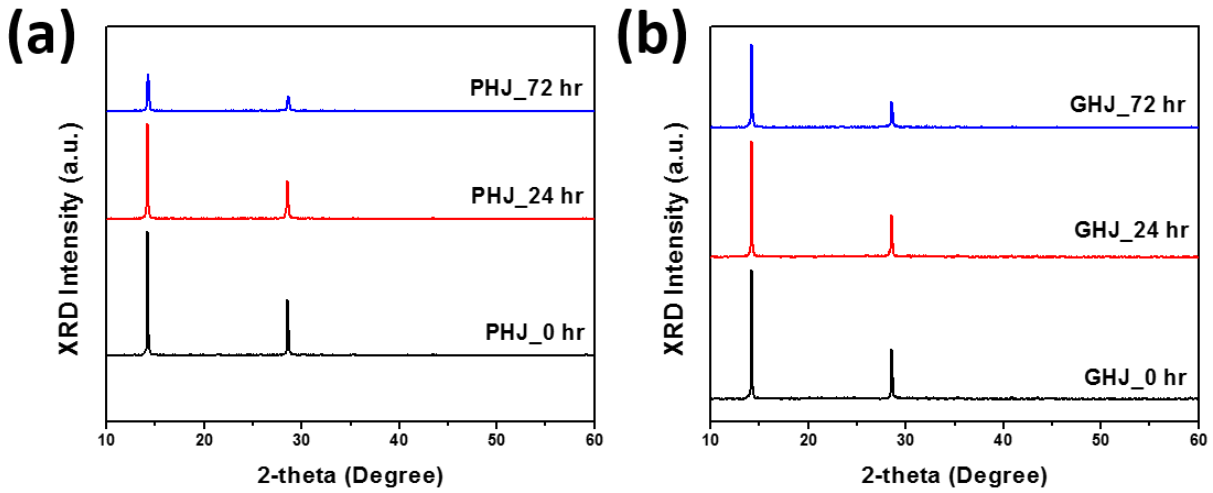

Figure 6.7. The XRD intensity change over time for the perovskite thin film with (a) PHJ and (b) GHJ structures.

6.4 SUMMARY

In summary, we have demonstrated an efficient Sn-based PVSCs with a new perovskite fabrication method. The distribution of fluoroalkyl-substituted fullerene, DF-C_{60}, inside perovskite thin film improved the charge extraction efficiency at the Sn-based perovskite/ETM interface. Meanwhile, the low surface recombination rate in GHJ Sn-based PVSCs increases V_{oc} from 0.68 V to 0.72 V. As a result, a high-performance Sn-based $MAPb_{0.5}Sn_{0.5}I_3$ PVSC with a PCE as high as 13.46% was demonstrated with small hysteresis. Finally, benefiting from the hydrophobicity of DF-C_{60}, the GHJ Sn-based PVSCs showed improved stability compared to PHJ PVSCs. Through the stability improvement is meager, it implied that the oxygen may be a more critical issue than the moisture in Sn-based PVSCs stability. Further studies related to decelerate the oxygen permeation would be needed to improve the Sn-based PVSCs stability.

Chapter 7. CONCLUSION AND FUTURE WORKS

7.1 CONCLUSION

Perovskite solar cells (PVSCs) are regarded as one of the strongest candidates for the next generation photovoltaics because of its decent solar energy conversion efficiency and the low cost of the solution fabrication process. The record efficiency of PVSCs has reached 22.1%.[3] This dissertation is focused on improving the device performance with integrated morphology, interfacial, and device engineering. The overall research can be summarized into three primary parts.

First, we successfully realized high-quality perovskite thin-film by manipulating its precursor composition and adding an extra additive. In the former method, Cl^- anions were incorporated into $MAPb(I_{1-r}Br_r)_3$, resulting in a crystallinity and homogeneity of perovskite thin-film improvement. In addition, the transient photoluminescence showed diffusion length was increased from ~160 nm to ~700-800 nm, which could contribute to the high charge collection efficiency. The later method showed a novel approach to control the perovskite crystallization morphology by introducing additive, DIO. From the SEM images and XRD spectra, the additive facilitated homogeneous nucleation through the temporary chelation. The possible hypothesis the additive mechanism was also proposed. Both morphology engineering approaches resulted in an improvement in the energy conversion efficiency. These results highlight the importance of the perovskite thin-film quality to PVSCs performance.

Second, the role of the fullerene-based interlayer in PVSCs has been revealed. By systematically study the three fullerene derivatives, ICBA, PCBM and C_{60}, we have found the clear trend between the fullerene electron extraction capability and device performance. Besides, we also demonstrate the unique interaction between the fullerenes and perovskite layer. A

spontaneous charge redistribution at the interface was discovered by carefully investigated the perovskite/fullerene field-effect transistors (FET). These interesting findings help us to have a deeper understating why fullerenes become an efficient electron transporting layer, which has high charge transfer efficiency, low recombination rate, and the capacity of defect passivation. This comprehensive study of the roles of fullerenes highlights the complexity of perovskite interface, which is an important factor to improve the device performance.

Third, a graded fullerene device structure was utilized in Pb-Sn mixed PVSCs to fully exploit the merits of fullerenes layer. The graded distribution of fluoroalkyl-substituted fullerene, DF-C_{60}, inside perovskite thin film improved V_{oc} of the PVSCs from 0.68 V to 0.72 V. From the Urbach energy estimation and impedance spectroscopy measurement, the results indicate the recombination rate in the Pb-Sn mixed perovskite processed with GHJ method is reduced. As a result, the device performance reached 13.46% with a small hysteresis. In addition to the performance improvement, benefiting from the hydrophobicity of DF-C_{60}, the GHJ Pb-Sn mixed perovskite showed improved structural stability compared to the film with PHJ device structure. Through the device performance stability didn't show the same trend with perovskite structure stability, this approach still demonstrates a huge potential to alleviate the effect of the trap states from the perovskite layer. Further studies are required to extend the PVSCs overall lifetime.

7.2 FUTURE WORKS

Solution-processed perovskite materials have just make a remarkable achievement in recent years. They have been utilized in wide application from solar cells to light emitting diodes. In this dissertation, we have an overview the decent optoelectronic properties of perovskite and integrated approaches, including morphology, interface, and device engineering, to optimize the PVSCs. This is an exciting field, but extra efforts still needed to further push this technology forward.

Efficiency is a key merit for PVSCs over the other solar technology. To maintain the competitive advantage, further reduce the non-radiative recombination and improve the charge transport is required to achieve the high V_{oc}, J_{sc}, and fill factor. The projects in this dissertation have described several promising approaches to optimizing these parameters. Further investigations are needed to go beyond the efficiency of 22%. For example, how to form a high-quality perovskite film with other methods, like new compositions or new additives? How to transform our knowledge about interface interaction between perovskite and fullerene to the non-fullerene electron transporting materials or even hole transporting materials? How to efficiently passivate the trap states at perovskite surface and boundary? These are the questions needed to be answered.

Besides the PVSCs advantage in efficiency, researchers should pay additional attention to perovskite disadvantage, which is the stability. For all the perovskite testing, it's important to tracking the maximum power point to see the stability of the power output. To test the long-term stability, it's more representative to make the device operated at the maximum power output point under 1 sum condition for whole the storage time rather than store it under dark condition. In addition, appropriate encapsulation/UV absorbers are required to prolong the lifetime of PVSCs. An exciting result showed a stable efficiency at 85°C for 500 hours under full solar illumination and maximum power output point.[149] There are many challenges remaining to understand the mechanism of the perovskite degradation and role of ionic movement for the long-term stability. It can be expected that PVSCs will become more prosperous in both academia and industry field.

BIBLIOGRAPHY

[1] O. Morton, *Nature* **2006**, *443*, 19.

[2] N. J. Jeon, J. H. Noh, Y. C. Kim, W. S. Yang, S. Ryu, S. Il Seok, *Nat. Mater.* **2014**, *13*, 897.

[3] M. A. Green, Y. Hishikawa, W. Warta, E. D. Dunlop, D. H. Levi, J. Hohl-Ebinger, A. W. H. Ho-Baillie, *Prog. Photovoltaics Res. Appl.* **2017**, *25*, 668.

[4] A. Kojima, K. Teshima, Y. Shirai, T. Miyasaka, *J. Am. Chem. Soc.* **2009**, *131*, 6050.

[5] J.-H. Im, C.-R. Lee, J.-W. Lee, S.-W. Park, N.-G. Park, *Nanoscale* **2011**, *3*, 4088.

[6] H.-S. Kim, C.-R. Lee, J.-H. Im, K.-B. Lee, T. Moehl, A. Marchioro, S.-J. Moon, R. Humphry-Baker, J.-H. Yum, J. E. Moser, M. Grätzel, N.-G. Park, *Sci. Rep.* **2012**, *2*, 591.

[7] M. M. Lee, J. Teuscher, T. Miyasaka, T. N. Murakami, H. J. Snaith, *Science* **2011**, *338*, 648.

[8] S. D. Stranks, G. E. Eperon, G. Grancini, C. Menelaou, M. J. P. Alcocer, T. Leijtens, L. M. Herz, A. Petrozza, H. J. Snaith, *Science* **2013**, *342*.

[9] G. Xing, N. Mathews, S. Sun, S. S. Lim, Y. M. Lam, M. Grätzel, S. Mhaisalkar, T. C. Sum, *Science* **2013**, *342*.

[10] L. Schmidt, in *38th Rochester Mineral. Symp.*, **2011**, pp. 31–32.

[11] I. B. Koutselas, L. Ducasse, G. C. Papavassiliou, *J. Phys. Condens. Matter* **1996**, *8*, 1217.

[12] T. Umebayashi, K. Asai, T. Kondo, A. Nakao, *Phys. Rev. B* **2003**, *67*, 155405.

[13] Y. H. Chang, C. H. Park, K. Matsuishi, *J. Korean Phys. Soc.* **2004**, *44*, 889.

[14] E. Mosconi, A. Amat, M. K. Nazeeruddin, M. Grätzel, F. De Angelis, *J. Phys. Chem. C* **2013**, *117*, 13902.

[15] T. Baikie, Y. Fang, J. M. Kadro, M. Schreyer, F. Wei, S. G. Mhaisalkar, M. Graetzel, T. J. White, *J. Mater. Chem. A* **2013**, *1*, 5628.

[16] A. Cuevas, D. Macdonald, *Sol. Energy* **2004**, *76*, 255.

[17] D. A. Valverde-Chávez, C. Ponseca, C. Stoumpos, A. Yartsev, M. G. Kanatzidis, V. Sundström, D. G. Cooke, *Energy Environ. Sci.* **2015**, *8*, 3700.

[18] D. W. DeQuilettes, S. M. Vorpahl, S. D. Stranks, H. Nagaoka, G. E. Eperon, M. E. Ziffer, H. J. Snaith, D. S. Ginger, *Science* **2015**, aaa5333.

[19] H.-H. Fang, R. Raissa, M. Abdu-Aguye, S. Adjokatse, G. R. Blake, J. Even, M. A. Loi, *Adv. Funct. Mater.* **2015**, *25*, 2378.

[20] C. Motta, F. El-Mellouhi, S. Kais, N. Tabet, F. Alharbi, S. Sanvito, *Nat. Commun.* **2015**, *6*, 7026.

[21] F. Brivio, K. T. Butler, A. Walsh, M. van Schilfgaarde, *Phys. Rev. B* **2014**, *89*, 155204.

[22] T. Wang, B. Daiber, J. M. Frost, S. A. Mann, E. C. Garnett, A. Walsh, B. Ehrler, *Energy Environ. Sci.* **2017**, *10*, 509.

[23] M. A. Green, A. Ho-Baillie, H. J. Snaith, *Nat. Photonics* **2014**, *8*, 506.

[24] S. Colella, E. Mosconi, P. Fedeli, A. Listorti, F. Gazza, F. Orlandi, P. Ferro, T. Besagni, A. Rizzo, G. Calestani, G. Gigli, F. De Angelis, R. Mosca, *Chem. Mater.* **2013**, *25*, 4613.

[25] B. Cai, Y. Xing, Z. Yang, W.-H. Zhang, J. Qiu, *Energy Environ. Sci.* **2013**, *6*, 1480.

[26] E. Edri, S. Kirmayer, M. Kulbak, G. Hodes, D. Cahen, *J. Phys. Chem. Lett.* **2014**, *5*, 429.

[27] E. Edri, S. Kirmayer, D. Cahen, G. Hodes, *J. Phys. Chem. Lett.* **2013**, *4*, 897.

[28] J. H. Noh, S. H. Im, J. H. Heo, T. N. Mandal, S. Il Seok, *Nano Lett.* **2013**, *13*, 1764.

[29] G. E. Eperon, S. D. Stranks, C. Menelaou, M. B. Johnston, L. M. Herz, H. J. Snaith, *Energy Environ. Sci.* **2014**, *7*, 982.

[30] K.-W. Tsai, C.-C. Chueh, S. T. Williams, T.-C. Wen, A. K. Y. Jen, *J. Mater. Chem. A* **2015**, *3*, 9128.

[31] N. Onoda-Yamamuro, T. Matsuo, H. Suga, *J. Phys. Chem. Solids* **1992**, *53*, 935.

[32] N. Onoda-Yamamuro, T. Matsuo, H. Suga, *J. Phys. Chem. Solids* **1990**, *51*, 1383.

[33] E. J. Juarez-Perez, R. S. Sanchez, L. Badia, G. Garcia-Belmonte, Y. S. Kang, I. Mora-Sero, J. Bisquert, *J. Phys. Chem. Lett.* **2014**, *5*, 2390.

[34] M. Hirasawa, T. Ishihara, T. Goto, K. Uchida, N. Miura, *Phys. B Condens. Matter* **1994**, *201*, 427.

[35] K. Galkowski, A. Mitioglu, A. Miyata, P. Plochocka, O. Portugall, G. E. Eperon, J. T.-W. Wang, T. Stergiopoulos, S. D. Stranks, H. J. Snaith, R. J. Nicholas, *Energy Environ. Sci.* **2016**, *9*, 962.

[36] M. I. Saidaminov, A. L. Abdelhady, B. Murali, E. Alarousu, V. M. Burlakov, W. Peng, I. Dursun, L. Wang, Y. He, G. Maculan, A. Goriely, T. Wu, O. F. Mohammed, O. M. Bakr, *Nat. Commun.* **2015**, *6*, 7586.

[37] Q. Dong, Y. Fang, Y. Shao, P. Mulligan, J. Qiu, L. Cao, J. Huang, *Science* **2015**, *347*, 967.

[38] R. Sheng, A. Ho-Baillie, S. Huang, S. Chen, X. Wen, X. Hao, M. A. Green, *J. Phys. Chem. C* **2015**, *119*, 3545.

[39] C. Wehrenfennig, G. E. Eperon, M. B. Johnston, H. J. Snaith, L. M. Herz, *Adv. Mater.* **2014**, *26*, 1584.

[40] T. J. Savenije, C. S. Ponseca, L. Kunneman, M. Abdellah, K. Zheng, Y. Tian, Q. Zhu, S. E. Canton, I. G. Scheblykin, T. Pullerits, A. Yartsev, V. Sundström, *J. Phys. Chem. Lett.* **2014**, *5*, 2189.

[41] Z. Guo, J. S. Manser, Y. Wan, P. V Kamat, L. Huang, *Nat. Commun.* **2015**, *6*, 7471.

[42] M. Zhang, H. Yu, M. Lyu, Q. Wang, J.-H. Yun, L. Wang, *Chem. Commun.* **2014**, *50*, 11727.

[43] D. Shi, V. Adinolfi, R. Comin, M. Yuan, E. Alarousu, A. Buin, Y. Chen, S. Hoogland, A. Rothenberger, K. Katsiev, Y. Losovyj, X. Zhang, P. A. Dowben, O. F. Mohammed, E. H. Sargent, O. M. Bakr, *Science* **2015**, *347*, 519.

[44] E. Edri, S. Kirmayer, S. Mukhopadhyay, K. Gartsman, G. Hodes, D. Cahen, *Nat. Commun.* **2014**, *5*, 3461.

[45] H.-S. Duan, H. Zhou, Q. Chen, P. Sun, S. Luo, T.-B. Song, B. Bob, Y. Yang, *Phys. Chem. Chem. Phys.* **2015**, *17*, 112.

[46] A. Miyata, A. Mitioglu, P. Plochocka, O. Portugall, J. T.-W. Wang, S. D. Stranks, H. J. Snaith, R. J. Nicholas, *Nat. Phys.* **2015**, *11*, 582.

[47] N. Kedem, T. M. Brenner, M. Kulbak, N. Schaefer, S. Levcenko, I. Levine, D. Abou-Ras, G. Hodes, D. Cahen, *J. Phys. Chem. Lett.* **2015**, *6*, 2469.

[48] K. Tanaka, T. Takahashi, T. Ban, T. Kondo, K. Uchida, N. Miura, *Solid State Commun.* **2003**, *127*, 619.

[49] Sze, *Physics of Semiconductor Devices*, Wiley-Interscience, **1995**.

[50] R. J. Nelson, R. G. Sobers, *J. Appl. Phys.* **1978**, *49*, 6103.

[51] V. D 'innocenzo, G. Grancini, M. J. P. Alcocer, A. Ram, S. Kandada, S. D. Stranks, M. M. Lee, G. Lanzani, H. J. Snaith, A. Petrozza, *Nat. Commun.* **2014**, *5*, 3586.

[52] Q. Lin, A. Armin, R. Chandra, R. Nagiri, P. L. Burn, P. Meredith, *Nat. Photonics* **2015**, *9*, 106.

[53] J. Even, L. Pedesseau, C. Katan, *J. Phys. Chem. C* **2014**, *118*, 11566.

[54] F. Deschler, M. Price, S. Pathak, L. E. Klintberg, D.-D. Jarausch, R. Higler, S. Hüttner, T. Leijtens, S. D. Stranks, H. J. Snaith, M. Atatüre, R. T. Phillips, R. H. Friend, *J. Phys. Chem. Lett.* **2014**, *5*, 1421.

[55] J. H. Heo, S. H. Im, J. H. Noh, T. N. Mandal, C.-S. Lim, J. A. Chang, Y. H. Lee, H.-J. Kim, A. Sarkar, K. Nazeeruddin, M. Grätzel, S. Il Seok, *Nat. Photonics* **2013**, *7*, 486.

[56] E. Edri, S. Kirmayer, A. Henning, S. Mukhopadhyay, K. Gartsman, Y. Rosenwaks, G. Hodes, D. Cahen, *Nano Lett.* **2014**, *14*, 1000.

[57] T. C. Sum, N. Mathews, *Energy Environ. Sci.* **2014**, *7*, 2518.

[58] G. Xing, N. Mathews, S. S. Lim, N. Yantara, X. Liu, D. Sabba, M. Grätzel, S. Mhaisalkar, T. C. Sum, *Nat. Mater.* **2014**, *13*, 476.

[59] V. Gonzalez-Pedro, E. J. Juarez-Perez, W.-S. Arsyad, E. M. Barea, F. Fabregat-Santiago, I. Mora-Sero, J. Bisquert, *Nano Lett.* **2014**, *14*, 888.

[60] J. T.-W. Wang, J. M. Ball, E. M. Barea, A. Abate, J. A. Alexander-Webber, J. Huang, M. Saliba, I. Mora-Sero, J. Bisquert, H. J. Snaith, R. J. Nicholas, *Nano Lett.* **2014**, *14*, 724.

[61] G. S. Han, S. Lee, J. H. Noh, H. S. Chung, J. H. Park, B. S. Swain, J.-H. Im, N.-G. Park, H. S. Jung, *Nanoscale* **2014**, *6*, 6127.

[62] D.-Y. Son, J.-H. Im, H.-S. Kim, N.-G. Park, *J. Phys. Chem. C* **2014**, *118*, 16567.

[63] A. Abrusci, S. D. Stranks, P. Docampo, H.-L. Yip, A. K.-Y. Jen, H. J. Snaith, *Nano Lett.* **2013**, *13*, 3124.

[64] J.-Y. Jeng, Y.-F. Chiang, M.-H. Lee, S.-R. Peng, T.-F. Guo, P. Chen, T.-C. Wen, *Adv. Mater.* **2013**, *25*, 3727.

[65] L. Etgar, P. Gao, Z. Xue, Q. Peng, A. K. Chandiran, B. Liu, M. K. Nazeeruddin, M. Grätzel, *J. Am. Chem. Soc.* **2012**, *134*, 17396.

[66] S. Aharon, S. Gamliel, B. El Cohen, L. Etgar, *Phys. Chem. Chem. Phys.* **2014**, *16*, 10512.

[67] X. Li, M. I. Dar, C. Yi, J. Luo, M. Tschumi, S. M. Zakeeruddin, M. K. Nazeeruddin, H. Han, M. Grätzel, *Nat. Chem.* **2015**, *7*, 703.

[68] J. H. Heo, D. H. Song, S. H. Im, *Adv. Mater.* **2014**, *26*, 8179.

[69] Y. Chen, Y. Zhao, Z. Liang, *Chem. Mater.* **2015**, *27*, 1448.

[70] P.-W. Liang, C.-Y. Liao, C.-C. Chueh, F. Zuo, S. T. Williams, X.-K. Xin, J. Lin, A. K.-Y. Jen, *Adv. Mater.* **2014**, *26*, 3748.

[71] Y. Zhao, K. Zhu, *J. Am. Chem. Soc.* **2014**, *136*, 12241.

[72] M. Xiao, F. Huang, W. Huang, Y. Dkhissi, Y. Zhu, J. Etheridge, A. Gray-Weale, U. Bach, Y.-B. Cheng, L. Spiccia, *Angew. Chemie* **2014**, *126*, 10056.

[73] Kangning Liang, A. David B. Mitzi, M. T. Prikas, *Chem. Mater.* **1998**, *10*, 403.

[74] D. B. Mitzi, *Chem. Mater.* **2001**, *13*, 3283.

[75] Q. Chen, H. Zhou, Z. Hong, S. Luo, H.-S. Duan, H.-H. Wang, Y. Liu, G. Li, Y. Yang, *J. Am. Chem. Soc.* **2014**, *136*, 622.

[76] M. Liu, M. B. Johnston, H. J. Snaith, *Nature* **2013**, *501*, 2518.

[77] NREL, "efficiency-chart.png (4348×2415)," can be found under https://www.nrel.gov/pv/assets/images/efficiency-chart.png.

[78] W. Shockley, H. J. Queisser, *J. Appl. Phys.* **1961**, *32*, 510.

[79] W. S. Yang, J. H. Noh, N. J. Jeon, Y. C. Kim, S. Ryu, J. Seo, S. I. Seok, *Science* **2015**, *348*, 1234.

[80] W. Qiu, T. Merckx, M. Jaysankar, C. Masse de la Huerta, L. Rakocevic, W. Zhang, U. W. Paetzold, R. Gehlhaar, L. Froyen, J. Poortmans, D. Cheyns, H. J. Snaith, P. Heremans, *Energy Environ. Sci.* **2016**, *9*, 484.

[81] A. Sharenko, M. F. Toney, *J. Am. Chem. Soc.* **2016**, *138*, 463.

[82] J. C. Yu, D. Bin Kim, G. Baek, B. R. Lee, E. D. Jung, S. Lee, J. H. Chu, D.-K. Lee, K. J. Choi, S. Cho, M. H. Song, *Adv. Mater.* **2015**, *27*, 3492.

[83] H. Yu, F. Wang, F. Xie, W. Li, J. Chen, N. Zhao, *Adv. Funct. Mater.* **2014**, *24*, 7102.

[84] Y. Zhao, K. Zhu, *J. Phys. Chem. C* **2014**, *118*, 9412.

[85] Y. Zhao, A. M. Nardes, K. Zhu, *Faraday Discuss.* **2014**, *176*, 301.

[86] S. A. Kulkarni, T. Baikie, P. P. Boix, N. Yantara, N. Mathews, S. Mhaisalkar, *J. Mater. Chem. A* **2014**, *2*, 9221.

[87] P. Docampo, J. M. Ball, M. Darwich, G. E. Eperon, H. J. Snaith, *Nat. Commun.* **2013**, *4*, 2761.

[88] Z. Xiao, C. Bi, Y. Shao, Q. Dong, Q. Wang, Y. Yuan, C. Wang, Y. Gao, J. Huang, *Energy Environ. Sci.* **2014**, *7*, 2619.

[89] Q. Wang, Y. Shao, Q. Dong, Z. Xiao, Y. Yuan, J. Huang, *Energy Environ. Sci.* **2014**, *7*, 2359.

[90] S. Sun, T. Salim, N. Mathews, M. Duchamp, C. Boothroyd, G. Xing, T. C. Sum, Y. M. Lam, *Energy Environ. Sci.* **2014**, *7*, 399.

[91] O. Malinkiewicz, A. Yella, Y. H. Lee, G. M. Espallargas, M. Graetzel, M. K. Nazeeruddin, H. J. Bolink, *Nat. Photonics* **2014**, *8*, 128.

[92] Y. Yang, J. You, Z. Hong, Q. Chen, M. Cai, T. Bin Song, C. C. Chen, S. Lu, Y. Liu, H.

Zhou, *ACS Nano* **2014**, *8*, 1674.

[93] C.-C. Chueh, S.-C. Chien, H.-L. Yip, J. F. Salinas, C.-Z. Li, K.-S. Chen, F.-C. Chen, W.-C. Chen, A. K.-Y. Jen, *Adv. Energy Mater.* **2013**, *3*, 417.

[94] K. M. O'Malley, C.-Z. Li, H.-L. Yip, A. K.-Y. Jen, *Adv. Energy Mater.* **2012**, *2*, 82.

[95] S. Ryu, J. H. Noh, N. J. Jeon, Y. Chan Kim, W. S. Yang, J. Seo, S. Il Seok, I. Mora-Sero, I. McCulloch, M. K. Nazeeruddin, M. Grätzel, S. I. Seok, *Energy Environ. Sci.* **2014**, *7*, 2614.

[96] S. Aharon, B. El Cohen, L. Etgar, *J. Phys. Chem. C* **2014**, *118*, 17160.

[97] B. Conings, L. Baeten, C. De Dobbelaere, J. D'Haen, J. Manca, H.-G. Boyen, *Adv. Mater.* **2014**, *26*, 2041.

[98] G. E. Eperon, V. M. Burlakov, P. Docampo, A. Goriely, H. J. Snaith, *Adv. Funct. Mater.* **2014**, *24*, 151.

[99] P.-W. Liang, C.-C. Chueh, X.-K. Xin, F. Zuo, S. T. Williams, C.-Y. Liao, A. K.-Y. Jen, *Adv. Energy Mater.* **2015**, *5*, 1400960.

[100] J. K. Lee, W. L. Ma, C. J. Brabec, J. Yuen, J. S. Moon, J. Y. Kim, K. Lee, G. C. Bazan, A. J. Heeger, *J. Am. Chem. Soc.* **2008**, *130*, 3619.

[101] J. Peet, J. Y. Kim, N. E. Coates, W. L. Ma, D. Moses, A. J. Heeger, G. C. Bazan, S. S. S N N Pcpdtbt Ch, *Nat. Mater.* **2007**, *6*, 497.

[102] D. B. Mitzi, C. A. Feild, W. T. A. Harrison, A. M. Guloy, *Nature* **1994**, *369*, 467.

[103] C. R. Kagan, D. B. Mitzi, C. D. Dimitrakopoulos, *Science* **1999**, *286*.

[104] J. Qiu, Y. Qiu, K. Yan, M. Zhong, C. Mu, H. Yan, S. Yang, M. Grätzel, J. H. Yum, J. E. Moser, M. Grätzel, N. G. Park, *Nanoscale* **2013**, *5*, 3245.

[105] R. J. Kulawiec, R. H. Crabtree, *Coord. Chem. Rev.* **1990**, *99*, 89.

[106] D. N. Kravtsov, B. A. Kvasov, L. S. Golovchenko, E. M. Rokhlina, E. I. Fedin, *J. Organomet. Chem.* **1972**, *39*, 107.

[107] P. J. Albietz, B. P. Cleary, W. Paw, R. Eisenberg, *Inorg. Chem.* **2002**, *41*, 2095.

[108] F. Zuo, S. T. Williams, P.-W. Liang, C.-C. Chueh, C.-Y. Liao, A. K.-Y. Jen, *Adv. Mater.* **2014**, *26*, 6454.

[109] C.-C. Chueh, C.-Y. Liao, F. Zuo, S. T. Williams, P.-W. Liang, A. K.-Y. Jen, S. I. Seok, J. T. W. Wang, K. Wojciechowski, W. Zhang, X. Hou, S. I. Seok, *J. Mater. Chem. A* **2015**, *3*, 9058.

[110] H. J. Snaith, A. Abate, J. M. Ball, G. E. Eperon, T. Leijtens, N. K. Noel, S. D. Stranks, J. T.-W. Wang, K. Wojciechowski, W. Zhang, *J. Phys. Chem. Lett.* **2014**, *5*, 1511.

[111] A. Abate, M. Saliba, D. J. Hollman, S. D. Stranks, K. Wojciechowski, R. Avolio, G. Grancini, A. Petrozza, H. J. Snaith, *Nano Lett.* **2014**, *14*, 3247.

[112] N. K. Noel, A. Abate, S. D. Stranks, E. S. Parrott, V. M. Burlakov, A. Goriely, H. J. Snaith, *ACS Nano* **2014**, *8*, 9815.

[113] Y. Shao, Z. Xiao, C. Bi, Y. Yuan, J. Huang, *Nat. Commun.* **2014**, *5*, 5784.

[114] C.-Z. Li, C.-C. Chueh, H.-L. Yip, F. Ding, X. Li, A. K.-Y. Jen, *Adv. Mater.* **2013**, *25*, 2457.

[115] C.-Z. Li, C.-C. Chueh, F. Ding, H.-L. Yip, P.-W. Liang, X. Li, A. K.-Y. Jen, *Adv. Mater.* **2013**, *25*, 4425.

[116] N. K. Noel, S. D. Stranks, A. Abate, C. Wehrenfennig, S. Guarnera, A.-A. Haghighirad, A. Sadhanala, G. E. Eperon, S. K. Pathak, M. B. Johnston, A. Petrozza, L. M. Herz, H. J. Snaith, *Energy Environ. Sci.* **2014**, *7*, 3061.

[117] M. H. Kumar, S. Dharani, W. L. Leong, P. P. Boix, R. R. Prabhakar, T. Baikie, C. Shi, H. Ding, R. Ramesh, M. Asta, M. Graetzel, S. G. Mhaisalkar, N. Mathews, *Adv. Mater.* **2014**, *26*, 7122.

[118] F. Hao, C. C. Stoumpos, R. P. H. Chang, M. G. Kanatzidis, *J. Am. Chem. Soc.* **2014**, *136*, 8094.

[119] Z. Yang, A. Rajagopal, C.-C. Chueh, S. B. Jo, B. Liu, T. Zhao, A. K.-Y. Jen, *Adv. Mater.* **2016**, *28*, 8990.

[120] S. J. Lee, S. S. Shin, Y. C. Kim, D. Kim, T. K. Ahn, J. H. Noh, J. Seo, S. Il Seok, *J. Am. Chem. Soc.* **2016**, *138*, 3974.

[121] X. Xu, C.-C. Chueh, Z. Yang, A. Rajagopal, J. Xu, S. B. Jo, A. K.-Y. Jen, *Nano Energy* **2017**, *34*, 392.

[122] D. Zhao, Y. Yu, C. Wang, W. Liao, N. Shrestha, C. R. Grice, A. J. Cimaroli, L. Guan, R. J. Ellingson, K. Zhu, X. Zhao, R.-G. Xiong, Y. Yan, *Nat. Energy* **2017**, *2*, 17018.

[123] X. Wu, M. T. Trinh, D. Niesner, H. Zhu, Z. Norman, J. S. Owen, O. Yaffe, B. J. Kudisch, X.-Y. Zhu, *J. Am. Chem. Soc.* **2015**, *137*, 2089.

[124] I. Chung, J.-H. Song, J. Im, J. Androulakis, C. D. Malliakas, H. Li, A. J. Freeman, J. T. Kenney, M. G. Kanatzidis, *J. Am. Chem. Soc.* **2012**, *134*, 8579.

[125] J. Xu, A. Buin, A. H. Ip, W. Li, O. Voznyy, R. Comin, M. Yuan, S. Jeon, Z. Ning, J. J. McDowell, P. Kanjanaboos, J.-P. Sun, X. Lan, L. N. Quan, D. H. Kim, I. G. Hill, P. Maksymovych, E. H. Sargent, *Nat. Commun.* **2015**, *6*, 7081.

[126] P.-W. Liang, C.-C. Chueh, S. T. Williams, A. K.-Y. Jen, *Adv. Energy Mater.* **2015**, *5*, 1402321.

[127] X. Liu, F. Lin, C.-C. Chueh, Q. Chen, T. Zhao, P.-W. Liang, Z. Zhu, Y. Sun, A. K.-Y. Jen, *Nano Energy* **2016**, *30*, 417.

[128] Y. Wu, X. Yang, W. Chen, Y. Yue, M. Cai, F. Xie, E. Bi, A. Islam, L. Han, *Nat. Energy* **2016**, *1*, 16148.

[129] J. Chang, H. Zhu, J. Xiao, F. H. Isikgor, Z. Lin, Y. Hao, K. Zeng, Q.-H. Xu, J. Ouyang, *J. Mater. Chem. A* **2016**, *4*, 7943.

[130] T. J. Jacobsson, J.-P. Correa-Baena, E. Halvani Anaraki, B. Philippe, S. D. Stranks, M. E. F. Bouduban, W. Tress, K. Schenk, J. Teuscher, J.-E. Moser, H. Rensmo, A. Hagfeldt, *J. Am. Chem. Soc.* **2016**, *138*, 10331.

[131] C. Roldán-Carmona, P. Gratia, I. Zimmermann, G. Grancini, P. Gao, M. Graetzel, M. K. Nazeeruddin, *Energy Environ. Sci.* **2015**, *8*, 3550.

[132] C.-H. Chiang, C.-G. Wu, *Nat. Photonics* **2016**, *10*, 196.

[133] Y. Zhao, W. Zhou, W. Ma, S. Meng, H. Li, J. Wei, R. Fu, K. Liu, D. Yu, Q. Zhao, *ACS Energy Lett.* **2016**, *1*, 266.

[134] K. Wang, C. Liu, P. Du, J. Zheng, X. Gong, *Energy Environ. Sci.* **2015**, *8*, 1245.

[135] J. T.-W. Wang, Z. Wang, S. Pathak, W. Zhang, D. W. deQuilettes, F. Wisnivesky-Rocca-Rivarola, J. Huang, P. K. Nayak, J. B. Patel, H. A. Mohd Yusof, Y. Vaynzof, R. Zhu, I. Ramirez, J. Zhang, C. Ducati, C. Grovenor, M. B. Johnston, D. S. Ginger, R. J. Nicholas, H. J. Snaith, *Energy Environ. Sci.* **2016**, *9*, 2892.

[136] S. De Wolf, J. Holovsky, S.-J. Moon, P. Löper, B. Niesen, M. Ledinsky, F.-J. Haug, J.-H. Yum, C. Ballif, *J. Phys. Chem. Lett.* **2014**, *5*, 1035.

[137] A. Sadhanala, F. Deschler, T. H. Thomas, S. E. Dutton, K. C. Goedel, F. C. Hanusch, M. L. Lai, U. Steiner, T. Bein, P. Docampo, D. Cahen, R. H. Friend, *J. Phys. Chem. Lett.* **2014**, *5*, 2501.

[138] S. R. Cowan, W. L. Leong, N. Banerji, G. Dennler, A. J. Heeger, *Adv. Funct. Mater.* **2011**, *21*, 3083.

[139] M. M. Mandoc, F. B. Kooistra, J. C. Hummelen, B. de Boer, P. W. M. Blom, *Appl. Phys. Lett.* **2007**, *91*, 263505.

[140] S. R. Cowan, A. Roy, A. J. Heeger, *Phys. Rev. B* **2010**, *82*, 245207.

[141] L. Gouda, R. Gottesman, A. Ginsburg, D. A. Keller, E. Haltzi, J. Hu, S. Tirosh, A. Y. Anderson, A. Zaban, P. P. Boix, *J. Phys. Chem. Lett.* **2015**, *6*, 4640.

[142] B. Zhao, M. Abdi-Jalebi, M. Tabachnyk, H. Glass, V. S. Kamboj, W. Nie, A. J. Pearson, Y. Puttisong, K. C. Gödel, H. E. Beere, D. A. Ritchie, A. D. Mohite, S. E. Dutton, R. H. Friend, A. Sadhanala, *Adv. Mater.* **2017**, *29*, 1604744.

[143] L. J. A. Koster, V. D. Mihailetchi, H. Xie, P. W. M. Blom, *Appl. Phys. Lett.* **2005**, *87*, 203502.

[144] J. Bisquert, I. Mora-Sero, F. Fabregat-Santiago, *ChemElectroChem* **2014**, *1*, 289.

[145] A. Guerrero, G. Garcia-Belmonte, I. Mora-Sero, J. Bisquert, Y. S. Kang, T. J. Jacobsson, J.-P. Correa-Baena, A. Hagfeldt, *J. Phys. Chem. C* **2016**, *120*, 8023.

[146] M. Bag, L. A. Renna, R. Y. Adhikari, S. Karak, F. Liu, P. M. Lahti, T. P. Russell, M. T. Tuominen, D. Venkataraman, *J. Am. Chem. Soc.* **2015**, *137*, 13130.

[147] A. Dualeh, T. Moehl, N. Tétreault, J. Teuscher, P. Gao, M. K. Nazeeruddin, M. Grätzel, *ACS Nano* **2014**, *8*, 362.

[148] H.-S. Kim, I. Mora-Sero, V. Gonzalez-Pedro, F. Fabregat-Santiago, E. J. Juarez-Perez, N.-G. Park, J. Bisquert, *Nat. Commun.* **2013**, *4*, 2242.

[149] M. Saliba, T. Matsui, K. Domanski, J.-Y. Seo, A. Ummadisingu, S. M. Zakeeruddin, J.-P. Correa-Baena, W. R. Tress, A. Abate, A. Hagfeldt, M. Grätzel, *Science* **2016**, *354*, 206.

VITA

Po-Wei Liang was born in Kaohsiung, Taiwan. In 2008 he earned a Bachelor of Science in Electrical Engineering from National Sun Yat-Sen University. In 2010 he earned a Master of Science in Photonics from National Cheng Kung University. In 2017 he earned a Doctor of Philosophy at the University of Washington in Materials Science and Engineering.